UNIVERSITY OF CALIFORNIA,
IRVINE

Temperature Variability in Coastal Environments Driven by Cross-Shore Exchange Associated with Baroclinic Thermal and Ekman Dynamics

DISSERTATION

submitted in partial satisfaction of the requirements
for the degree of

DOCTOR OF PHILOSOPHY

in Civil and Environmental Engineering

by

Aryan Safaie

Dissertation Committee:
Kristen Davis, Chair
Geno Pawlak
Russ Detwiler

2021

This work is dedicated to the brilliant Nirnimesh Kumar;
Righteous
Intelligent
Compassionate
A light in a frighteningly dark world.

TABLE OF CONTENTS

LIST OF FIGURES

LIST OF TABLES

ACKNOWLEDGMENTS

Thank you Kristen Alexis Davis. As an advisor, you've fostered my growth and curiosity, and have given me opportunities I could never have dreamt of. As a mentor, you've been supportive and compassionate. I'm thankful for every interaction I've had with you, for very often, you've unknowingly made me happy and brought a smile to my face, and you've inspired and challenged me to be a better version of myself. You are the best example of a role model, an educator, and a leader. I'm extremely thankful and honored to have you as my Ph.D. advisor.

Many thanks to Geno Pawlak. I am very grateful for your help and guidance through my studies, and I thank you for pushing me towards greatness. I realize how incredibly lucky I am for all of the focused, rigorous, and rewarding science discussions we've had; video conferences with you and Kristen were among the most rewarding experiences of my graduate life. Thank you for your energy, your intelligence, your spirit, and most importantly, thank you for teaching me.

Thank you to my peer, and more importantly, my friend, Emma Reid. Thank you for your camaraderie and your support, for without you, I would probably not have made it. I'm excited to see where all of your hard work and brilliance will take you, for you deserve the best.

My deepest appreciation to Sarah Merrigan. Thank you for allowing me to pretend I'm mature and qualified enough to give advice to others, and thank you for sharing your work and your research with me. I wish you happiness and success in your graduate student journey.

Thank you to all of my fellow Coastal Dynamics Lab members: Christina Frieder, Greg Sinnett, Isabella Arzeno, Sam Kastner, Lily Nguyen, Jared Brzenski, and Jayden Wood. I look forward to seeing you all flourish in your careers, in academia or otherwise, and I thank you for your kinship and your help, especially during this pandemic.

Many people, at UCI and elsewhere, have been indispensable to my success as a researcher and graduate student. April Heath, Sergio Carnalla, Matthew Brand, Jochen Schubert, James Beam, and Russ Detwiler, you all have come to my aid, often on short notice, without condition or question. Thank you to everyone at UCSD and Scripps who has shared their knowledge and experience with me, particularly Sarah Giddings, Falk Feddersen, Nirnimiseh Kumar, and Ata Suanda. Thank you to John Warner, John Wilkin, Hernan Arango, Kate Hedstrom, Sasha Shchepetkin, and Jamie Pringle, for all of your technical wizardry with ROMS, and your patience with my incessant forum-posting.

Most importantly, I would like to thank my family for their love and support throughout this experience. To my parents, Nahid and Majid, thank you for being there for me at all times, thank you for giving me safety, thank you for nurturing me, and thank you for guiding me. You are embodiments of courage and virtue. To Kia, thank you for prioritizing

my happiness, and thank you for your kindness. To Timon, thank you for being my best friend, and for understanding me. You two are at the center of my world; thank you for being my protectors.

This work was generously supported by the National Science Foundation (OCE 1436254), as well as the UCI OCEANS Initiative and the UCI Data Science Fellowship.

Chapter 1, as well as Appendices A-D, in full, is a reprint of material as it appears in Safaie, A., Silbiger, N. J., McClanahan, T. R., Pawlak, G., Barshis, D. J., Hench, J. L., ... & Davis, K. A. (2018). "High frequency temperature variability reduces the risk of coral bleaching". Nature communications, 9(1), 1-12. The dissertation author was the primary investigator and author of this paper.

Chapter 2, in full, is currently being prepared for submission for publication of the material to Journal of Geophysical Research: Oceans by A. Safaie, G. Pawlak, and K. A. Davis. The dissertation author was the primary investigator and author of this paper.

Chapter 3, in full, is currently being prepared for submission for publication of the material by A. Safaie, G. Pawlak, and K. A. Davis. The dissertation author was the primary investigator and author of this paper.

VITA

Aryan Safaie

EDUCATION

Doctor of Philosophy in Civil and Environmental Engineering **2021**
University of California, Irvine *Irvine, CA*

Master of Science in Civil and Environmental Engineering **2013**
University of California, Irvine *Irvine, CA*

Bachelor of Science in Mechanical Engineering **2011**
California Institute of Technology *Pasadena, CA*

RESEARCH EXPERIENCE

Graduate Research Assistant **2013–2020**
University of California, Irvine *Irvine, California*

TEACHING EXPERIENCE

Teaching Assistant **2013–2020**
University of California, Irvine *Irvine, California*

REFEREED JOURNAL PUBLICATIONS

High frequency temperature variability reduces the risk of coral bleaching **2018**
Nature Communications

Internal waves influence the thermal and nutrient environment on a shallow coral reef **2019**
Limnology and Oceanography

ABSTRACT OF THE DISSERTATION

Temperature Variability in Coastal Environments Driven by Cross-Shore Exchange Associated with Baroclinic Thermal and Ekman Dynamics

By

Aryan Safaie

Doctor of Philosophy in Civil and Environmental Engineering

University of California, Irvine, 2021

Kristen Davis, Chair

Within coastal environments, multiple physical processes influence the concentration of nutrients, oxygen, salinity, and other important ecological variables. Many of these physical mechanisms, which include surface and internal waves, tides, winds, and daily heating and cooling, produce considerable nearshore environmental variability on diurnal time scales. In the case of tropical coral reefs, diurnal temperature variability has been previously demonstrated to enhance coral resistance to thermal stress, and therefore reduce the prevalence of bleaching. Here, we ascertain the importance of diurnal temperature variability over other thermal stress metrics for predicting coral bleaching, using a collection of over 100 in situ temperature time series from 5 global reef regions matched with 46 bleaching observations. Results indicate that high-frequency temperature variability is the most influential metric in explaining bleaching outcomes, offering a mitigating effect such that a 1 °C increase in daily temperature range would reduce the odds of more severe bleaching by a factor of 33. Implications for prioritizing reefs for conservation are noted.

As there are multiple physical processes driving diurnal temperature variability in the nearshore and within coral reefs, we are further concerned with the role of strong atmosphere-ocean heat fluxes over nonuniform bathymetry, generic features of tropical reef environments,

in shaping the nearshore thermal environment. In such regions, surface heat fluxes lead to greater volumetric heating and cooling in shallower waters than adjacent deeper ones, establishing a horizontal temperature gradient that subsequently drives a vertically sheared exchange flow. The importance of this thermally-driven exchange to cross-shore volume and heat transport is apparent in multiple field observations, whereby modulations from alongshore currents are considerable. Using the Regional Ocean Modeling System (ROMS), we investigate the role of steady, upwelling- and downwelling-favorable alongshore currents of varying magnitudes in altering the structure of thermal exchange. Circulation in a base-case simulation with no alongshore forcing demonstrates a robust diurnal pattern consisting of a downslope flow from convective cooling and a buoyant warm front from surface heating, with cross-shore velocities of $O(1)$ cm s^{-1}. Mild upwelling- and downwelling-favorable alongshore currents enhance the nearshore temperature gradient, thereby strengthening the thermal exchange. However, as the alongshore current is strengthened, the resulting near-bed shear-generated turbulence induces substantial vertical mixing, dampening temperature gradients and weakening thermally-driven exchange.

When the alongshore forcing is further increased such that the associated turbulent mixing homogenizes the water column, the *thermally-driven* exchange vanishes, yet there remains nontrivial baroclinic cross-shore exchange, which we investigate by invoking bottom Ekman theory. A theoretical model derived from central differences of the classical Ekman balances is used to compute the horizontal velocity profiles resulting from an alongshore bottom stress, and we find that the ability of the theoretical solution to reproduce the expected flow features largely depends on the form of the eddy viscosity. Velocities of the theoretical model are then compared with those of ROMS, which includes nonlinear advection terms in the governing equations. The resulting dynamics and consequences for baroclinic cross-shore exchange of these additional terms are discussed in the context of the alongshore momentum budget.

Introduction

Coral reef ecosystems are of immense value as a source for nutrition, revenue, coastal protection, and recreation for human populations (Costanza et al., 2014; West and Salm, 2003; Hoegh-Guldberg et al., 2007). Due to global warming, rising ocean temperatures (Van Hooidonk et al., 2016; Hughes et al., 2017; Grottoli et al., 2006) threaten corals through a process known as bleaching (Hughes et al., 2017; Glynn, 1993), or the ejection of the symbiotic algae from the coral host (Glynn, 1993; Goreau and Hayes, 1994), and bleached corals are susceptible to disease and mortality (Jokiel et al., 2004; Hughes et al., 2017; Dunn et al., 2004; Berkelmans et al., 2004). Remotely-sensed satellite observations of sea surface temperatures are conventionally used to monitor thermal stress on reefs (Hughes et al., 2017; Goreau and Hayes, 1994; Goreau et al., 2000; Liu et al., 2014), yet such data is of relatively coarse spatiotemporal resolution compared to the important physical and biological processes occurring within individual reefs, such as the history and duration of thermal stress exposure (Berkelmans, 2002; Middlebrook et al., 2008), flow conditions (McClanahan et al., 2005), heterotrophic feeding (Grottoli et al., 2006), and turbidity (Williams et al., 2010). Furthermore, reef-scale gradients in both thermal environments and coral bleaching escape detection from remotely-sensed metrics of thermal stress (DeCarlo et al., 2017; Oliver and Palumbi, 2011; Guadayol et al., 2014).

Conventional metrics of thermal stress used for issuing bleaching alerts often rely on knowledge of an aggregate summer threshold temperature (Hughes et al., 2017; Goreau and Hayes, 1994; Goreau et al., 2000; Liu et al., 2006). In recent years, however, a multitude of more nuanced metrics of thermal stress have proven adept in predicting coral performance during acute temperature anomalies. Notable among these is historical temperature variability (Barshis et al., 2013; Rogers et al., 2016; Schoepf et al., 2015; Ainsworth et al., 2016), particularly within diurnal time scales (Oliver and Palumbi, 2011; McClanahan et al., 2005;

Carilli et al., 2012; Palumbi et al., 2014; Castillo et al., 2012). As such, the focus of Chapter 1 of this dissertation is to demonstrate the role of "high-frequency" temperature variability in determining corals' physiological response to thermal stress, and thereby reef-scale vulnerability to bleaching, for a better understanding of reef-scale bleaching risk factors could help coastal management efforts to identify natural refugia, and may be important for the recovery of coral communities following a bleaching event (Riegl and Piller, 2003). After using ordinal logistic regression modeling to assess the ability of 27 temperature and environmental metrics in explaining bleaching observations from five major reef regions globally, we conclude that high-frequency temperature variability, specifically the average daily temperature range of the 30 days preceding a bleaching observation, is the most influential covariate in predicting the bleaching response, and serves to attenuate the prevalence of bleaching.

Coral reefs are often found on narrow coastal shelves with optically clear water and irregular bathymetry, where multiple physical mechanisms interact to shape the thermal environment. Forcings from surface waves (Lentz et al., 2008; Lowe et al., 2009), winds (Austin and Lentz, 2002; Lentz and Fewings, 2012), tides (Leichter and Miller, 1999), internal tides and internal waves (Leichter et al., 1996; Reid et al., 2019), and daily heating and cooling (Davis et al., 2011), not only determine nearshore temperatures, but are also responsible for driving and modulating cross-shore fluxes of heat, nutrients, and planktonic organisms to nearshore ecosystems (Roughgarden et al., 1988; Nittrouer and Wright, 1994; Falkowski et al., 1998; Pringle, 2001; Brink, 2016). For tropical coral reefs, cross-shore exchange promotes larval connectivity between reefs and adjacent ecosystems (Pineda et al., 2007; Cowen and Sponaugle, 2009), and mitigates thermal stress by transporting heat (Molina et al., 2014; Herdman et al., 2015). In such areas, strong atmospheric surface heat fluxes over nonuniform bathymetry induce greater volumetric heating and cooling in shallower water than deeper water, establishing a horizontal temperature gradient and a subsequent baroclinic pressure gradient that drives a vertically-sheared exchange circulation (Monismith et al., 1990, 2006). This "thermal siphon" is the focus of Chapter 2 of this dissertation, as investigating the role

of surface heat fluxes in driving cross-shore transport improves our overall understanding of coastal circulation.

The work of Monismith et al. (1990) is an early analysis of thermally-driven baroclinic exchange using observations from a reservoir in Western Australia, while subsequent studies, such as those by Farrow and Patterson (1993) and Lei and Patterson (2006), establish a theoretical framework for convectively-driven flows and provide solutions for the associated temperature and velocity responses. Our investigation of cross-shore thermally-driven baroclinic exchange is largely motivated by the works of Monismith et al. (2006) and Molina et al. (2014), whose observational evidence of thermal exchange facilitate a thorough assessment of the dynamical regimes constraining the thermal and cross-shore momentum balances. Ulloa et al. (2018) extends this work to demonstrate how tidally-driven alongshore flow influences the cross-shore momentum budget through Coriolis and bottom-driven vertical turbulent diffusion. As the observational data supporting the study of Ulloa et al. (2018) was site-specific, we seek to generalize their results and broaden our understanding of the modulation of thermal exchange by bottom-generated turbulence, via the paradigm that stronger alongshore flow weakens thermally-driven cross-shore exchange through enhanced turbulent mixing. In Chapter 2, we present an idealized numerical modeling investigation of the influence of steady, upwelling- and downwelling-favorable alongshore currents of varying magnitudes on baroclinic thermally-driven cross-shore exchange over a sloping bottom. Our analysis contrasts the cross-shore momentum balances, coastal circulation, and thermal gradients of a base-case, surface-heat-flux-only simulation against those resulting from the perturbation of thermal exchange by upwelling- and downwelling-favorable alongshore currents. While enhanced vertical mixing from near-bed shear-generated turbulence does indeed erase cross-shore temperature gradients and reduce the strength of thermal exchange, we find that very weak upwelling- and downwelling-favorable alongshore currents increase the nearshore temperature gradient, resulting in stronger thermally-driven exchange than anticipated. Furthermore, as the strength of the alongshore flow is increased so as to dec-

imate stratification and therefore overwhelm the thermally-driven exchange, there remains a nontrivial cross-shore exchange, which is attributed to rotational effects. Specifically, the baroclinic cross-shore exchange produced by a strong alongshore current is indicative of the role of bottom Ekman dynamics, and is necessarily investigated in Chapter 3.

The work of Ekman (1905) demonstrated how the combined influence of the earth's rotation and friction between overlying water layers causes a horizontal current to veer through the water column, producing what is commonly known as an Ekman spiral. For an ocean of infinite depth, Ekman demonstrated the angle between the direction of a steady, uniform wind stress and the current at the water surface to equal 45°, while for finite depths, these angles may be considerably smaller. Similarly, for infinite depths, Ekman revealed the horizontal pressure gradients resulting from sea-surface inclinations to produce bottom currents directed 45° from the direction of the pressure gradient force. To date, numerous observational and analytical studies have applied Ekman's analysis to shallow, coastal regions, where pressure-driven bottom currents drive vertically sheared exchange flows (Welander, 1957; Cushman-Roisin and Malačič, 1997; Birchfield, 1973). Studies of bottom Ekman dynamics must often make important considerations regarding the form of the eddy viscosity (Mofjeld, 1988; Perlin et al., 2005b) and the ratio of the local depth to the theoretical Ekman layer thickness Jenter and Madsen (1989); Kämpf (2015). The goal of Chapter 3 is therefore to understand the nature of the cross-shore exchange in the strong alongshore flow scenarios of Chapter 2 through an application of bottom Ekman dynamics in shallow water. Finite differences of the classical Ekman balances are used to produce a theoretical solution for the resulting velocity profiles in the context of an unstratified coastal domain. Results from this theoretical solution are then compared to those from a primitive equation numerical model (ROMS), to discern the dynamical effects of a sloped bottom and nonlinear advection of momentum in the governing equations.

Chapter 1

High frequency temperature variability reduces the risk of coral bleaching

1.1 Introduction

Coral reef ecosystems provide subsistence nutrition, coastal protection, and revenue from tourism to hundreds of millions of people globally (West and Salm, 2003; Hoegh-Guldberg et al., 2007), and are valued at trillions of dollars annually (Costanza et al., 2014). Especially during recent years, coral reefs are increasingly threatened by accelerated rises in ocean temperatures owing to global warming (Van Hooidonk et al., 2016; Hughes et al., 2017; Grottoli et al., 2006). Elevated seawater temperatures are the primary cause of mass coral bleaching (Hughes et al., 2017; Glynn, 1993), or the loss of pigmentation due to the collapse of the symbiotic relationship between the coral host and its endodermal dinoflagellate algae (zooxanthellae) (Glynn, 1993; Goreau and Hayes, 1994). Bleached corals are susceptible to

disease (Jokiel et al., 2004) and reduced carbonate accretion (Jokiel et al., 2004; Cantin and Lough, 2014), and prolonged bleaching will lead to mortality (Hughes et al., 2017; Dunn et al., 2004; Berkelmans et al., 2004). Thermal stress on corals and regional bleaching events are most often predicted by the magnitude and duration of remotely sensed sea surface temperatures (SSTs) above a fixed, locally defined average summer threshold temperature (Hughes et al., 2017; Goreau and Hayes, 1994; Goreau et al., 2000). A conventionally used metric for quantifying these temperature anomalies is provided by the National Oceanic and Atmospheric Administration's (NOAA) Coral Reef Watch program, which has reported cumulative thermal stress on reefs twice a week since 1997 (Liu et al., 2014). Furthermore, bleaching predictions from remotely sensed temperatures can be improved by including SST-based calculations of interannual temperature variability (Donner, 2011; Logan et al., 2012) and coral sensitivity to thermal stress exposure (Boylan and Kleypas, 2008). However, the relatively coarse spatiotemporal resolution of the remotely sensed data prevents ensuing thermal stress quantifications from identifying the often observed significant spatial heterogeneity in bleaching that occurs within reef regions and individual reefs (DeCarlo et al., 2017; Oliver and Palumbi, 2011; Guadayol et al., 2014). The response of reefs to temperature at these smaller spatial scales is complex and putatively depends on a combination of organism-level and reefscale factors such as coral life-history strategies and stressor cotolerances (Darling et al., 2013), the history and duration of thermal stress exposure (Berkelmans, 2002; Middlebrook et al., 2008), the rate of change in seawater temperature (Middlebrook et al., 2010; Chollett et al., 2014), flow conditions (McClanahan et al., 2005), heterotrophic feeding (Grottoli et al., 2006), turbidity (Williams et al., 2010), and the intensity and history of exposure to solar radiation (Lesser and Farrell, 2004; Brown et al., 2000). In turn, many of these environmental conditions are mediated by reef-scale factors such as waves (Lentz et al., 2016), winds, tides (Leichter and Miller, 1999), and daily heating and cooling (Davis et al., 2011). Site-specific studies suggest that historical temperature variability within diurnal time scales affects corals' physiological tolerance (Oliver and Palumbi, 2011;

McClanahan et al., 2005; Carilli et al., 2012; Palumbi et al., 2014) and performance (Castillo et al., 2012) under thermal stress. For example, it has been theorized that corals located in areas characterized by large temperature fluctuations, such as reef flats or shallow lagoons, may be better acclimatized or adapted to thermal stress, and therefore more resistant to anomalous temperatures and bleaching, than corals in areas where temperatures are more stable, such as on reef crests or reef slopes (Barshis et al., 2013; Rogers et al., 2016; Schoepf et al., 2015). Other studies have suggested that water temperatures in the weeks or months leading up to peak temperatures are critical in determining the coral physiological response. A recent analysis of experimentally heated corals from the Great Barrier Reef showed that bleaching and cell death responses were indeed lower when the thermal exposure included a moderate pre-stress followed by a short recovery period (i.e., a "protective temperature trajectory") (Ainsworth et al., 2016). Depending on intrinsic properties of coral physiology (Swain et al., 2016) such as energy reserves and algal phenotypic plasticity (Grottoli et al., 2014), pre-peak temperatures may either protect against or exacerbate bleaching at peak temperatures (Grottoli et al., 2014). Taken together, a growing body of evidence thus suggests that historical temperature variability, and particularly, "high-frequency" temperature variability, which we define as occurring within diurnal or shorter periods, may play an important role in determining corals' physiological responses to thermal stress and thereby reef-scale vulnerability to bleaching. In turn, a better understanding of reef-scale bleaching risk factors could help coastal management efforts to identify natural refugia and may be important for the recovery of coral communities following a bleaching event (Riegl and Piller, 2003).

Here, using a global suite of in situ data, we compare and assess the ability of 20 commonly used environmental variables and 7 remotely sensed variables to explain observed bleaching prevalence, testing the hypothesis that including high-frequency temperature variability as one of these model variables will lead to more accurate predictions. Analyzed data include records of in situ temperature time series at 118 reef locations from five major

reef regions with sampling intervals of $\leq$3 h and continuous measurements of $\geq$1 year, as well as precise information on habitats and depths (Appendix B), along with 81 spatially and temporally coincident, quantitative coral bleaching observations (Appendix C). Each of the 81 bleaching observations was matched to its own spatiotemporally coincident temperature time series data, such that 46 of the 118 temperature time series were used in the subsequent bleaching analysis. Bleaching observations, which are most often reported as the average percent of colony or transect area bleached, were standardized to ordinal-valued "bleaching prevalence scores" (1: $\leq$10%; 2: 10$-$25%; 3: 25$-$50%; 4: $>$50% of reef area bleached), representing mild to pervasive bleaching, respectively (**Methods**). The influence of different factors on bleaching prevalence scores are evaluated by selecting covariates from a pool of 20 explanatory variables (depth, latitude, and 18 thermal metrics) grouped into 8 categories of metrics often used to predict bleaching (Table 1.1). In addition to these in situ variables, we also include 7 analogous and conventional remotely sensed SST thermal stress metrics (Table 1.1). After standardizing all covariates and fitting them to ordinal-valued bleaching prevalence scores using ordinal logistic regression (OLR) models (**Methods**), we conclude that high-frequency temperature variability, specifically the average daily temperature range (DTR) of the 30 days preceding a bleaching observation, is the most influential covariate in predicting the bleaching response, and serves to attenuate the prevalence of bleaching.

1.2 Results

1.2.1 Variation among in situ explanatory variables.

A principal components analysis (PCA) displays the projection for each site onto the 2D plane that accounts for the most variance in the 20 in situ explanatory variables (Fig. 1.1),

Category	Variable [Units]	Identifier	Description	Ref.
1. Depth	Instrument depth[m]	depth	In situ water depth of instrument	
2. Background Conditions	Latitude [DD]	lats	Latitude of instrument	
	Maximum Monthly Mean (MMM) [°C]	MMM_{Total}	Maximum of monthly mean climatology from entire time series	Liu et al. (2006)
		MMM	Maximum of monthly mean climatology using data only before and during bleaching event	
		MMM_{4km}	Maximum of monthly mean climatology using 4 km weekly CoRTAD SST data	
		MMM_{Max}	Mean of maximum monthly SST from each year in climatological time period	Donner (2011)
3. Cumulative Thermal Stress	Degree Heating Weeks (DHW) [°C-weeks]	DHW_{90}	Trapezoidal integration of temperatures in excess of MMM + 1 °C during 90 days preceding a bleaching event	Liu et al. (2006)
		DHW_{30}	Trapezoidal integration of temperatures in excess of MMM + 1 °C during 30 days preceding a bleaching event	
		DHW_{4km}	Degree heating week product from 4 km weekly CoRTAD SST data	
	Cumulative Summer Anomaly (CSA) [°C-days]	CSA_{Total}	Trapezoidal integration of temperatures in excess of MMM + 1 °C during all summer periods through entire time series	
		CSA_{Before}	Trapezoidal integration of temperatures in excess of MMM + 1 °C during summer periods before and during a bleaching event	
		CSA_{During}	Trapezoidal integration of temperatures in excess of MMM + 1 °C during summer of bleaching event	
4. Acute Thermal Stress	Presence/absence of acute temperature anomaly [binary]	Acute1	Binary value indicating whether any of the daily mean temperatures within 90 days preceeding a bleaching event exceeded MMM + 1 °C	
		$Acute1_{4km}$	Acute1 computed using 4 km weekly CoRTAD SST data	
		Acute2	Binary value indicating whether any of the daily mean temperatures within 90 days preceeding a bleaching event exceeded MMM + 2 °C	
		$Acute2_{4km}$	Acute2 computed using 4 km weekly CoRTAD SST data	
5. Thermal Trajectory	Type of induced thermal tolerance prior to acute thermal stress, using twice-weekly averaged temperatures [ordinal]	TT	0: No thermal stress (temperatures do not exceed MMM + 2 °C within 90 days prior to survey date)	Ainsworth et al. (2016)
			1: Protective Trajectory (temperatures exceed MMM, then have a recovery period below MMM for at least 10 days prior to exceeding MMM + 2 °C)	
			2: Single Bleaching Trajectory (temperatures exceed both MMM and MMM + 2 °C without a 10-day recovery period in between)	
			3: Repetitive Bleaching Trajectory (temperatures exceed MMM + 2 °C in two peaks separated by 9 days)	
6. Heating Rate	Rate of spring-summer temperature change [°C/day]	$ROTC_{SS}$	Mean rate of temperature change during spring and summer of all years	Chollett et al. (2014)
		$ROTC_{90-4km}$	Mean rate of temperature change during 90 days preceding a bleaching event using CoRTAD SST data	
		$ROTC_{SS-4km}$	Mean rate of temperature change during spring and summer of all years using CoRTAD SST data	
7. High-Frequency Temperature Variability	Daily Temperature Range (DTR) [°C]	DTR_{Total}	Mean DTR over entire time series	
		DTR_{SS}	Mean DTR of all spring and summer periods	
		DTR_{FW}	Mean DTR of all fall and winter periods	
		DTR_{90}	Mean DTR over 90 days preceding a bleaching event	
		DTR_{30}	Mean DTR over 30 days preceding a bleaching event	
8. DTR Distribution Shape	Measure of shape of distribution of all DTR values w/in a time series [−]	kurtosis	Kurtosis of full time series of DTR values	
		skewness	Skewness of full time series of DTR values	

Variables are grouped according to eight categories representing different aspects of ecologically relevant environmental and temperature factors. Seasons were defined such that each season spanned three complete months, and austral and boreal summers were December through February and June through August, respectively

Table 1.1: List of explanatory variables used in the ordinal logistic regression analysis

and the locations of the loading vectors reveal how these explanatory variables relate to their respective groupings. The first principal component accounts for 44.2% of the variation in the explanatory variables, and is largely driven by high-frequency temperature variability and cumulative thermal stress.

1.2.2 Spatiotemporal dependence of diurnal temperature variability.

The thermal metrics computed from temperature time series were highly variable across sites, but regardless of location and depth, all 118 time series show significant temperature variations in the high-frequency band (Supplementary Note A.1; Fig. A.1), which we define as 0.727-4 cycles per day (cpd). Power spectra of temperature variations were calculated for each location, and the ratios of high-frequency band to seasonal band (0.012-0.143 cpd, or 1/7 to 1/84 days) variance in these spectra were used to characterize the relative importance of variance within the high-frequency band. This ratio correlates with the inverse of depth ($r = 0.381$, Student's t-test $p < 0.05$), indicating that the relative contribution of high-frequency variability to the variance within a temperature time series is stronger at shallower sites (Fig. A.2a). At back reef, reef flat, and reef slope habitats, these ratios were on average 1.83, 0.68, and 0.44, respectively, while across all locations, this ratio was 1.02 (Fig. A.2b). Furthermore, these ratios differed significantly among the three habitats (Kruskal-Wallis, $\chi^2 = 24.66$, df = 117, $p < 0.05$; Fig. A.2b). Although the magnitude of diurnal temperature fluctuations varies by location, the ubiquity and prominence of temperature variance in this frequency band indicated by these average ratios reflects the importance of some common physical forcing processes governing the flow and heating of reef waters, such as diurnal solar heating, tides, winds, and waves (Leichter and Miller, 1999; Davis et al., 2011; Lowe et al., 2016; Herdman et al., 2015).

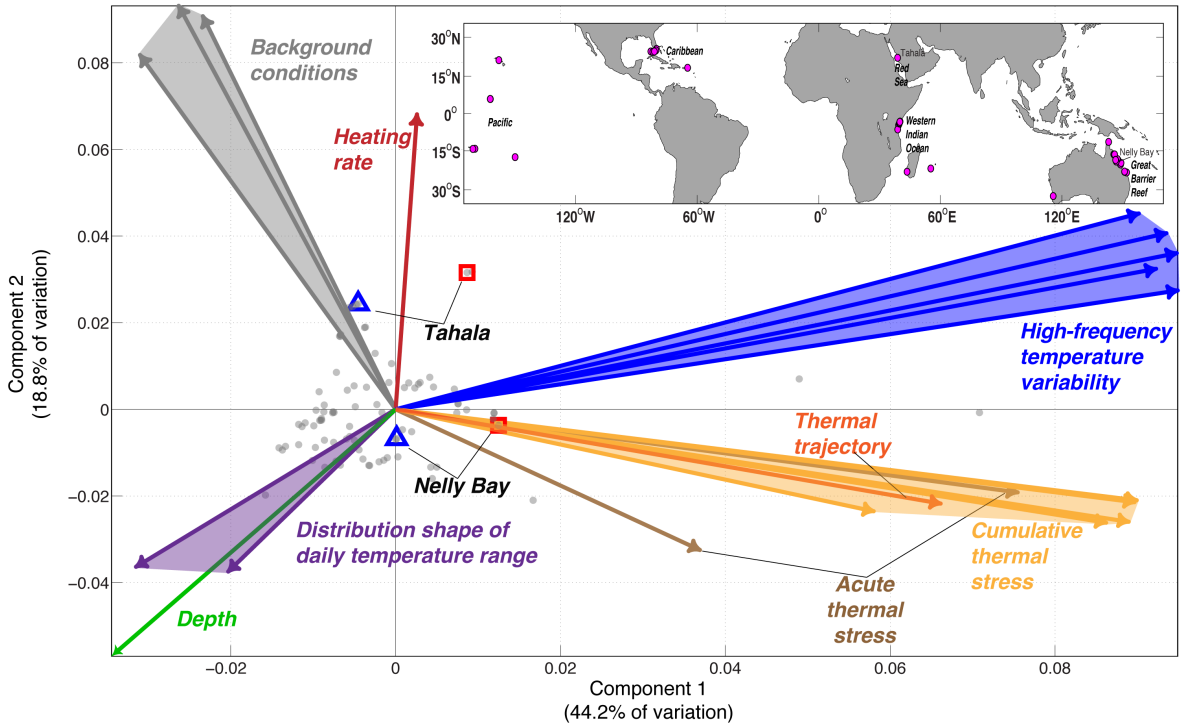

Figure 1.1: First two axes of variation of site-specific explanatory variables. Biplot of principal components analysis (PCA) showing the first two components (44.2% and 18.8%, respectively) that explain the majority of the variance in the matrix of 20 in situ explanatory variables (Table 1.1) used to explain bleaching prevalence. The light gray dots ("scores") each represent temperature time series associated with a distinct bleaching event at a given reef site. Gray dots that are close to each other have more similar temperature environments than dots further apart. The vectors are colored according to the categories described in Table 1.1. The time series inspected later in Fig. 1.4 are also indicated by red squares (Tahala and Nelly Bay shoreward habitats) and blue triangles (Tahala and Nelly Bay seaward habitats). The magenta circles in the inset map indicate the locations of all 118 in situ time series, with their associated reef regions labeled. The map was created using the MATLAB package "M_Map", created by Rich Pawlowicz under the license Copyright (c) 2014, Chad Greene. All rights reserved

Power spectra of six representative time series from different reef regions (Fig. 1.2a) show a broad range of temperature variability from annual to hourly periods (see Fig. A.1 for other spectra). Yearly composites of mean water temperature and DTR (Fig. 1.2b) both show prominent seasonal cycles (Supplementary Note A.2): the magnitude of daily temperature fluctuations was seasonally dependent (Kruskal-Wallis, $p < 0.01$) for 96% of reefs in our study (113 of 118 time series), with maximum DTRs occurring most often in spring and summer months (74% of time series, Fig. A.3), and minimum DTRs occurring most often in fall and winter months (also 74% of time series, Fig. A.3). On global scales ($\sim$103 km), latitudinal gradients in solar forcing drive variations in seasonal temperature patterns on reefs (Fig. A.4), but there is also considerable heterogeneity in thermal environments at reef-scales ($\sim$102 m) due to variation in depth and circulation (Davis et al., 2011; Riegl and Piller, 2003; Craig et al., 2001). The differences in thermal environments at reef-scales are often greatest in the high-frequency band (daily and tidal timescales; Fig. 1.2c). Dramatically different thermal environments can be found at locations separated by 10s or 100s of meters on a reef, as illustrated by 7-day temperature time series from various locations on the same island, or different habitats within a given reef (Fig. 1.2c). For example, during a week in November 2009, two sites in American Samoa that are separated by <2 km and at similar water depths experienced average DTRs of 1.78 and 0.51 °C (Fig. 1.2c, sites OF3 and OF5 respectively).

Differences in the distributions of DTRs that distinguish microclimates within a reef system (e.g., thermally variable shoreward locations or thermally stable seaward ones) are reflected in the mean, skewness, and kurtosis of DTR values (Fig. 1.2d). Shallower and more shoreward sites have a peak in their DTR distributions corresponding to a larger DTR value, and furthermore, their distributions take on more extreme values than those from sites in deeper and more seaward locations. For example, at Heron Island in the Great Barrier Reef, the mean DTR of 4.23 °C on the reef flat was over three times as large as that of the reef slope (Fig. 1.2d). The implications of these different thermal microclimates for resistance

to thermal stress and resilience to bleaching are discussed below.

1.2.3 The effect of diurnal temperature variability on bleaching.

Ordinal logistic regression ("logit") models were computed for all permutations of selecting at most one variable from each of the eight categories in Table 1.1 (a total of 10,367 models), with bleaching prevalence scores as the response variable. Corrected Akaike's Information Criterion (AIC_C) values were used to rank the logit models, where the model with the lowest AIC_C value was ranked the highest (Fig. 1.3b). The model coefficients indicate the association of tested variables with bleaching prevalence score, such that positive coefficients indicate a "mitigating" effect on bleaching prevalence, and negative coefficients an "exacerbating" effect on bleaching prevalence.

"High-Frequency Temperature Variability" (Table 1.1) was used to capture temperature variability on diurnal and shorter time periods, a metric that is important for characterizing differential reef- and habitat-scale microclimates (Oliver and Palumbi, 2011; Davis et al., 2011; Pineda et al., 2013). In the best model (Fig. 1.3a), high-frequency temperature variability, specifically the average DTR over the 30 days preceding a bleaching event (DTR_{30}, Table 1.1) was the most influential metric for predicting bleaching prevalence score, with greater daily temperature variability serving as a mitigating factor (Fig. 1.3b). Furthermore, among all models within 2 AIC_C units of the highest ranked model (i.e. $\Delta AIC_C = AIC_C - \min(AIC_C) \leq 2$, Fig. 1.3a), high-frequency temperature variability was both the greatest mitigating factor of bleaching prevalence score and the most influential covariate– more influential than widely used metrics of acute and cumulative thermal stress by a factor of 2 and 3 times, respectively (Fig. 1.3c). Using globally averaged values of explanatory variables, our highest-ranked logit model (Fig. 1.3b) implies that, in native units, a 1 °C increase from the mean DTR_{30} value would decrease the odds of more prevalent bleaching

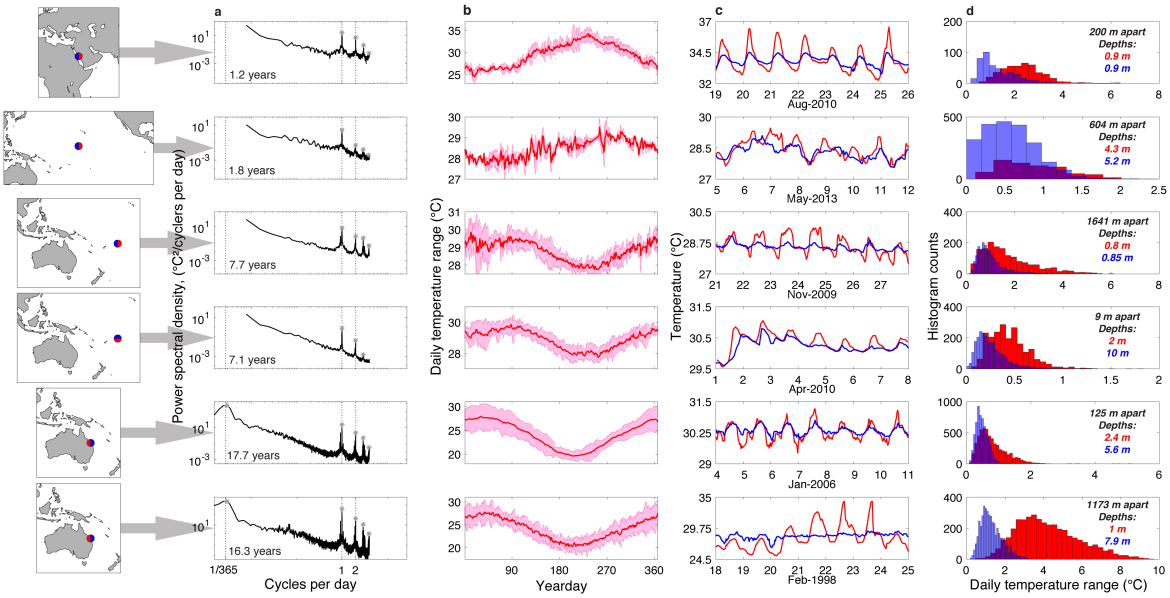

Figure 1.2: Temperature variability of six reef records. **a** Power spectra of temperature for TA3, P21, OF3, VT1, HW1, and HR1, with asterisks marking significant peaks, **b** yearly composites of mean daily temperatures and temperature ranges (red and pink shading respectively) for the same six time series in **a**, **c** 7-day trends in temperatures at two different habitats on the reef, and **d** histograms of daily temperature range at the same two habitats on each reef. In each case, reef locations are shown in maps on the left (for site information see Appendix B), the full duration of temperature records are indicated in **a**, and the great-circle distances between same-reef sites are indicated in **d**. The maps were created using the MATLAB package "M_Map", created by Rich Pawlowicz under the license Copyright (c) 2014, Chad Greene. All rights reserved

by a factor of 33. To standardize this, each unit increase in high-frequency temperature variability (i.e., DTR_{30}) would reduce the odds of more prevalent bleaching by a factor of $e^{2.66} = 14.3$. Contrasting this against a unit increase in cumulative thermal stress (i.e., DHW_{30}), which would only increase the odds of more prevalent bleaching by a factor of 2.6, highlights the dominant influence of diurnal temperature variability on reef-scale bleaching prevalence.

"Depth" (Table 1.1) was taken as the mean depth of the water temperature measurement, in meters below the surface, for each site, and is also representative of local water column depth as sensors were placed near the bed. Depth was the second-most effective predictor of bleaching prevalence (Fig. 1.3c), with deeper reefs less likely to experience pervasive bleaching. However, "depth" is also a proxy for other characteristics of the reef sites such as habitat (e.g., deeper forereefs and lagoons, shallow reef flats) and light intensity, which decays exponentially with depth. Although the logit models preclude significant collinearity of tested variables (**Methods**), corals at shallow depths may experience greater high-frequency temperature variability (Craig et al., 2001), although accounting for water flow can complicate this interpretation as it pertains to bleaching (McClanahan et al., 2005, 2007a). High-frequency temperature variability and depth may mitigate bleaching in complementary ways: habitats with greater high-frequency temperature variability, which are likely to be found at shallower depths (Craig et al., 2001), may develop greater thermal tolerance (Oliver and Palumbi, 2011; Castillo and Helmuth, 2005), while deeper coral habitats, despite their propensity for milder diurnal temperature variability (outside of internal wave-influenced regions (Davis et al., 2008; Davis and Monismith, 2011; Leichter et al., 2005)), may serve as refuge areas resistant to the intrusion of hot water (Chollett et al., 2014), perhaps facilitating recovery of coral cover following bleaching events (Graham et al., 2015).

"Background Conditions", "Cumulative Thermal Stress", and "Acute Thermal Stress" were the three explanatory variable categories largely suspected of exacerbating bleaching.

"Background Conditions" (Table 1.1) consisted of the average summertime, or maximum monthly mean (MMM), temperature, but computed from our in situ time series data, as opposed to conventional remotely sensed SST data (Liu et al., 2014). "Background Conditions" also included the latitude of the temperature logger, a variable that served as a proxy for unresolved oceanographic factors (McClanahan et al., 2007b) related to the large-scale processes that influence climatologies. The "Cumulative Thermal Stress" category (Table 1.1) encompassed various methods for the computation of the magnitude and duration of acute in situ thermal stress exposure on reefs. Similar to the MMM, cumulative thermal stress is traditionally derived from remotely sensed SSTs and is among the most common metrics used to predict coral bleaching (Chollett et al., 2014; Carilli et al., 2012). The "Acute Thermal Stress" category (Table 1.1) was included as a safeguard to differentiate sites with temperatures that may not have exceeded MMM+1°C (i.e. no thermal stress) yet still experienced bleaching. Consistent with the well established perspective that anomalously high temperatures are the primary cause of coral bleaching (Glynn, 1993), among our highest ranked models, bleaching was most exacerbated by greater cumulative and acute thermal stress, and also, to a lesser degree, by increases in MMM temperature and heating rate (Chollett et al., 2014). "Heating Rate" (Table 1.1) was the average rate of change in spring to summer temperatures, which is believed to have a positive relationship with bleaching-induced tissue damage, and this time period has been shown to be crucial for determining the fate of corals to summertime bleaching susceptibility (Chollett et al., 2014). The "Thermal Trajectory" (Table 1.1) category followed the methodology of a previous study that highlighted the role of protective warm, pre-stress temperatures as being important for resilience to bleaching from intense acute stress temperature events (Ainsworth et al., 2016). Our results reinforce recent findings that a reef's thermal trajectory is a significant predictor of bleaching prevalence (Ainsworth et al., 2016) (Fig. 1.3c), with thermal tolerance conferred by exposure to a protective, sub-lethal bleaching stress prior to acute stress exposure. Although not as influential as the above variables, a no-stress or protective thermal trajectory (i.e., a pre-stress,

sub-bleaching warming period, followed by a cooler recovery period) is more likely to result in lower bleaching prevalence than a single bleaching trajectory (temperatures that cross the bleaching threshold without a prior protective event) or a repetitive bleaching trajectory (Fig. 1.3b, c and Table 1.1). Finally, the "Shape of DTR Distribution" category (Table 1.1) was used to capture the skewness and kurtosis of DTR values derived from each time series to represent the symmetry and tail-density of DTR distributions. While these variables were not present in any of the highest ranked models, kurtosis and skewness of temperature time series have been associated with site-specific increased thermal tolerance (Baker et al., 2013).

To summarize the results of our highest-ranked logit model, we can examine how manipulating each covariate, while holding all others at their mean values, will change the probability of bleaching (Fig. 1.4). For example, a 0.88 °C decrease in high-frequency temperature variability (DTR_{30}) from its mean value would increase the probability of Category 4 bleaching from 12% to 75%, for a change of 63% (Fig. 1.4a), and a depth decrease of 5 m would increase this probability by 41% (Fig. 1.4b). Similarly, a 0.03 °C/day increase in $ROTC_{SS}$ from its mean value would increase the probability of Category 4 bleaching by 34% (Fig. 1.4c), and a 1 °C-weeks increase in DHW_{30} would increase this probability by 44% (Fig. 1.4f).

To broaden the applicability of our conclusions, we repeated the OLR analysis, with the addition of remotely sensed SST-derived covariates, to determine how the results would differ from the in situ driven models. We obtained weekly 4 km resolution CoRTAD SST data (Casey et al., 2015), using the data pixels closest to the coordinates of our in situ loggers, and used this SST dataset to compute covariates within the Background Conditions, Acute and Cumulative Thermal Stress, and Heating Rate categories (Table 1.1). This resulted in an improved highest ranked model (**Methods**), that included six covariates, three of which (MMM, DHW, Rate of Temperature Change) were computed using the SST, as opposed to in situ, data (Fig. 1.5a). However, similar to the highest-ranked model fit to exclusively

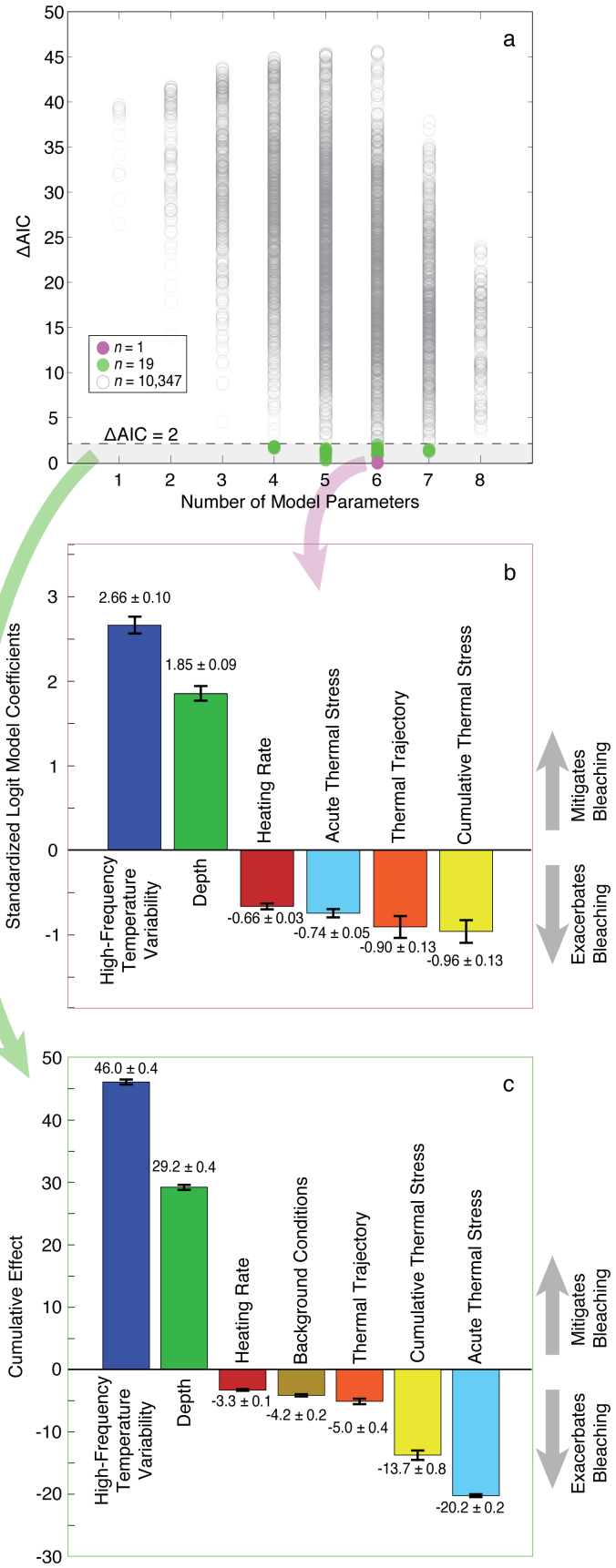

Figure 1.3: In situ explanatory variables of bleaching and their standardized logit coefficients with greatest predictive power. **a** ΔAIC_C, computed as AIC_C - $\min(AIC_C)$, values of all 10,367 runs of an ordinal logistic regression model, where models within $\Delta AIC_C \leq 2$ (dashed line and gray shaded region) are statistically indistinguishable, of which there were 20. **b** The best model (i.e. $\Delta AIC_C = 0$) included six variables, of which high-frequency temperature variability was the absolute most influential and also greatest mitigating factor to bleaching prevalence. **c** Summing across 20 indistinguishably good models (i.e. within $\Delta AIC_C \leq 2$), high-frequency temperature variability was consistently most influential. Variable categories are shown in Table 1. Delete-1 jackknife standard error bars are shown in (**b**), while the standard error bars shown in (**c**) were obtained by summing in quadrature the individual standard errors from each of the 20 models computed after delete-1 jackknife resampling

in situ data, covariates representing High-Frequency Temperature Variability, specifically DTR_{30}, and depth were again the dominant drivers of bleaching, and served as mitigating factors (Fig. 1.5a, b). Similarly, among covariates that exacerbated bleaching, Acute and Cumulative Thermal Stress provided the strongest influence (Fig. 1.5a, b), while Background Conditions (MMM_{4km}, Table 1.1) represented a mild exacerbating effect. A notable difference occurring in these new models was the opposite effect Heating Rate had from before; whereas in the exclusively in situ models, Heating Rate exacerbated bleaching, these SST-based models imply stronger heating rates serve to mitigate bleaching. Ultimately, these SST-based OLR models indicate that upon consideration of the consistent importance of DTR to bleaching, a globally available remotely sensed metric for diurnal temperature variability would be valuable for improved bleaching predictions.

1.2.4 Specific reef cases.

Our results reveal the importance of high-frequency temperature variability at locations worldwide, but include reef-scale observations where such variability influences bleaching prevalence of corals in different locations of the same reef during the same bleaching event (Davis et al., 2011; Pineda et al., 2013). Here, we present two such case studies: one from Tahala Reef, a platform reef in the central Red Sea, and another from Nelly Bay, a fringing reef in the Great Barrier Reef in Australia (Fig. 1.6). These sites were chosen due to the availability of additional meteorological data (Davis et al., 2011; Marshall and Baird, 2000) at these reefs. At each location, temperature time series (Fig. 1.6a, b) for both a seaward and a shoreward location show that, whereas low-frequency variations in water temperature are often very similar over reef-scales (Fig. 1.6c, d), high-frequency variations may be quite distinct (Fig. 1.6e, f). In these cases, bleaching events were more widespread and severe at the seaward locations where DTRs were smaller (Fig. 1.6a, b), consistent with our best logit models.

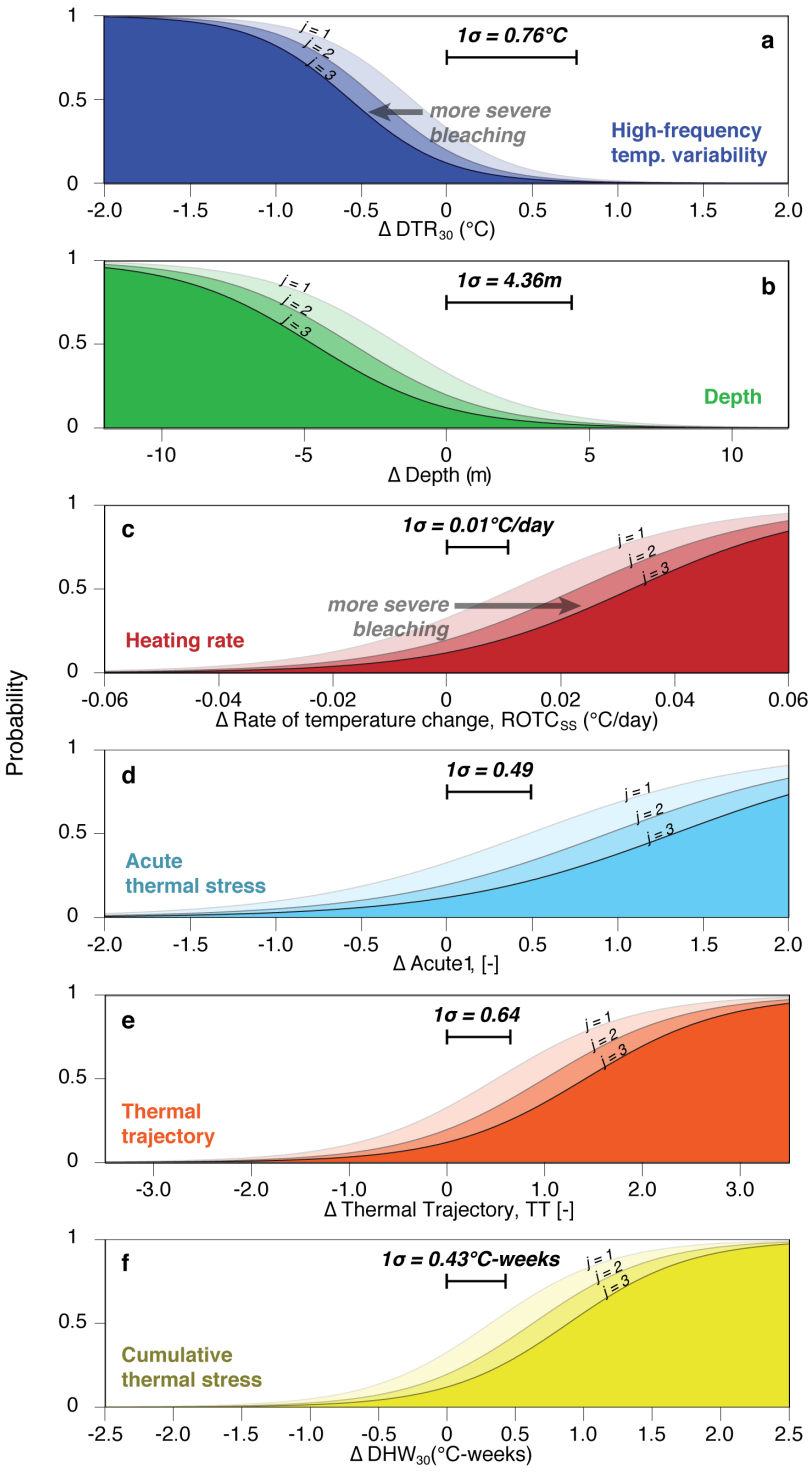

Figure 1.4: Influence of each in situ covariate on bleaching. Using the covariates from the highest-ranked logit model, the probability of observing bleaching prevalence greater than the jth category is plotted against changes in each covariate from their respective mean values (where 0 corresponds to the mean value), while keeping all other covariates at their mean values. Bleaching prevalence categories are defined as 1: $\leq$ 10%; 2: 10-25%; 3: 25-50%; 4: $>$ 50% of reef area bleached. Highest-ranked model covariates include: (**a**) High-frequency temperature variability (DTR_{30}), (**b**) Depth, (**c**) Heating Rate ($ROTC_{SS}$), (**d**) Acute Thermal Stress (Acute1), (**e**) Thermal Trajectory (TT), and (**f**) Cumulative Thermal Stress (DHW_{30}). Standard deviations for each covariate within our data set are also indicated

1.3 Discussion

For corals, a shift in thermal tolerance can occur due to adaptation of the coral animal or algal symbionts through natural selection of heat-tolerant lineages (Berkelmans and Van Oppen, 2006; Rowan, 2004), or physiological acclimation through the expression of heat shock proteins and regulation of apoptosis (i.e., programmed cell death) (Middlebrook et al., 2008; Barshis et al., 2013). As discussed, recent work highlights the importance of short-term temperature history (daily-weekly periods) for coral acclimatization to higher temperatures (Oliver and Palumbi, 2011), such that corals subject to warmer than average temperatures prior to thermal stress may exhibit a greater tolerance to acute temperature stress (Middlebrook et al., 2008). In the context of these studies and in keeping with other site-specific and experimental studies (Oliver and Palumbi, 2011; McClanahan et al., 2005; Craig et al., 2001; McClanahan et al., 2007a, 2009), our results suggest that temperature fluctuations on daily or tidal timescales are often sufficient to expose corals to temperatures high enough to encourage greater tolerance (via acclimation or adaptation) to thermal stress, but for time periods short enough to avoid mortality (Oliver and Palumbi, 2011; Castillo and Helmuth, 2005). Further, our results establish that the resistance of corals located in areas of high-frequency temperature variability to bleaching occurs in reef regions throughout the world. While we lack sufficient species-level data, we fully acknowledge that intrinsic coral properties (Swain et al., 2016), differences in reef-scale community compositions (Marshall and Baird, 2000), and taxonomic susceptibility (McClanahan et al., 2005) are likely to influence heterogeneous reef-scale bleaching responses, and an improvement to our model framework would include species-level covariates.

Our results also demonstrate the potential to both improve predictions of bleaching and anticipate heterogeneous patterns in bleaching prevalence at reef-scales, considering that beyond mean values, accounting for variability in temperature regimes yields better predictions of organismal responses to anomalous environmental events (Sheldon and Dillon, 2016).

Although SSTs from satellite remote sensing are not yet available at the spatiotemporal resolution required to calculate reef-scale high-frequency temperature variability, observational work on a range of reef structures suggests that it may be possible to predict reef-scale thermal environments using relatively simple hydrodynamic models given readily available bathymetry and basic hydrographic data such as tidal range, wave height, and offshore mean SST (Lentz et al., 2016; Davis et al., 2011; Lowe et al., 2016). While we did not assess other biogeochemical parameters, it is worth noting that the same physical circulation that drives spatially variable thermal environments, in locations with an active benthic community, can also create dynamic oxygen, pH, and nutrient environments (Falter et al., 2013; Gruber et al., 2017).

Urgent global efforts at reducing anthropogenic greenhouse gas emissions must remain a priority for reef preservation, due to the acute thermal stress that is now arising from global warming projections on reefs (Hughes et al., 2017; Selig et al., 2012). However, combating the effects of local stressors on reefs through conservation tools such as marine protected areas is likely to increase the chances of reef persistence through future warming, as well as to facilitate recovery following a bleaching event (Hoegh-Guldberg et al., 2007; Graham et al., 2015; Baker et al., 2008; Mellin et al., 2016). Warming ocean temperatures are projected to result in annual severe bleaching regimes by the middle of this century, with spatial variability in the onset of these events on the order of ± 10 years (Van Hooidonk et al., 2016). Considering our results in the context of this inevitable and persistent acute thermal stress, focusing management efforts on the more resistant reef locations that also experience delayed onsets in annual severe bleaching would maximize the likelihood that at least some healthy reefs will exist in the future.

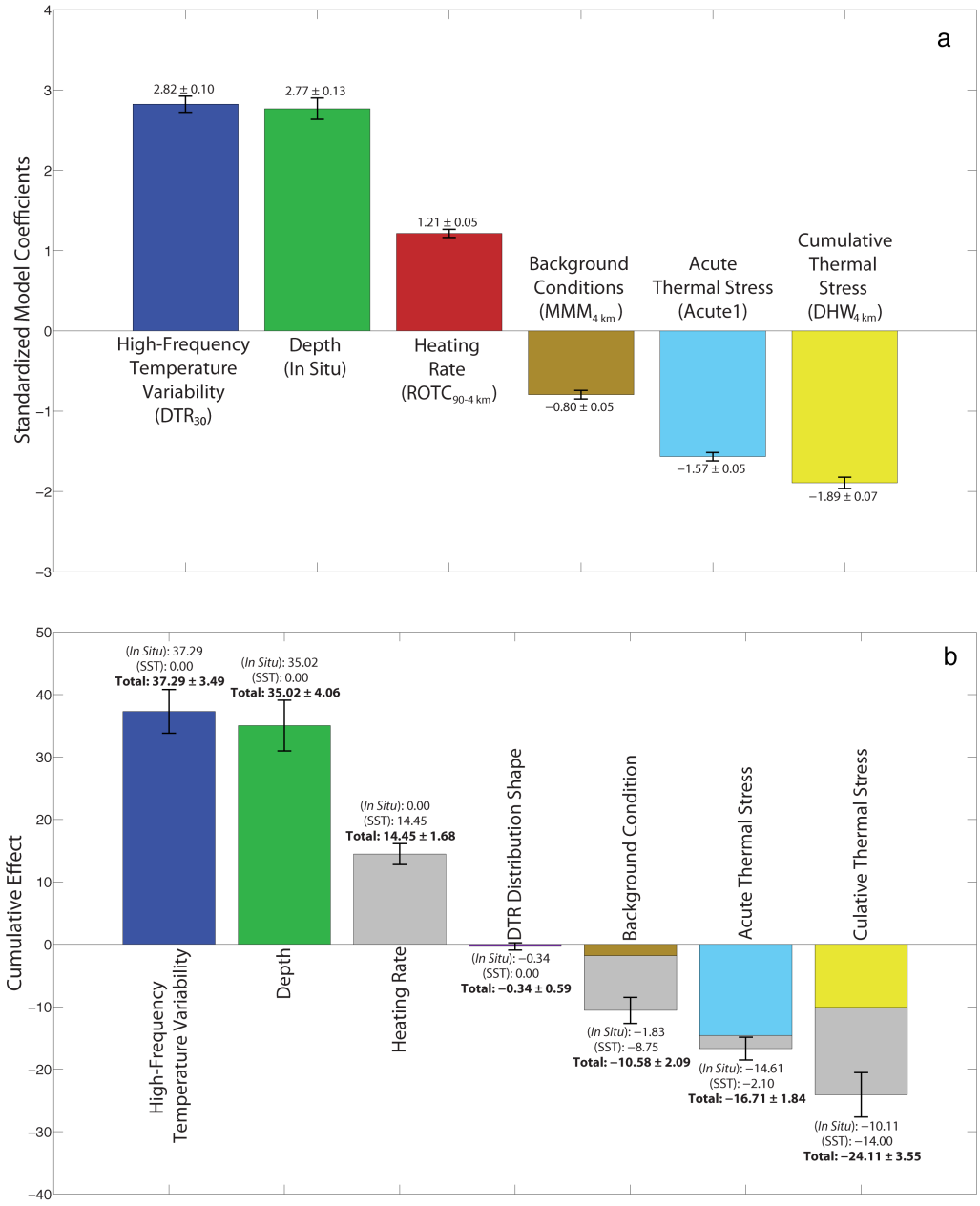

Figure 1.5: Remotely sensed SST OLR results. **a** Parameter estimates for standardized model coefficients of the covariates used in the highest-ranked OLR model when weekly 4 km CoRTAD SST-based variables are added to the pool of possible covariates; standard error bars were computed from delete-1 jackknife resampling. **b** The summation of the standardized covariate coefficients grouped by category from the highest-ranked models when including CoRTAD SST-based covariates; the standard error bars shown are obtained by summing in quadrature the individual standard errors computed after delete-1 jackknife resampling. The remotely sensed SST-based covariate contribution to each Cumulative Effect is colored gray

1.4 Methods

1.4.1 Data synthesis.

Water temperature time series from 118 locations, representing five major ocean basins where tropical coral reefs are found (Western Indian Ocean, Pacific Ocean, Caribbean Sea, Great Barrier Reef, and Red Sea), were obtained from existing records of in situ temperature data. Many of these time series were obtained directly from the researchers (Appendix B), or from publicly available databases including the Australian Institute of Marine Science (AIMS), the National Data Buoy Center (NDBC), and the Florida Institute of Oceanography (FIO). However, time series within our dataset were also selected to match precise reef locations that had sufficiently documented bleaching events, while also containing as long and consistently sampled records as possible. Site names and three-letter codes, locations, depths, instrument descriptions, and additional information for each time series are listed in Appendix B, which also lists the source for each time series. Water temperature records included in this analysis spanned at least 12 months in duration, with a sampling interval less than or equal to 3 h. In cases where instrument substitution resulted in varying sampling intervals, time series were sub-sampled to the largest of these intervals, or, in rare cases, interpolated to remain below a 3 h sampling interval. The temperature time series data used in this study originate from instruments that were calibrated using varying methodologies, such as by placing loggers together at one location and comparing recorded temperatures with a reference temperature dataset, ice bath calibration, or multiplying raw field recorded temperatures by normalized logger calibration coefficients. Our analysis is largely based on relative temperature variations, however, so that absolute temperature accuracy will not affect the results presented here. In an effort to examine how representative our sample temperature time series data was, we used one-sample t tests to compare the overall means and extremes of our data to a global temperature data set taken from nearly 1000 reef locations (Kleypas et al., 1999).

From these tests, we cannot conclude any significant differences ($\alpha = 0.05$) between our time series data and this larger global data set. All data analyses were done using MATLAB 7.14 (The Mathworks, Natick, MA, USA).

1.4.2 Spectral analysis.

Power spectral density (PSD) estimates were computed for each temperature time series. First, if necessary, temperature time series were resampled or linearly interpolated to maintain a constant sampling interval, chosen to be 3 h so as to resolve spectral frequencies of up to 4 cpd. In order to examine temperature variability for a broad range of frequencies spanning annual to diurnal and shorter periods, a PSD was calculated as follows: time series greater than or equal to 10 years in duration were divided into 3-year sections, while all others were divided into 4-month sections. Sections were overlapped by 50% and windowed with a Hamming function before spectra for each section were calculated, which were then ensemble averaged to obtain the PSD estimate. The statistical significance ($\alpha = 0.05$) of observed spectral peaks was ascertained by comparison with the upper confidence level of a background red noise fit to the spectrum (Warner, 1998). We empirically defined annual, seasonal, and diurnal frequency bands as 0.00185 to 0.0111, 0.0119 to 0.143, and 0.727 to 1.333 cycles per day (cpd), respectively. Band variance was computed using trapezoidal integration of PSD values within each respective frequency range, and ratios of high-frequency to seasonal band variances among habitat types ("Back Reef", "Reef Flat", "Reef Slope") were compared using a Kruskal-Wallis test (Fig. A.2b).

1.4.3 Spatiotemporal variability in water temperature.

To quantify the magnitude of diurnal patterns of heating and cooling, a DTR was calculated as the difference between maximum and minimum temperatures for each day of each time

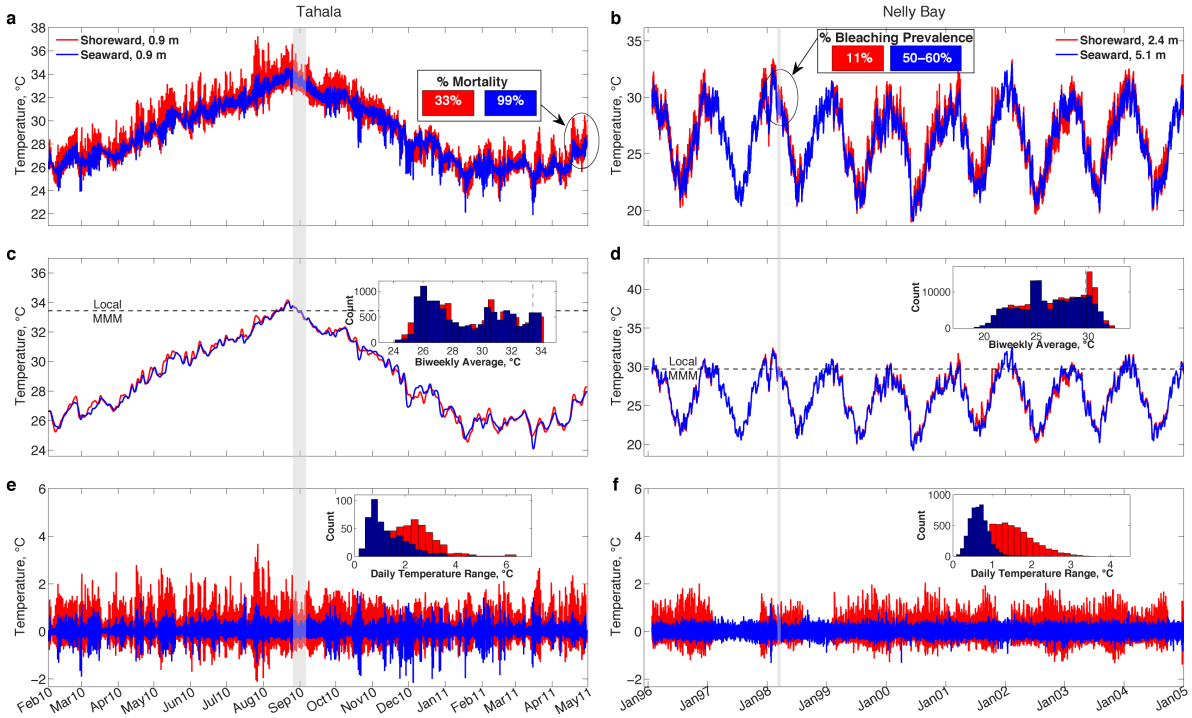

Figure 1.6: Same-reef case studies. **a** Temperature time series taken from the wave-exposed (blue) and wave-protected (red) edges of the Tahala reef platform in the Red Sea, which are separated by ∼200 m. The percentage of observed mortality, which was associated with the bleaching event in September 2010 (Pineda et al., 2013; Furby et al., 2013), is indicated for each corresponding platform edge. **c** 2-week low-pass filtered time series of the raw Tahala temperature data, with the Maximum Monthly Mean (MMM) temperature calculated using the in situ data for each time series. **e** 33-h high-pass filtered time series of the raw Tahala temperature data, with a histogram of the Daily Temperature Range (DTR) values for each time series. **b**, **d**, **f** Analogous versions of **a**, **c**, and **e**, respectively, but for the Nelly Bay reef flat (red) and reef slope (blue) habitats in the Great Barrier Reef, separated by ∼122 m. Bleaching prevalence as proportions of belt transects (Marshall and Baird, 2000) are also indicated in **b**. The gray bars highlight the approximate periods of reported bleaching events

series. Temporal variations in DTR values were examined in multiple ways. First, DTRs were composite-averaged for yeardays 1-366, and based on evident seasonal DTR variability from panel b of Figure 1.2, a non-parametric Kruskal-Wallis test was used to assess the seasonal dependence of DTR distributions (Green et al., 2010). Seasons were defined such that each season spanned 3 complete months, and austral and boreal summers were December through February and June through August, respectively. Temperature metrics are summarized in Table 1.1. Large-scale spatial patterns in water temperature variability relative to latitude were also characterized; annual temperature ranges, calculated as the range of monthly mean temperatures, were compared against latitude for all sites. Variance in high-frequency (33 to 6 h periods) and seasonal (7 to 84-day periods) spectral bands were computed via integration of their respective power spectral densities, and the ratios of high-frequency to seasonal variance for all time series were compared by the habitat from which each time series was recorded. Habitats were divided into three groups: (i) back reefs and back reef lagoons (labeled as "BR"), (ii) reef flats and non-back reef lagoons ("RF"), and (iii) reef crests, reef slopes, forereefs, and anything further offshore ("RS").

1.4.4 Bleaching data synthesis.

Coral bleaching observations (81 events) that corresponded in time and location with temperature data (Appendix C) were obtained from a variety of sources, but primarily from peer-reviewed publications. Bleaching reports were based upon various quantification schemes, but some common methods included recording bleaching as: (i) a proportion of transect area (Elvidge et al., 2004), (ii) severity among different colonies of different coral species (Baird and Marshall, 2002), and (iii) prevalence categories based on aerial (and ground-verified) surveys (Berkelmans, 2002). In publications that reported percentages of colony bleaching within different coloration and paling categories, we used the weighted average of the different percentages within each category, though the majority of bleaching records

naturally translated into our four bleaching prevalence scores. To aggregate or standardize the bleaching reports for use in this study, we defined a bleaching response variable in terms of percentage of spatial area bleached, and we therefore assigned the following categories as ordinal values of bleaching prevalence score: 1: "bleaching prevalence" $\leq 10\%$ ($n = 48$); 2: $10\% <$ "bleaching prevalence" $\leq 25\%$ ($n = 5$); 3: $25\% <$ "bleaching prevalence" $\leq 50\%$ ($n = 6$); 4: "bleaching prevalence" $> 50\%$ ($n = 22$). Note that bleaching events of 0 (reports of no bleaching observed or negligibly mild paling) are binned into bleaching prevalence score 1, to provide a conservative grouping for mild bleaching events, seasonal patterns of discoloration and variation in zooxanthellae densities (Fitt et al., 2000), unresolved "background bleaching" levels (Yee et al., 2008), and observation errors. As opposed to continuous interval variables, ordinal variables represent categorical values that can be ranked and have a natural ordering to them, offering the advantage of creating bins for ranges of values.

1.4.5 Explanatory variables.

To assess the influence of explanatory environmental variables, including high-frequency temperature variability, on bleaching response, we performed a multivariate statistical analysis of the observed bleaching events. As there are multiple aspects of thermal stress and environmental conditions that may explain the bleaching response, we selected 20 experimental variables for the ordinal regression (defined in Table 1.1), organized into eight broad categories: (1) Depth, (2) Background Oceanographic Conditions, (3) Cumulative Thermal Stress, (4) Acute Thermal Stress, (5) Thermal Trajectory, (6) Heating Rate, (7) High-Frequency Temperature Variability, and (8) Shape of the Distribution of HF Temperature Variability. We lacked sufficient habitat (i.e., reef flat, reef crest, reef slope, etc.) information at which many loggers were placed, and therefore did not include habitat as an explanatory variable. Environmental variables in the Cumulative Thermal Stress category were calculated from in situ temperature measurements rather than the remotely sensed National Oceanic and

Atmospheric Administration's Coral Reef Watch (NOAA CRW) products because many of our logger locations were outside of the coverage areas of the CRW Virtual Stations, and furthermore, as the first suite of CRW products was released in 2000, they do not include temperature data corresponding to the 1998 global bleaching event. The explanatory variables we use here are commonly appended with a subscript to indicate the period of time, relative to the bleaching observation date, used to calculate the metric. For example, the subscript "SS" denotes the spring to summer period, and the subscript "30" denotes the 30 days preceding (and including) a bleaching observation.

1.4.6 Principal components analysis.

Principal components analysis was performed to examine the spatial structure of the environmental forcings and determine the association between independent variables within each of the eight categories (Fig. 1.1). The first two PC axes accounted for 44.2 and 18.8% of the variance within the matrix of independent variables. The magnitude and orientation of the loading vectors indicate the importance of each parameter in describing the variance of the PCA components.

1.4.7 Computation of thermal trajectory and acute stress variables.

An ordinal-valued Thermal Trajectory (Ainsworth et al., 2016) variable was included as an independent variable to assess the degree to which environmental conditions confer thermal tolerance. The calculation of this was as follows: first the MMM and MMM + 2 °C (the latter quantity is referred to as the "local bleaching threshold") were computed for a given time series. Then the 33-h low pass filtered time series for the 90 days preceding a bleaching event

was inspected to determine the type of Thermal Trajectory. If temperatures exceeded the MMM, then fell below the MMM for a required 10-day "recovery period" before proceeding to exceed the local bleaching threshold, a Protective Trajectory with an ordinal value of 1 was recorded. If temperatures increased from below the MMM to above the local bleaching threshold, without a 10-day recovery period, a Single Bleaching Trajectory with a value of 2 was recorded. If temperatures exceeded the local bleaching threshold at least twice, with a required 9-day recovery period between threshold exceedances, a Repetitive Bleaching Trajectory with an ordinal value of 3 was assigned. Finally, if temperatures did not exceed the local bleaching threshold, an ordinal value of 0 corresponding to no thermal stress was assigned. Justification of our ordinal-value scheme comes from an analysis of experimentally heated corals from the Great Barrier Reef, whereby in the face of thermal stress, corals with a Protective Trajectory experienced localized cell death of approximately 30%, while that of corals under Single and Repetitive Bleaching Trajectories was approximately 60% and 70%, respectively (Ainsworth et al., 2016). Furthermore, experimental results showed that corals under a Protective Trajectory maintained significantly greater symbiont density than those under Single and Repetitive Bleaching Trajectories, and hence the ordinal scores from 0 to 3 aptly account for the monotonic nature of coral tissue detriment associated with no heat stress, a Protective Trajectory, a Single Bleaching Trajectory, or a Repetitive Bleaching Trajectory, respectively. The "No Thermal Stress" trajectory corresponded to $\sim$ 0% cell death and greater symbiont density than the Protective Trajectory.

The Acute Thermal Stress category was composed of two binary variables to indicate the presence/absence of acute thermal stress. The calculation of this was as follows: first the MMM + 1 °C and MMM + 2 °C were computed for a given time series, then the daily mean temperatures within 90 days before a bleaching event were inspected to determine if temperatures exceeded MMM + 1 °C (in which case Acute1 would equal 1) and MMM + 2 °C (in which case Acute2 would equal 1).

1.4.8 Ordinal logistic regression.

Using the eight explanatory variable categories described above, and bleaching prevalence scores from 1 to 4 as the response variable, we performed an ordinal logistic regression analysis to determine how the relative log odds of a given bleaching prevalence score depends on the interactions among the explanatory variables. Ordinal regression models have been adeptly used in ecological studies where data are often present as semi-quantitative variables in which relative differences between values are of importance (Schabenberger, 1995; Guisan and Harrell, 2000). Furthermore, logit functions have been previously implemented to predict the presence/absence of bleaching using gridded remote-sensed data (Yee et al., 2008; Yee and Barron, 2010), or to explain the influence of a range of environmental and coral physiological factors on reef ecosystem response following a disturbance (Graham et al., 2015). These logit models are multivariate extensions of generalized linear regression models (McCullagh, 1980), providing parameter estimates via maximum likelihood estimation (MLE) to model the relative log odds of, for our purposes, observing one bleaching prevalence score or less versus observing the remaining greater bleaching prevalence scores:

$$\ln\left(\frac{P(y_i \leq j)}{P(y_i > j)}\right) = C_j + B_1 z_{i1} + \ldots + B_p z_{ip} \tag{1.1}$$

Here i indexes each of N observations, with bleaching observation y_i, and the left-hand side quantity is referred to as the logit of the probability of observing bleaching prevalence score j or lower, for $j = 1$, 2, or 3 (observations with bleaching prevalence scores of 4 contribute to the regression through calculation of the log-odds). Note that the odds are defined as the ratio of the probability of an event occurring to the probability of the event not occurring, which is exactly the ratio inside the natural logarithm. Each C_j is an MLE-computed model intercept, and each B_k is the MLE coefficient corresponding to each standardized independent variable z_{ik}, for $k = 1, \ldots, p$, where p is the number of independent variables used in a given model. A fundamental component of this model is the assumption of proportional odds, or

parallel regression, which implies B_k values are independent of the logit level j. The validity of this parallel regression assumption was ascertained using Brant's Wald test (Brant, 1990), as well as a likelihood ratio test ($\alpha = 0.05$).

As each time series was the sole source of its explanatory variables, we can expect many of these variables to be correlated with each other (multicollinear). If left unaccounted for, multicollinearity obscures the interpretation of the explanatory variables and their coefficients, and may decrease the statistical power of the logit analysis (Graham, 2003). The degree of multicollinearity among the 20 explanatory variables used in the logistic regression was assessed by calculating the condition indices and variance-decomposition proportions (Belsley et al., 2005) of the matrix of explanatory variables. This revealed the following non-trivial multicollinearities: (1) DHW_{90} with CSA_{During}; (2) DTR_{90} with DTR_{30}; (3) MMM with MMM_{Total}; and (4) DTR_{Total} with DTR_{SS} and DTR_{FW} (Table 1.1). Note that within each of these four multicollinear groupings, the multicollinear variables come from the same explanatory variable category (for example, both DHW_{90} and CSA_{During} are both from the Cumulative Thermal Stress category). Therefore, for each logit model, we selected at most one variable from a category without multicollinearity erroneously influencing our results. Spatial autocorrelation within each covariate was determined by calculating Moran's I and examining correlograms, from which we determined significant spatial autocorrelation typically up to distances of 500 km (Fig. A.5). To account for this, we also added a random effect to the highest-ranked logit models, from which we failed to conclude a marginal model improvement (see below).

All permutations of all possible explanatory variables were used to compute a total of 10,367 logit models, where all logit models were computed using a multinomial logistic regression function ("mnrfit") in MATLAB. Model comparison was performed using a bias correction for small sample sizes to Akaike's Information Criterion, AIC_C(Hurvich and Tsai, 1989), and all models within $\Delta AIC_C \leq 2$ of the best model ($\Delta AIC_C = 0$), which have

statistically indistinguishable performances (Burnham and Anderson, 2002), are presented in Fig. A.6. McFadden's pseudo-R^2 was also computed for the highest ranked models, and ranged from 0.26 to 0.30, with that of the highest-ranked model equal to 0.30. While the logit model with the lowest $\mathrm{AIC_C}$, as well as all models within $\Delta\mathrm{AIC_C} \leq 2$, provide a general outline for the coefficients of the critical independent variables in explaining bleaching prevalence, these parameter estimates have errors of unknown distribution. Additionally, the possible existence of outliers in the high-frequency temperature variability data may influence the results of the logit parameter estimates, and therefore, delete-1 jackknife resampling was used to compute estimates of bias and standard errors. We found a slight positive bias that did not significantly alter the influence of high-frequency temperature variability relative to the other covariates. Estimates of standard errors for all logit parameters of all models within $\Delta\mathrm{AIC_C} \leq 2$ can be seen in standard error bars (Fig. 1.3b and Fig. A.6). Specifically, the error bars seen in Fig. 1.3c are the standard errors from each contribution summed in quadrature. A modified jackknife resampling scheme was also performed, in which instead of leaving out one site at a time, sites within 10 km of each other were grouped together and each of these proximity groups was left out incrementally before fitting OLR models to the remaining data. This spatial resampling analysis (Fig. A.7) did not result in significantly different parameter estimates than the full model presented in Fig. 1.3b. Estimates for the intercept terms C_1, C_2, and C_3 ($\pm$non-resampled standard errors) were found to be 0.72 ± 0.35, 1.41 ± 0.38, and 2.00 ± 0.42, respectively, indicating no significant difference between bleaching prevalence categories within our dataset. Using the statistical computing software R (Team, 2017, `https://www.r-project.org`), a random effect grouping variable was added to each of the highest-ranked models, which grouped reefs within 5 km of each other. These resulting mixed effects models were compared to their fixed effects equivalents to determine model fit improvement, and the inclusion of a random effect did not improve the fit of any of the 20 highest-ranked models (Appendix D). Furthermore, to account for possible nonlinear interactions between covariates, such as Depth $\times$ $\mathrm{DTR_{30}}$ or Acute1 $\times$ $\mathrm{DHW_{30}}$,

we also included a nonlinear interaction term to the highest-ranked model and determined model fit improvement. The AIC_C of these nonlinear models (Table A.1) indicated that the addition of a nonlinear interaction term did not significantly improve the fit of the original highest-ranked model displayed in Fig. 1.3b. Therefore, as our main result, we ultimately report the fixed effects ORL model parameter estimates with no nonlinear or interaction terms (Fig. 1.3b). The SST-based OLR analysis summarized in Fig. 1.5 was performed using the CoRTAD 4 km weekly SST data (Casey et al., 2015) pixels that were closest to our in situ bleaching observations. The quantities MMM, MMM_{Max} (Donner, 2011), Acute1, Acute2, DHW, $ROTC_{SS}$, and $ROTC_{90}$ (Table 1.1) were computed from the CoRTAD temperature data. This resulted in a total of 27 covariates (20 as described above, and 7 new ones computed from the CoRTAD data). We then proceeded to fit OLR models using all permutations of covariates, with the constraint that within each model, we only include $\leq$1 covariate from each category listed in Table 1.1. This produced 60,479 models, from which we performed model comparison using AIC_C, resulting in 12 dominant models being identified as statistically indistinguishable. From here, we concluded that when 4 km SST metrics are incorporated into our model framework, high-frequency temperature variability and depth remain the most influential covariates on bleaching prevalence, acting to attenuate bleaching (Fig. 1.5). Furthermore, acute and cumulative thermal stress exacerbate bleaching prevalence the most, and the SST-derived version of the latter contributes substantially to this effect. The results presented in Fig. 1.5 ultimately mirror those from Fig. 1.3b, c, indicating that DTR is the main driver of bleaching prevalence, regardless of whether SST or in situ quantities of the other predictors are used. Common covariates in these models were MMM, MMM_{Max}, MMM_{4km} , DHW_{30}, DHW_{4km} , Acute1, $Acute2_{4km}$, and $ROTC_{90-4km}$, and each of these 12 highes-tranked models included at least one SST-based covariate. The AIC_C values of these models ranged from 129.19 to 131.12, with McFadden's pseudo-R^2 values ranging from 0.35 to 0.38, which presents a considerable improvement to the highest-ranked model that was fit to only in situ values, which had an AIC_C equal to

143.75 and a McFadden's pseudo-R^2 of 0.30. To highlight the importance of High-Frequency Temperature Variability in model improvement, we also fit these models to the data and excluded the Daily Temperature Range covariate, which was either DTR_{30} or DTR_{90}. This significantly decreased model performance, with AIC_C values ranging from 153.46 to 169.57, and McFadden's pseudo-R^2 values ranging from 0.12 to 0.23, which supports the idea that DTR_{30} is the dominant driving variable for the bleaching response.

Chapter 2

Thermally-driven cross-shore exchange in steady alongshore currents

2.1 Introduction

Cross-shore circulation allows for the transport of heat, nutrients, and planktonic organisms to nearshore benthic ecosystems (Roughgarden et al., 1988; Nittrouer and Wright, 1994; Falkowski et al., 1998; Pringle, 2001; Brink, 2016). In the case of tropical coral reefs, which often have steep bathymetry over narrow shelves, cross-shore exchange can promote larval connectivity between reefs and adjacent ecosystems (Pineda et al., 2007; Cowen and Sponaugle, 2009), mitigate thermal stress by transporting heat (Molina et al., 2014; Herdman et al., 2015), and increase thermal resilience of corals through regular exposure to daily temperature variability (Davis et al., 2011; Safaie et al., 2018). While there are many mechanisms responsible for driving cross-shore fluxes, such as winds (Austin and Lentz, 2002; Lentz and

Fewings, 2012), internal tides and internal waves (Leichter et al., 1996; Reid et al., 2019), and surface waves (Lentz et al., 2008; Lowe et al., 2009), our interest here is with cross-shore transport due to atmosphere-ocean surface heat fluxes. Over nonuniform bathymetry (Figure 2.1), a feature common to coastal regions, surface heating and cooling induces greater volumetric heating in shallower water than deeper water, establishing a horizontal temperature gradient and a subsequent baroclinic pressure gradient that drives a vertically-sheared exchange circulation (Monismith et al., 1990, 2006). During periods of net surface heating, water flows offshore at the surface, with a compensating return flow at depth, and the pattern is reversed during net cooling. As atmospheric heating and cooling over nonuniform bathymetry induces the horizontal temperature gradient responsible for accelerating the baroclinic flow, we expect thermally-driven exchange to be a generic feature of nearshore regions. Hence investigating the role of surface heat fluxes in driving cross-shore transport improves our understanding of coastal circulation.

Previously, numerical and analytical studies have examined the thermally-driven exchange problem under various forcings. Farrow and Patterson (1993) considered coastal domains with relatively small slopes to derive an asymptotic solution for the nearshore temperature and flow response to a vertically-uniform, time-dependent surface heat flux, while Lei and Patterson (2006) explored results from a numerical model to show that the cross-shore exchange response is determined by the local depth, attenuation length of shortwave radiation, and amplitude of surface heat flux. Coenen et al. (view) present an analytical foundation for buoyancy-driven flow in a wedge under harmonic surface heat flux forcing to reveal that the leading-order temperature and flow response contains both a harmonic component and a steady residual component proportional to the Rayleigh number. Field evidence of convective motions driving thermal exchange has been found in a reservoir in Western Australia (Monismith et al., 1990) and on coral reefs in Eilat, Israel (Monismith et al., 2006, hereafter, M06) and Oahu, Hawaii (Molina et al., 2014, hereafter, M14). Data from these studies indicate the importance of the flow inertia in determining the phasing

of the momentum response in relation to the surface heat flux and temperature gradients. Furthermore, data from the Oahu and Eilat sites indicate different dynamic regimes based on thermal and cross-shore momentum balances. The Oahu data demonstrates an unsteady thermal/diffusive momentum regime, while the Eilat site exhibits both steady thermal and momentum regimes. Temporal variations in the diurnal thermally-driven cross-shore exchange flow in the Oahu observations were identified by Ulloa et al. (2018) to be due to wind stress, Coriolis, and time-varying eddy viscosity, the latter two via tidally-variable alongshore flow. Ulloa et al. (2018) developed an idealized linear model to demonstrate how tidally-driven flow can modulate a diurnal thermal exchange circulation over a fortnightly period, and that the alongshore flow influences the cross-shore momentum budget through Coriolis and bottom-driven vertical turbulent diffusion. While Ulloa et al. (2018) explored the effects of Coriolis and tidally-driven alongshore flow, their study was limited to a range of field-specific values. As such, we lack a wider understanding of the modulation of the thermal exchange by bottom-generated turbulence.

Using the Eilat data to scale the velocity shear by the convective velocity scale of buoyancy-driven flows, M06 demonstrated that stronger alongshore flows weaken the thermally-driven cross-shore exchange through enhanced turbulent mixing. However, the observations from M06 were limited to relatively quiescent alongshore flow conditions with $u_*/u_f < 1$, where

$$u_* = \sqrt{\frac{\tau}{\rho_0}} \tag{2.1}$$

is the friction velocity scale, and

$$u_f = \left(\frac{\alpha g I_0 D}{\rho_0 C_p}\right)^{\frac{1}{3}} \tag{2.2}$$

is a convective velocity scale. Here g is the acceleration of gravity, α is the thermal expansion coefficient, I_0 is the heat flux amplitude, D is the depth, ρ_0 is the reference density, C_p is the specific heat of sea water, and τ is the bottom shear stress. In this paper, we present an idealized numerical modeling investigation of the influence of a broad space of friction

velocity regimes on baroclinic thermally-driven cross-shore exchange. We begin with a base-case (buoyancy flux forcing only) thermally-driven exchange, and perturb this scenario by introducing alongshore currents of varying magnitudes, to characterize the resultant flows within the u_*/u_f parameter space.

2.2 Methodological Framework

2.2.1 Background

The alongshore and cross-shore momentum equations, respectively, are given by:

$$\frac{\partial u}{\partial t} + u\frac{\partial u}{\partial x} + v\frac{\partial u}{\partial y} + w\frac{\partial u}{\partial z} = -\frac{1}{\rho_0}\frac{\partial P}{\partial x} + \frac{\partial}{\partial z}\left(\nu_t \frac{\partial u}{\partial z}\right) + fv \tag{2.3}$$

and

$$\frac{\partial v}{\partial t} + u\frac{\partial v}{\partial x} + v\frac{\partial v}{\partial y} + w\frac{\partial v}{\partial z} = -\frac{1}{\rho_0}\frac{\partial P}{\partial y} + \frac{\partial}{\partial z}\left(\nu_t \frac{\partial v}{\partial z}\right) - fu \tag{2.4}$$

Here x, y, and z are the alongshore, cross-shore, and vertical coordinates, respectively, with corresponding velocity components u, v, and w, and t is time. P is the pressure, f is the (constant) Coriolis frequency, and ν_t is the eddy viscosity computed via a $k-\epsilon$ turbulence closure (details below). For our purposes, the vertical momentum equation reduces to a hydrostatic balance:

$$\frac{1}{\rho_0}\frac{\partial P}{\partial z} = -B \tag{2.5}$$

and the buoyancy equation is given by

$$\frac{\partial B}{\partial t} + u\frac{\partial B}{\partial x} + v\frac{\partial B}{\partial y} + w\frac{\partial B}{\partial z} = \frac{\partial}{\partial z}\left(\kappa_t \frac{\partial B}{\partial z}\right) + \frac{\partial F}{\partial z} \tag{2.6}$$

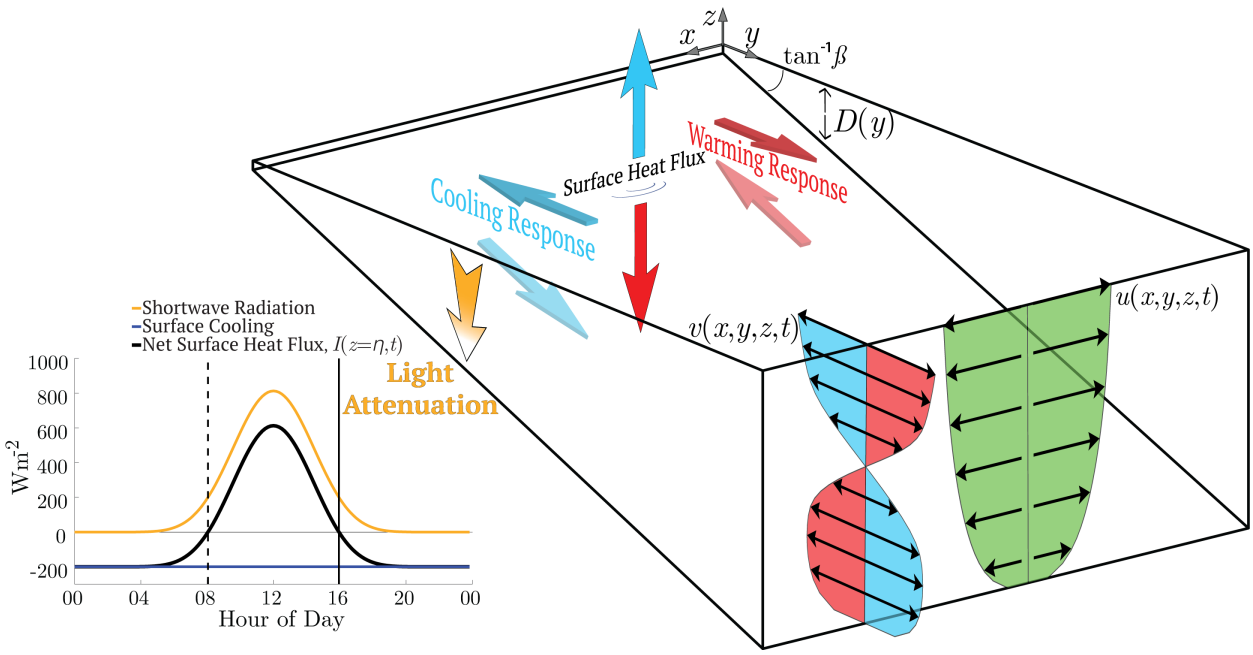

Figure 2.1: Schematic of the computational domain, with the diurnal periodic buoyancy forcing and circulation patterns associated with the cooling (blue arrows) and warming (red arrows) response flows. The buoyancy flux is composed of constant surface cooling and diurnally periodic shortwave radiation that penetrates below the surface and is attenuated with depth. The vertical lines in the surface heat flux plot indicated the transition from net surface cooling to net surface heating (dashed line) and net surface heating to net surface cooling (solid line), and will be shown in subsequent figures.

Buoyancy is related to temperature as $B = -\alpha g(T - T_0)$, with T, and T_0 being the water temperature and reference water temperature, respectively. The same $k - \epsilon$ turbulence closure is used to compute the eddy diffusivity, κ_t. Finally, F is the periodic buoyancy flux forcing, given by $F = -\frac{\alpha g I(z,t)}{\rho_0 C_p}$, where the laterally-uniform heat flux $I(z,t)$ is an idealized expression parameterizing heating and cooling due to depth-dependent irradiance and surface cooling, respectively (Figure 2.1). Given the alongshore-uniform domain used in our study, terms involving $\partial/\partial x$ in (2.3)-(2.6) are ignored, except for the alongshore pressure gradient associated with the alongshore current forcings (Table 2.1).

Following the analyses of M06 and M14, we can approximate the balances governing our problem by identifying the relevant dynamical limits. For both momentum and buoyancy, we expect diffusion to play an important role within the shallowest nearshore region of the

domain, where the depth is comparable to the length scale of the turbulent boundary layer. For larger slopes, advection will balance heating and cooling ($V\partial B/\partial y \sim \partial F/\partial z$), whereas farther offshore, the buoyancy budget will ultimately reach an unsteady limit in which the temperature response to the forcing is transient ($\partial B/\partial t \sim \partial F/\partial z$). From M14, the ratio $(\beta V T_f)/D$, where β is the slope, V is the cross-shore flow, and T_f is the period of forcing, provides a scaling of the advective to unsteady terms in both the momentum and buoyancy balances; at a given depth, for larger slopes, we anticipate advection to be important relative to the unsteady term, while farther offshore as the depth increases, the dynamical limits will approach an unsteady regime.

2.2.2 Model Configuration

We use the Regional Ocean Modeling System (ROMS) (Shchepetkin and McWilliams, 2005; Haidvogel et al., 2008), a terrain-following, free-surface model that solves finite differences of the Reynolds Averaged Navier Stokes equations using hydrostatic and Boussinesq approximations. The theoretical framework discussed in the present study is derived from Equations (2.3)-(2.6); however, the governing equations within ROMS (horizontal and vertical momentum, scalar transport, continuity, and equation of state) are expressed in flux form, in horizontal orthogonal curvilinear coordinates, and sigma vertical coordinates (Haidvogel et al., 2008).

The model grid is an alongshore uniform wedge, of 10 m lateral $(\Delta x, \Delta y)$ resolution, extending 1000 m in the alongshore and 5000 m in the cross-shore. For the baseline (hereafter, BL) simulation, no significant difference in results was observed among alongshore domains of 2 km, 1.5 km, and 1 km, and therefore we chose the shortest of these for computational efficiency. The grid has 30 vertical S-coordinate layers with stretching parameters $\theta_S = 3$, $\theta_B = 1$, and $h_C = 25$, chosen for greatest resolution at the surface and bottom. Horizontal

viscosity and diffusivity coefficients are set to dampen noise occurring on a time scale of 120 s, with a horizontal Prandtl number of 7 following Marques and Özgökmen (2014). The bottom slope and minimum depth are 3% and 1 m, respectively, resulting in a maximum domain depth of 151 m.

At the onshore and alongshore boundaries, all prognostic fields are set to closed and periodic boundary conditions, respectively. At the offshore boundary, the free surface and barotropic momentum boundary conditions are set to those of Chapman (1985) and Mason et al. (2010), respectively, to allow signals moving at the shallow water speed to radiate out normal to the boundary; the offshore 3D momentum and tracer (temperature and salinity) boundaries are set to the radiation condition of Orlanski (1976). Finally, the offshore mixing turbulent kinetic energy field has a gradient boundary condition. To attenuate numerical noise associated with open (offshore) boundary conditions, a sponge layer that linearly increases the horizontal viscosity and diffusivities by a factor of 10 is inserted in the offshore 500 m of the domain. The domain is initially quiescent, with uniform temperature and salinity fields of 24°C and 35 psu, respectively. All model runs have a baroclinic time step of 2 seconds, with 35 barotropic time steps in between each baroclinic time step, and are run for a 28 day simulation. Analysis is performed on the final 14 days of simulated output and all variables are averaged in the alongshore direction, from which a diurnal phase-averaged canonical day is computed. In general, runs reach quasi steady-state within the first $\sim$7 days of simulation time.

As the diurnal surface heat flux forcing includes both heating and cooling periods, using a hydrostatic model to simulate the ensuing convection requires a justification of our model choice. ROMS offers a number of parameterizations for the unresolved turbulent fluxes, and here we implement a modification of the two-equation $k - \epsilon$ (Rodi, 1987) version of the Generic Length Scale (Warner et al., 2005; Umlauf and Burchard, 2003) parameterization, in which the minimum turbulent kinetic energy value is 1E-12 $m^2 s^{-2}$. Simulations using

the $k - \epsilon$ turbulence closure have reliably reproduced convectively-driven flows, such as gravity currents and overflows (Ilıcak et al., 2008; Marques and Özgökmen, 2014), convective turbulence (Stips et al., 2002), wind deepening and penetrative convection of the mixed layer (Rodi, 1987), and shear driven turbulence (Jackson et al., 2008). Prognostic results of model simulations may be sensitive to the choice of turbulence closure, though here we restrict our attention to general features of the flows so that our conclusions should be robust. An investigation assessing the influence of turbulence parameterizations is beyond the scope of this paper, though warrants further inspection (Figure F.1). Ultimately, as our goal is to investigate the modulation of the thermal exchange in the presence of various forcing scenarios, the relative change in magnitude and spatio-temporal structure of the cross-shore exchange among forcing scenarios is the emphasis of this study.

In addition to the $k - \epsilon$ turbulence closure, the choice of advection algorithm for tracers in ROMS has been shown to influence its ability to replicate nonhydrostatic flows. Marques and Özgökmen (2014) simulated the lock-exchange problem using ROMS and a large eddy simulation model (taken as the ground truth), evaluating model performances using background potential energy (Winters et al., 1995). Importantly, they found the choice of tracer advection scheme influenced results such that the multidimensional positive-definite advection transport algorithm (MPDATA) more accurately represented the mixing and stratification compared to the ROMS default (fourth-order centered for both horizontal and vertical schemes) or other schemes. Hence, we will also use MPDATA for our simulations.

2.2.3 Model Runs

The thermal forcing common to all runs is an idealized analytical expression representing surface heat fluxes for a periodic diurnal cycle of heating and cooling, with periods and amplitudes of both phases informed by meteorological observations (i.e. M06 and M14). At

the surface, the time-dependent heat flux is given by:

$$I(z=\eta,t) = I_0 sin^{10}\left(\frac{2\pi t}{T_f}\right) - 200 \tag{2.7}$$

while below the surface, the depth-dependence of the parameterized shortwave radiation is given by the double exponential decay function of Paulson and Simpson (1977):

$$I(z\neq\eta,t) = \left[I_0 sin^{10}\left(\frac{2\pi t}{T_f}\right)\right]\left(Re^{z/\zeta_1} + (1-R)e^{z/\zeta_2}\right) \tag{2.8}$$

Here I_0 is the magnitude of incoming solar radiation, T_f is the period of diurnal forcing (equal to 1 day), and R, ζ_1, and ζ_2 are fitting parameters associated with optically clear water, categorized as Jerlov water type 1 (Jerlov, 1976). It is important to recognize that Eqs. (2.7) and (2.8) effectively distribute incoming heating vertically but remove heat only at the surface.

The baseline scenario, BL, is forced only by the diurnally periodic surface heat flux forcing described by (2.7) and (2.8). Additional simulations were forced with the same surface heat flux as that in BL, as well as with steady alongshore currents of varying magnitudes (Table 2.1). Within ROMS, the steady alongshore forcing was implemented by applying an alongshore-directed kinematic momentum flux with a magnitude scaled by the local depth; this is equivalent to a constant alongshore pressure gradient. The kinematic momentum flux was then applied as a bodyforce throughout the water column by activating the ROMS "BODYFORCE" C-preprocessor directive to distribute the stress vertically. At a depth of 20 m, this alongshore forcing is equivalent to an alongshore pressure gradient ranging from 9.9E-6 m s^{-2} for the weakest alongshore forcing to 9.0E-4 m s^{-2} for the strongest alongshore forcing. Simulations are distinguished by the ratio of u_*/u_f at the 20 m isobath in Table 2.1, where the value of u_* is computed within the model using a logarithmic drag formulation with an integration constant (i.e. "z_0") set to 2 cm.

Forcing	**Name**	τ_x^b [Pa]	u_*/u_f
Diurnal Buoyancy Flux only	BL	N/A	N/A
Diurnal Buoyancy Flux and	U1	0.0094	0.17
Steady Upwelling-Favorable	U2	0.018	0.25
Alongshore Current	U3	0.058	0.44
	U4	0.29	0.98
	U5	0.40	1.2
	U6	0.90	1.7
Diurnal Buoyancy Flux and	D1	-0.0097	0.18
Steady Downwelling-Favorable	D2	-0.02	0.26
Alongshore Current	D3	-0.065	0.46
	D4	-0.31	1.0
	D5	-0.42	1.2
	D6	-0.93	1.8
Steady Upwelling-Favorable	NU1	0.0092	N/A
Alongshore Current, no	NU2	0.019	N/A
Buoyancy Flux	NU3	0.058	N/A
	NU4	0.29	N/A
	NU5	0.40	N/A
	NU6	0.90	N/A
Steady Downwelling-Favorable	ND1	-0.012	N/A
Alongshore Current, no	ND2	-0.023	N/A
Buoyancy Flux	ND3	-0.065	N/A
	ND4	-0.31	N/A
	ND5	-0.42	N/A
	ND6	-0.93	N/A

Table 2.1: Name and forcing of each ROMS simulation, with the alongshore bottom stress and ratio of friction to convection velocity scales at the 20 m isobath. No value of τ_x^b is listed for the base-case simulation (BL), as that simulation was not forced with an alongshore current. Convective velocity scales are not applicable for scenarios with no diurnal buoyancy flux forcing.

A final group of simulations was run with the same range of alongshore forcing, but with zero buoyancy flux to isolate cross-shore exchange driven solely by the Coriolis contribution to the cross-shore momentum budget. These simulations achieved equilibrium flow more quickly than the simulations with diurnal heating and cooling, so were run for only 10 days, and are identified with the prefix "N" in Table 2.1.

2.2.4 Diagnostic Quantities

Following M14, we quantify the cross-shore volume exchange associated with the baroclinic flow as:

$$\Gamma(y,t) = \frac{1}{2}\int_{-h}^{\eta} |v(y,z,t) - \overline{v}(y,t)| dz \tag{2.9}$$

and heat transport as:

$$Q_{ex}(y,t) = \rho_0 C_p \int_{-h}^{\eta} \big[v(y,z,t) - \overline{v}(y,t)\big]\big[T_{anom}(y,z,t)\big] dz \tag{2.10}$$

Here, the overbar represents depth-averaging, and T_{anom} is a measure of the depth- and diurnally-variable temperature associated with the baroclinic pressure gradient, and is computed by subtracting the low-frequency volume-averaged temperature from the raw output temperature.

2.3 Results

2.3.1 Thermally-Driven Cross-Shore Circulation

To illustrate the time-evolution of the temperature and cross-shore velocity in response to the various forcings, snapshots showing T_{anom} and stream function contour lines are presented

at various instances through the diurnal cycle for a subset of simulations in Figure 2.2. To obtain a characteristic magnitude of each term in the cross-shore momentum balance, the depth-average of the absolute value of the baroclinic terms in the cross-shore momentum budget were computed from the ROMS model diagnostics. For additional suppression of numerical noise, our model setup includes sub-grid scale horizontal mixing of momentum using the Laplacian operator, labeled in the cross-shore momentum budget below as "y-Diffusion", and will be ignored in the present dynamical analysis. This term is expected to be nontrivial only during the propagation of transient events characterized by large cross-shore velocity gradients, during which it will at most be of similar magnitude as the turbulent diffusion term. For BL, these results are presented in the $y-t$ plane in Figure 2.3. Then, for BL as well as for U1, U3, U5, D1, D3, and D5, time-averages of the depth-averaged absolute values of the baroclinic components of the cross-shore momentum balance during the cooling response flow (08:00-12:00) and warming response flow (14:00-20:00) are shown as a function of cross-shore distance (Figure 2.4).

Circulation in BL is characterized by two distinct phases: a cooling response period occurring approximately from t = 20:00-12:00, consisting of convective cooling and downslope flow, and a warming response period from t = 14:00-20:00 (Figure 2.2). From the late evening through the early morning (Figure 2.2a-b, BL) convective cooling mixes the water column and decelerates the warming response flow from the previous day, resulting in cross-shore velocities that are quite small. As cooling progresses, the temperature within the shallower nearshore regions decreases more rapidly than in adjacent regions offshore, consequently forming an offshore (positive) cross-shore temperature gradient. The dominant baroclinic cross-shore momentum balance corresponding to the cooling, and warming, response flows is between the pressure gradient and turbulent diffusion terms (Figure 2.3f, g). The development of convective cooling during this time is reflected in the turbulent diffusion term (Figure 2.3g), which increases in magnitude and cross-shore extent, while the growing cross-shore temperature gradient yields an enhancement of the baroclinic cross-shore pressure gradient

(Figure 2.3f).

From 06:00 to 09:00 (Figure 2.2c-d, BL), the cross-shore temperature gradient strengthens with the coldest temperatures nearshore (Figure 2.3h), and a growing counterclockwise circulation pattern that extends through the nearshore 1 km, though with relatively weak velocities consistent with strong vertical turbulent diffusion. The cooling response flow is most evident beginning from approximately 8:00, with the onset of net surface heating and waning convective turbulent diffusion (Figure 2.3g). The cold dense water that has formed in the nearshore accelerates downslope in the form of a gravity current, with an overlying compensating return flow. This downslope flow persists well after the surface forcing has changed signs, and is ultimately reversed by the warming response flow. However, the pressure gradient term (Figure 2.3h) continues to expand and increase due to the slumping of the isotherms, as the cross-shore thermal gradient is distributed horizontally with the propagating downslope flow. Noticeable increases in the cross-shore and vertical advection terms (Figure 2.3c, d) capture the transient propagation of this cooling response flow, serving to balance the pressure gradient. Cross-shore velocities during the cooling response flow reach up to (+)1.7 and (-)2.3 cm s^{-1} in the bottom and surface, respectively. The cooling response flow magnitude reaches its maximum shortly before 12:00, and with the advent of the stratification induced by surface heating, the flow decelerates and begins to reverse (Figure 2.2e, BL). Owing to developing stable stratification and the deceleration and reversal of the cross-shore flow, the components of the cross-shore momentum budget are briefly arrested within a time period near t = 12:00.

Surface heating establishes a nearshore warm region (Figure 2.3h), and by 15:00, the warmest waters are found at the surface and in the nearshore tip of the wedge (Figure 2.2f, BL). This cross-shore temperature gradient gives rise to a new baroclinic pressure gradient, which is again predominantly balanced by turbulent diffusion (Figure 2.3f,g), now associated with convection due to bottom heating close to shore. While the cooling response circulation

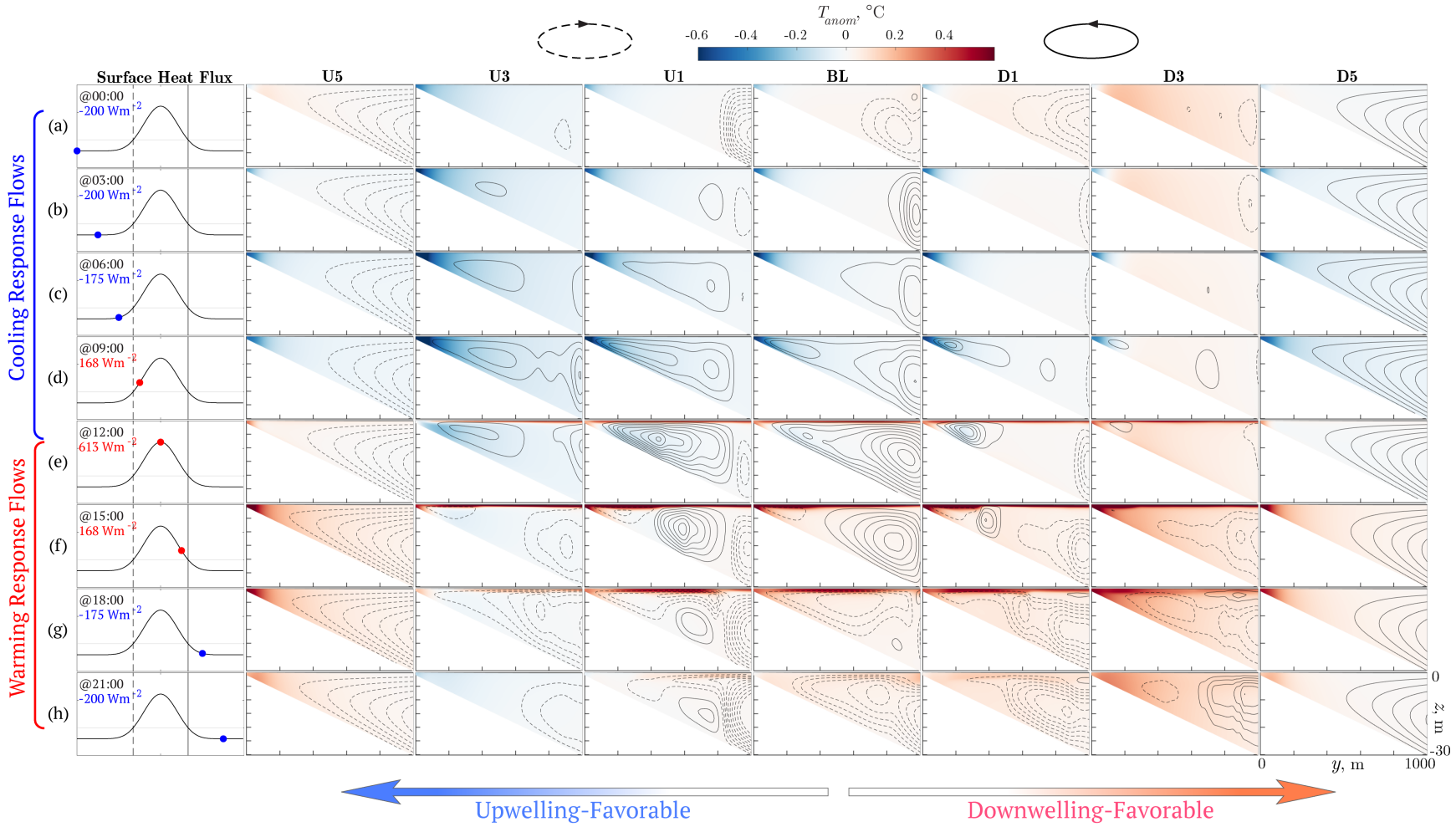

Figure 2.2: Snapshots at 3 hour intervals of T_{anom} and streamfunction contours, with an interval of 0.01 m^2s^{-1}, for BL, U1, U3, U5, D1, D3, and D5. At each time, the phase of the surface heat flux is shown on the left.

is still present offshore of ∼500 m, a convective current in the form of a warm front emanates from the nearshore region of the wedge and propagates offshore at the surface. This is most evident in the increased unsteady acceleration within the nearshore 600 m, from t = 12:00 to t = 18:00 (Figure 2.3a). This warm front drives the lagged warming response flow, seen as clockwise flow with maximum cross-shore velocities of 2.7 cm s^{-1} at the surface, persisting through t = 21:00 (Figure 2.2g-h, BL), even as the surface forcing changes signs again, indicative of an unsteady momentum response. The offshore-propagating increase in turbulence diffusion beginning at $t \approx$ 18:00 indicates convection associated with surface cooling (Figure 2.3g), which serves to weaken the stratification in the nearshore. Immediately afterwards, turbulent diffusion is briefly reduced, as velocity gradients are no longer present during this time. Convective cooling continues to reverse the nearshore thermal gradient overnight, and the diurnal cycle is renewed.

2.3.2 Modification of Thermally Driven Cross-Shore Circulation by Alongshore Flow

Simulations with the same buoyancy flux forcing as that of BL, but additionally forced with varying amplitudes of upwelling- and downwelling-favorable alongshore flow are also shown in Figure 2.2. For all scenarios, thermal stratification is first introduced via the surface forcing, and then redistributed through the domain due to the combined effects of thermal exchange and steady upwelling- and downwelling-favorable alongshore currents. Here we focus on scenarios U1, U3, U5, D1, D3, and D5 (Table 1), as they span a sufficient dynamic range of u_*/u_f from 0.17 to 1.2, for comparison to BL. From 00:00 to 09:00, all scenarios show a generally positive cross-shore temperature gradient, with the coldest water onshore of approximately y = 200 m, and an unstratified near-surface region (Figure 2.2a-d). During this time period, the upwelling-favorable simulations retain colder water throughout the interior 1 km than do the downwelling-favorable simulations. U5 and D5 constitute

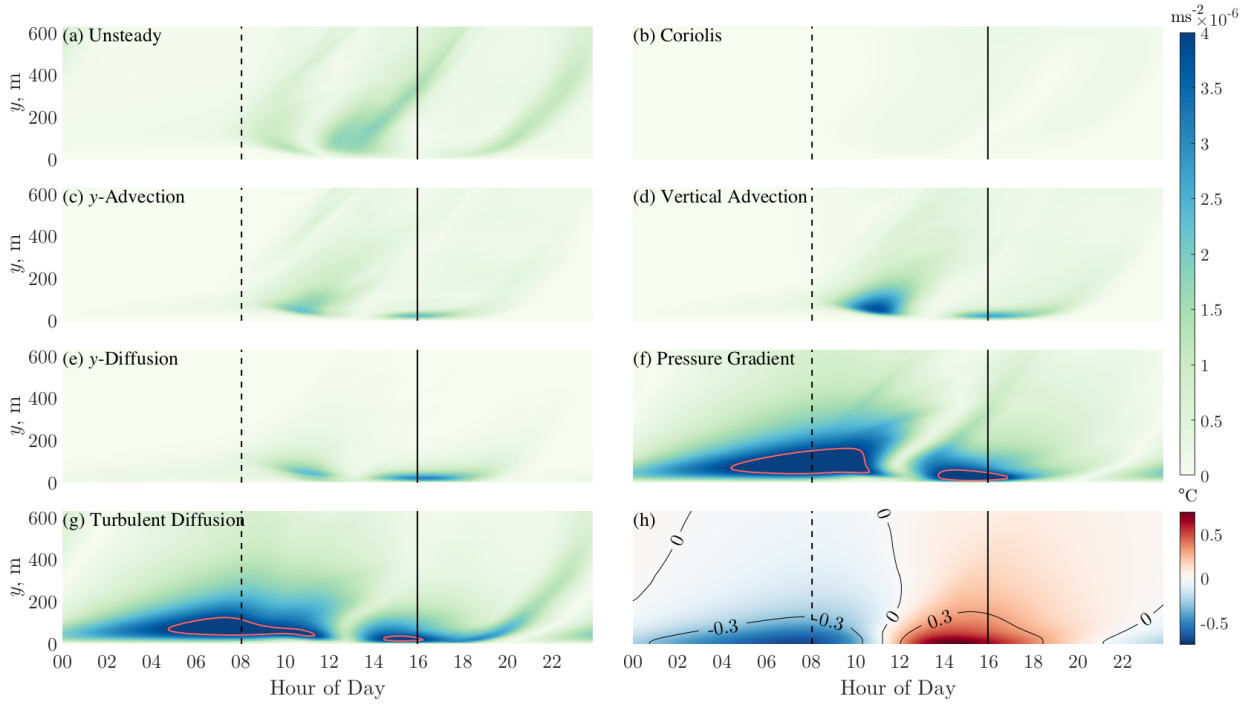

Figure 2.3: (a)-(g) Depth-averaged absolute values of the baroclinic cross-shore momentum terms for BL, with the 4E-6 ms^{-2} contour highlighted; (h) depth-averaged T_{anom} for BL.

exceptions to this, as both simulations show milder temperature gradients during this time (Figure 2.2a-d, U5 and D5). By t = 12:00, net surface heating results in a warm, stratified near-surface for all runs except U5 and D5, (Figure 2.2e), and by t = 15:00, the cross-shore temperature gradient for all runs is generally negative (Figure 2.2f). By t = 21:00, net surface cooling serves to erase the warm surface layers that were present, and the cross-shore temperature gradients for all runs begins to diminish and reverse.

Simulations with $u_*/u_f < 1$, namely U1, U3, D1, and D3 in Figure 2.2, show diurnal patterns of cross-shore circulation that are generally similar to the thermally-driven circulation pattern seen in BL, with differences in amplitude, spatial structure, and temporal phasing. For upwelling-favorable alongshore flow, during the late evening and early morning, convective cooling diminishes stratification and decelerates the warming phase flow from the previous day (Figure 2.2 U1 and U3, a-b), as in BL. As nearshore cooling establishes a sufficient cross-shore temperature gradient and drives the cooling response circulation, the

characteristic counterclockwise flow pattern emerges for U1 and U3 in the nearshore 1 km within 06:00$\leq t \leq$12:00 (Figure 2.2c-d, U1 and U3). During this time, the baroclinic pressure gradient in the cross-shore momentum budget for both U1 and U3 is larger than it is in BL within the nearshore 1 km (Figure 2.4b, c). For U3 however, the turbulent diffusion and Coriolis contributions are increased due to the stronger alongshore flow, and in the nearshore 200 m, the advection terms for U3 are smaller than those for U1 or BL. The maximum surface (onshore) and bottom (offshore) cross-shore velocities for U1 during the cooling response are 2.0 cm s^{-1} and 2.8 cm s^{-1}, respectively, which are stronger than those for BL during this time, while for U3, the cooling response cross-shore circulation is weaker than that for both BL and U1. As surface heating erases and reverses the morning cross-shore temperature gradient during 12:00$< t <$15:00, the cross-shore circulation is also decelerated and reversed for U1 and U3, though for U1, the counterclockwise cooling response circulation persists between 400 and 800 m (Figure 2.2f, U1). By 18:00, the warming response circulation pattern fully occupies the nearshore 1 km for U3 (Figure 2.2g, U3), while for U1, this clockwise circulation overlies the residual cooling response circulation near $y = 600$ m (Figure 2.2g, U1), and merges with an offshore clockwise circulation cell produced as a result of divergence during the earlier cooling response flow. During the warming response, the baroclinic cross-shore momentum balances for both U1 and U3 show strong dependence on cross-shore distance; inshore of $y = 200$ m, the balances are dominated by the turbulent diffusion and pressure gradient terms, with advection playing a secondary role (Figure 2.4i, j). For U1, the balance resembles that of BL, with a slightly greater Coriolis contribution, while for U3, the Coriolis term is of leading order offshore of $y \approx 300$ m. Net surface cooling has resumed by $t =$ 16:00, and by 21:00, convective cooling for both U1 and U3 reverses the nearshore temperature gradient and decelerates the warming response circulation (Figure 2.2h, U1 and U3). Cross-shore velocities in the nearshore 500 m for both U1 and U3 are reduced to $O(0.1)$ cm s^{-1}, and the early morning convective cooling period returns.

Steady, downwelling-favorable alongshore currents with $u_*/u_f < 1$ (D1 and D3) main-

tain a diurnally-modulated cross-shore thermal exchange structure similar to that of BL, though with generally weaker cross-shore circulation. During the early morning hours (00:00< t <06:00), surface cooling establishes a positive cross-shore temperature gradient, and the residual warming response circulation from the previous evening is decelerated for D1 (Figure 2.2a-c, D1), as well as for the much weaker flows in D3 (Figure 2.2a-c, D3). From 09:00 to 12:00, nearshore cold and dense water accelerates downslope, driving the cooling response for D1 and D3 (Figure 2.2d-e, D1 and D3), although the cross-shore circulation in D3 is rather weak. Compared to that of BL, the cooling response cross-shore circulation in D1 occupies a narrower nearshore region, yet drives stronger cross-shore velocities, which reach 3.6 cm s^{-1} and 2.0 cm s^{-1} at the surface (onshore) and bottom (offshore), respectively. Within the baroclinic cross-shore momentum budget during the cooling response flow, the pressure gradient for D1 reaches larger values than in BL inshore of $y \approx 300$ m (Figure 2.4e). For D3, the baroclinic pressure gradient, which is smaller than that of BL, is generally balanced by turbulent diffusion inshore of $y \approx 300$ m, beyond which the Coriolis contribution dominates the cross-shore momentum budget (Figure 2.4f). Net surface heating begins by 08:00, and by 15:00, the nearshore clockwise warming response circulation is evident in D1 and D3 (Figure 2.2f, D1 and D3). For both scenarios, the clockwise cross-shore circulation fills the nearshore 1 km by 18:00, though the strongest circulation can be seen offshore of y = 400 m (Figure 2.2g, D1 and D3). In the late afternoon, net surface heating has established a warm surface layer and a negative cross-shore temperature gradient, which, although surface cooling has resumed by 16:00, persist until approximately 21:00 (Figure 2.2h, D1 and D3). The warming response baroclinic cross-shore momentum budget for D1 is similar to that of BL, with a strong pressure gradient and turbulent diffusion balance, and advection playing a secondary role, inshore of $y = 200$ m (Figure 2.4l). Offshore of $y \approx 200$ m, the relative importance of advection increases while the pressure gradient and turbulent diffusion contributions are consistently important. For D3, a similar balance holds inshore of $y \approx 200$ m as in D1, though with an increase in the pressure gradient and decrease in the

advection terms (Figure 2.4m). For D3 offshore of $y \approx 200$ m, increases in the Coriolis and turbulent diffusion terms reflect the increased alongshore flow. For D1 and D3, after $t \approx$ 21:00, the warm surface layer dissipates and the cross-shore temperature gradient reverses; the clockwise warming response circulation is still present (Figure 2.2h, D1 and D3), though this circulation is weakened in the most nearshore region of the domain. The progression of net surface cooling and the associated convection gradually decelerates these flows overnight, and the diurnal cycle begins again.

Simulations with stronger alongshore forcing (U5 and D5), with $u_*/u_f > 1$, exhibit primarily Coriolis-driven circulation in the cross-shore, only slightly modified diurnally by thermally-driven exchange. The strong upwelling-favorable alongshore flow scenario, U5, has a persistent clockwise-oriented (offshore surface flow and onshore bottom flow) circulation throughout the day (Figure 2.2a-h, U5), while D5 exhibits similarly consistent cross-shore flow (Figure 2.2a-h, D5), but with a counterclockwise circulation. The steady clockwise cross-shore circulation in U5 is stronger during the warming response flows (Figure 2.2e-g, U5) than during the cooling response flows (Figure 2.2b-d, U5), as evidenced by the locations of the streamfunction contours. The opposite is apparent for D5, whereby the steady counterclockwise circulation is stronger during the cooling response flows than during the warming response flows. This diurnal modulation is attributed to the thermally-driven exchange, which is of secondary importance in driving vertically-sheared cross-shore flow for $u_*/u_f > 1$. For U5 and D5, the dominance of the Coriolis, turbulent diffusion, and pressure gradient terms (Figure 2.4a,h,g,n) in the cross-shore momentum budget are indicative of a balance between Coriolis, vertical mixing due to the strong alongshore flow, and lateral temperature gradient, while the advection terms are negligible. During the cooling response, the positive nearshore temperature gradient for both U5 and D5 peaks near $y = 100$ m (Figure 2.2b-d, U5 and D5), and the baroclinic pressure gradient contribution to the cross-shore momentum budget is smaller than that of BL (Figure 2.4a, g). Due to the diurnal modulation from the thermal exchange mentioned above, turbulent diffusion is larger, asso-

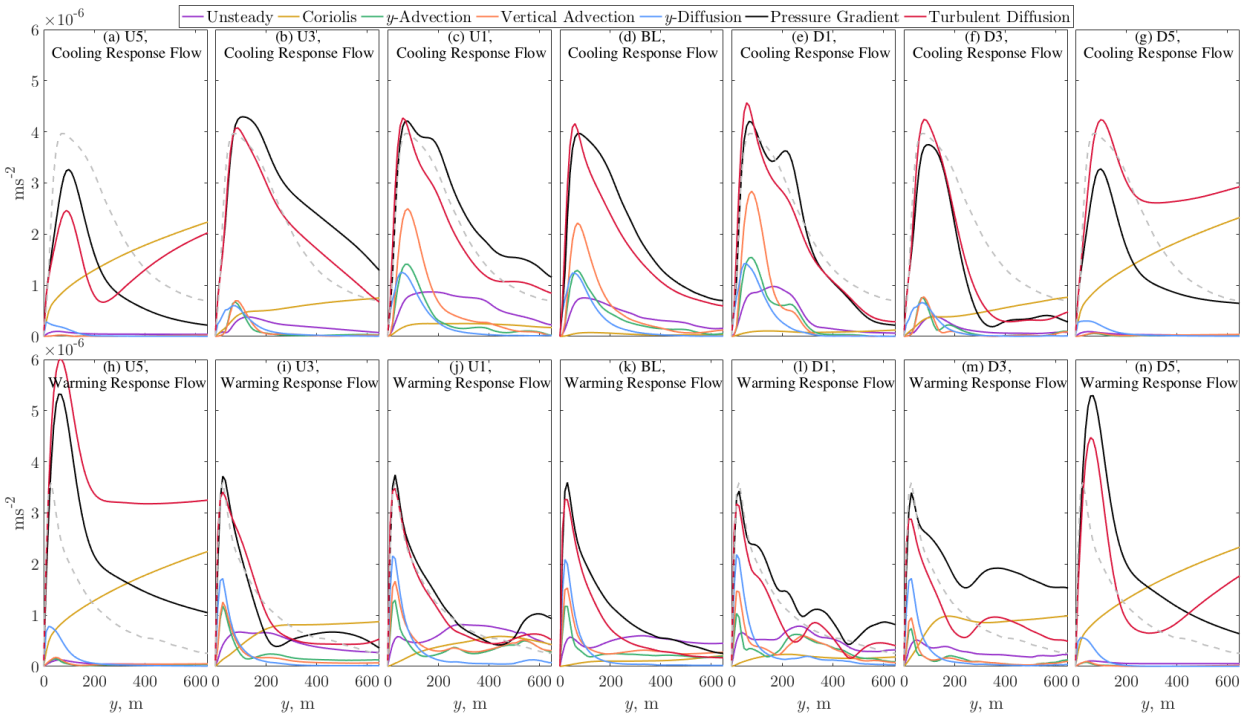

Figure 2.4: Depth-average absolute values of the terms in the baroclinic cross-shore momentum budget for the indicated ROMS simulations, time-averaged during the cooling response flows, 08:00-12:00 (a-g), and during the warming response flows, 14:00-20:00 (h-n). For comparison, the depth-average of the absolute value of the baroclinic pressure gradient for BL from the corresponding time-average is reproduced as a dashed grey line in the panels for U1, U3, U5, D1, D3, and D5.

ciated with greater alongshore bottom stress, for D5 than for U5 during this time. During the warming response for U5 and D5, the negative cross-shore temperature gradient (Figure 2.2f, g, U5 and D5) and hence the baroclinic pressure gradient (Figure 2.4h, n), also peak near $y = 100$. Additionally, the enhanced Coriolis acceleration for U5 and D5 contributes to a greater baroclinic pressure gradient for these simulations compared to BL. The warming response diurnal modulation from the thermal exchange implies that turbulent diffusion associated with bottom stress is larger for U5 than for D5.

It is evident from the patterns in the cross shore momentum terms in Figure 2.3 that the diurnal variation in the thermally-driven baroclinic momentum response for BL is constrained within a limited nearshore region. To estimate a cross-shore length scale for this region, we first note that, for the cooling phase, we can expect that convection will vertically homogenize

the temperature close to shore. Here the temperature will be inversely proportional to the depth, and a diffusive dynamic regime will apply following M06 and M14, with a velocity that scales as $v \sim \beta u_f^2 T_f / D$. The cross-shore extent of this region, L_y, in turn will scale as vT_f. The slope β relates the depth at this location to the distance from shore, and we obtain the following scaling relation:

$$L_y \sim \left(\frac{\alpha g I_0 \beta}{\rho_0 C_p} \right)^{1/2} T_f^{3/2} \tag{2.11}$$

Using the BL model parameters (α = 1.7 x 10^{-4} C^{-1}, β = 0.03, T_f = 86400 s, I_0 = 613 Wm^{-2}, ρ_0 = 1027 kgm^{-3}, C_p = 3985 $Jkg^{-1}C^{-1}$) yields $L_y \sim 1$ km. The actual scale for BL (Figures 2.2, 2.3) is smaller than this, but the balance noted in (2.11) provides a guide for how we can expect L_y to vary as forcing and geometry change. As convective cooling terminates and the surface buoyancy flux forcing changes signs, advection of cross-shore momentum then becomes important. The velocity scale for advection, V_{AD}, is proportional to the cross-shore extent of the viscous region, and we can define a draining time as $t_{AD} \sim L_y / V_{AD}$.

For the stabilizing heating phase, the cross-shore extent of the thermal response is determined by the depth of radiative heat penetration, given by the optical depth used in Equation (2.8). For Jerlov type I waters, the e-folding depth of 3 m corresponds to ≈100 m offshore; more than 50% of the incident solar radiation is absorbed by the surface 1 m of the water column, and over 80% is absorbed within 20 m depth. Therefore, the appropriate velocity scale for the buoyant surface current resulting from the absorption of irradiance in the water column is given by $u_f(D)$, with $D \sim O(10)$ m.

2.3.3 Advective Exchange

The consequence of vertically-sheared cross-shore flow within a thermally-stratified water column is the cross-shore exchange of water and heat. To quantify this exchange, we examine the baroclinic advective volume exchange (Γ) and heat exchange (Q_{ex}) for each simulation. In

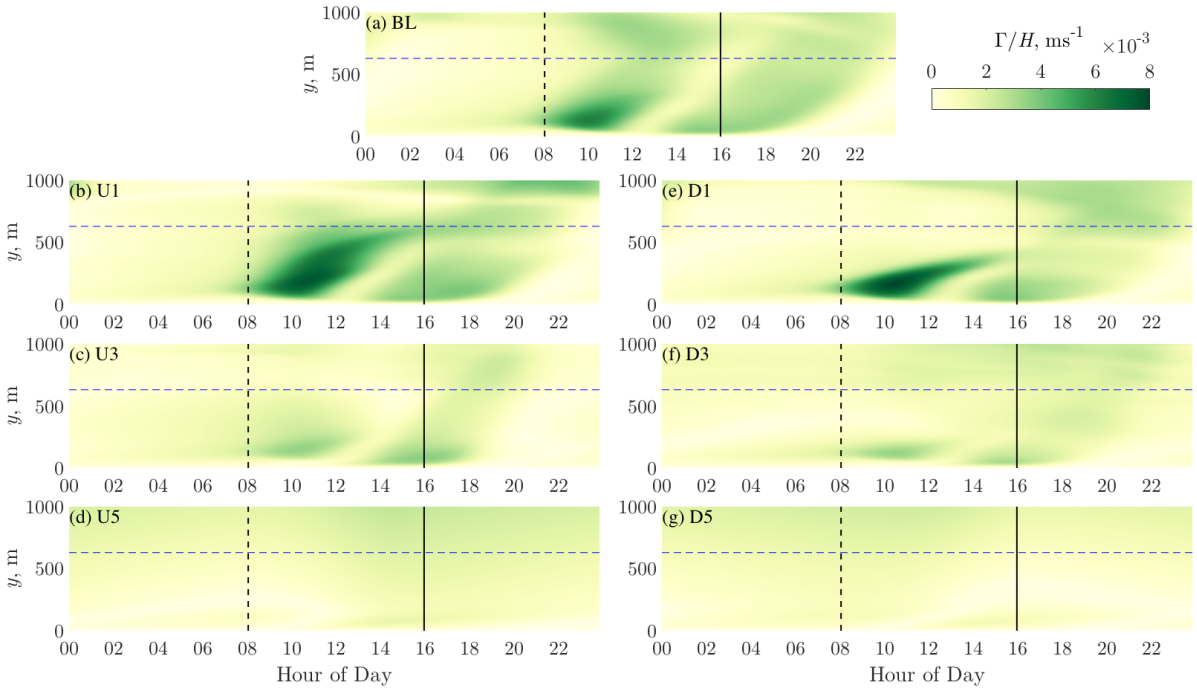

Figure 2.5: Exchange rate, or Γ/H, in the $y-t$ plane for the noted simulations. The y location of the 20 m isobath is indicated by the horizontal dashed line spanning each panel.

the analysis below, Γ is normalized by the local depth to arrive at a characteristic "exchange rate", which can be interpreted as a measure of the baroclinic cross-shore velocity magnitude. Note that Γ is associated with advection within the cross-shore momentum budget.

The diurnal phase-averaged exchange rate (Γ/H), shown in Figure 2.5, exhibits a diurnal pattern corresponding to periods of cross-shore momentum advection. For BL (Figure 2.5a), the downslope gravity current ($\approx$ 08:00 to 11:30) and the offshore-propagating warm front ($\approx$ 13:00 to 19:00) constitute the notable periods of strong exchange. In the late evening and early morning, the exchange rate diminishes considerably as vertical mixing associated with convective cooling limits acceleration and thus minimizes baroclinic cross-shore flow. The exchange rate for BL peaks at $y = 130$ m and $t = 10{:}00$, corresponding to the downslope flow during the cooling response. For U1, the mildest upwelling-favorable alongshore flow scenario, (Figure 2.5b), the exchange rate exhibits a similar diurnal pattern as in BL; however, the peak exchange rate for U1 is 24% greater, and occurs farther offshore

(at $y = 200$ m) and later (at t =10:50) than in BL. For increased steady upwelling-favorable alongshore flow (U3, Figure 2.5c), the peak in the exchange rate is 40% smaller than that of BL, and coincides with the warm front ($y = 80$ m at $t = 16{:}00$) rather than the cooling response downslope flow. For $u_*/u_f > 1$ (U5), the peak in exchange rate within the nearshore 200 m is reduced by 76% compared to that of BL, though a diurnal pattern is still evident (Figure 2.5d). As for U1, the exchange rate for the mildest downwelling scenario, D1, retains a similar diurnal pattern as in BL, occurring during the cooling-response flow at $y = 170$ m and $t = 10{:}30$, though importantly, the peak is 30% and 5% larger than those of BL and U1, respectively (Figure 2.5e). The strength of the alongshore forcing increases for D3, while the peak exchange rate diminishes by 45% and 7% compared to those of BL and U3, respectively, occurring at $y = 120$ m and $t = 10{:}30$ (Figure 2.5f). For the strongest downwelling-favorable alongshore forcing, in which $u_*/u_f > 1$ (D5), the peak in the exchange rate within the nearshore 200 m is 82% and 12% smaller than those of BL and U5, respectively (Figure 2.5g). Note that for $u_*/u_f > 1$, the cross-shore exchange rate is primarily an expression of the upwelling- (Figure 2.5d) and downwelling-favorable (Figure 2.5g) Coriolis-driven circulation, and the effect of the diurnal surface forcing is to enhance the upwelling-favorable circulation during the warming response (Figure 2.5d), or enhance the downwelling-favorable circulation during the cooling response (Figure 2.5f).

2.3.4 Dynamics of Cross-Shore Volume Exchange

Here we seek to establish a paradigm relating the strength of the alongshore forcing to the cross-shore exchange rate (Figures 2.5 and 2.6), with an emphasis on explaining the observed variations in exchange rate relative to BL. The thermally-driven exchange in the cross-shore results from two dominant advective phenomena: a downslope flow during the cooling response, and an offshore-directed surface warm front during the heating response. The thermally-driven baroclinic cross-shore momentum balance is relevant over a length

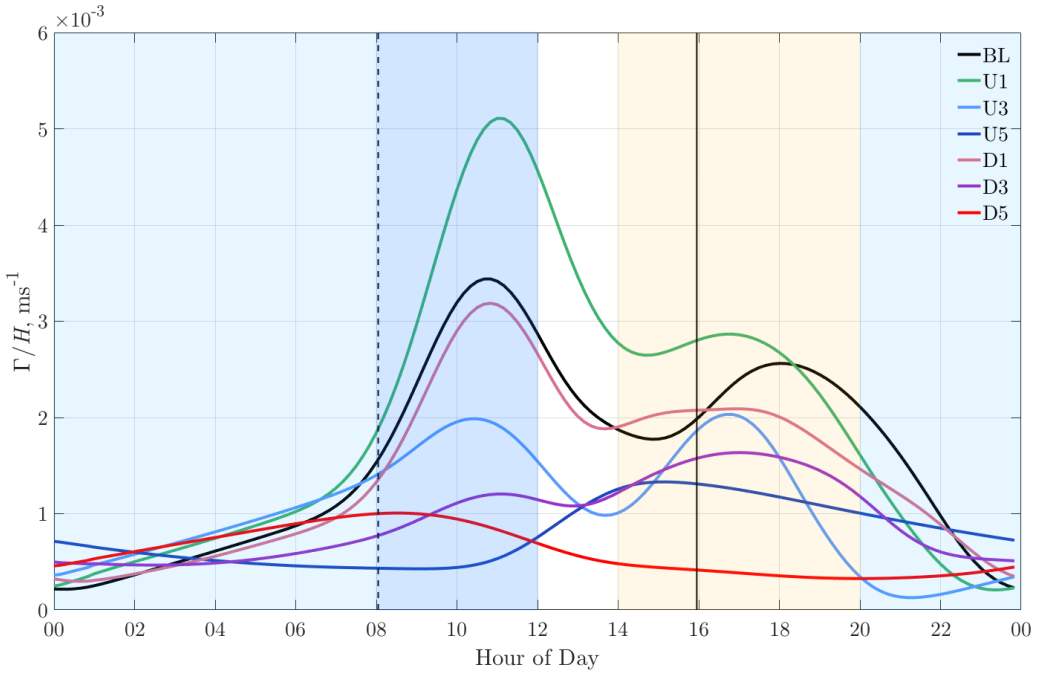

Figure 2.6: Diurnal time-series of exchange rate, or Γ/H, for the noted simulations, cross-shore averaged to the 20 m isobath. The shaded regions indicate the periods of convective cooling (20:00-08:00), and cooling response (08:00-12:00) and warming response (14:00-20:00) flows.

scale given by Eqn. (2.11), and when considering the cross-shore extent of dominant Γ/H presented in Figure (2.5), it is apparent that the location of the 20 m isobath ($y = 630$ m) provides a cross-shore reference scale that reasonably captures the extent of both the cooling and heating response flows. Figure (2.6) shows the phase-averaged diurnal time series of Γ/H, cross-shore averaged to the 20 m isobath, allowing for a direct comparison between the magnitudes of the cooling and heating response exchange flows among simulations.

Upwelling- and downwelling-favorable flow components for $u_*/u_f < 1$ lead to perturbations in the baroclinic structure relative to that of BL which modify the cross-shore exchange. From the instantaneous snapshots in Figure 2.2a-d, it is evident that the magnitude of the cooling phase cross-shore thermal gradient for BL increases towards shore. This is further reflected in the baroclinic gradients shown in Figures 2.3 and 2.4d. For the upwelling-favorable scenarios, the Coriolis component imports cold water to the nearshore, further strengthen-

ing this gradient and expanding its cross-shore extent (Figure 2.4b, c). This, in turn, drives stronger acceleration during the cooling response, resulting in an intensified downslope flow and therefore increased Γ (Figure 2.5).

For mild downwelling-favorable alongshore flow (D1), the Coriolis contribution slightly increases the magnitude of the cross-shore thermal gradient, but also compresses this region closer to shore. The resulting exchange is therefore slightly increased compared to BL, but only in this narrower nearshore region. As the upwelling- and downwelling-favorable alongshore flow magnitude increases, the Coriolis contribution to the thermal structure begins to dominate relative to the thermally-driven circulation, thus weakening the resulting cross-shore exchange.

The advective heat transport, Q_{ex}, (Figure 2.7) exhibits similar patterns to the volume exchange, such that the heat transport in BL (Figure 2.7a) maintains the characteristic diurnal pattern associated with the cooling and warming response flows. For BL, the downslope flow during the cooling response transports cold water offshore, reaching a peak advective cross-shore heat transport of $(-)4.49 \times 10^4$ Wm^{-1} at $y = 640$ m and $t =$ 13:00, serving to heat the nearshore. The warm front transports heat offshore, cooling the nearshore, and reaching a peak of 6.64×10^4 Wm^{-1} at $y = 510$ m and $t =$ 17:10. U1 shows stronger cross-shore advective heat transport than that of BL, consistent with the pattern for Γ, with peaks during the cooling and warming responses increasing by 49% and 21%, respectively (Figure 2.7b). As the alongshore forcing increases, the peak cooling and warming response heat transport for U3 compared to BL are reduced by 44% and 23%, respectively (Figure 2.7c), and occur closer to shore. For U5, in which $u_*/u_f > 1$, the advective heat transport is generally an order of magnitude smaller than that of BL, yet maintains a diurnal pattern (Figure 2.7d). The peak cross-shore advective heat transport for D1 during the cooling response is 23% greater than that of BL, while the warming response peak for D1 is 31% greater than that of BL (Figure 2.7e). As the downwelling-favorable alongshore forcing increases (D3),

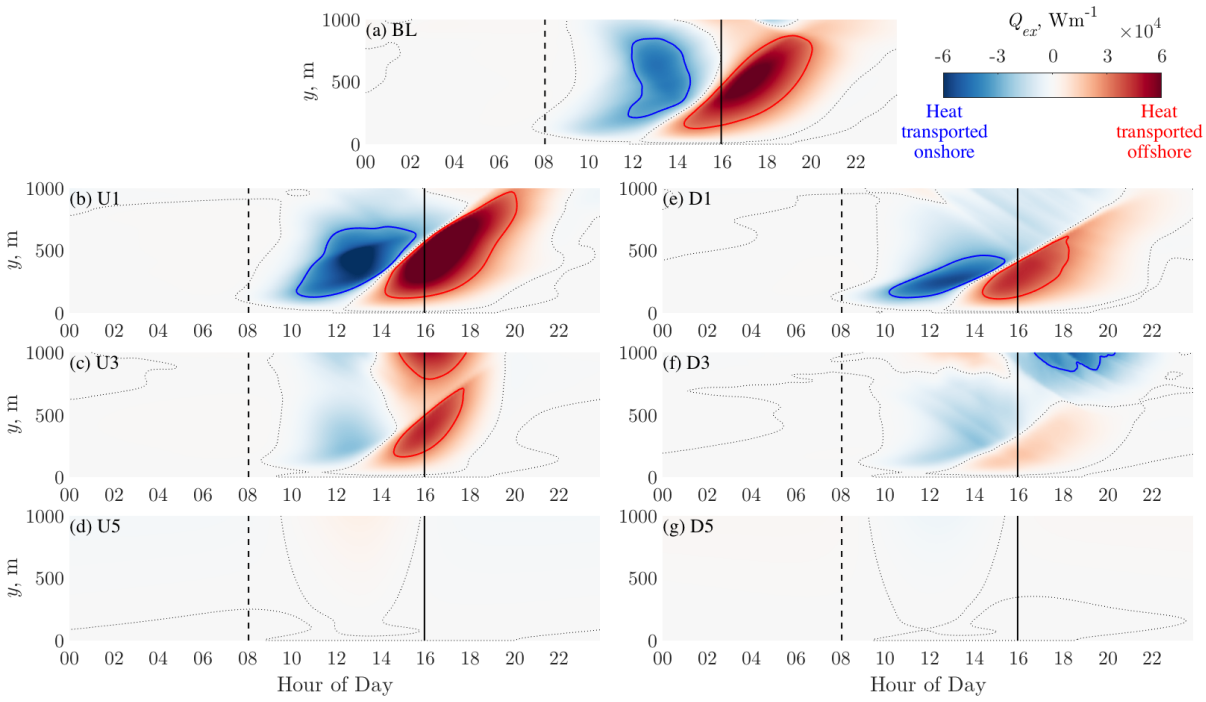

Figure 2.7: Advective cross-shore heat transport in the y-t plane for the indicated simulations. The zero contour is indicated with the black dotted line. The 3×10^4 Wm^{-1} contour, which represents the required heat transport to change the temperature inshore of the 20 m isobath by 0.1 °C in one day, is highlighted with red and blue lines.

the cooling and warming response peaks are reduced by 45% and 74%, respectively, compared to those of BL (Figure 2.7f), again occuring closer to shore. As for U5, the cross-shore advective heat transport for D5, where $u_*/u_f > 1$, is generally an order of magnitude smaller than that of BL (Figure 2.7g). For context, the contour value of 3×10^4 Wm^{-1} in Figure 2.7 represents the required heat transport to change the temperature inshore of the 20 m isobath by 0.1 °C in one day. The information presented in Figure 2.7 suggests that within the heat budget for our simulations, the cross-shore advection of heat is relatively small, consistent with an unsteady regime. To leading order, variations in advective heat transport do not create substantial temperature changes within the nearshore 1 km.

We can expect that these largely different quantities of cross-shore heat transport will, on average, establish distinct temperature structures for each scenario. These are evident in time-averaged transects of the temperature anomaly, T_{anom}, (Figure 2.8), which reveal

how upwelling- and downwelling-favorable flows modulate the time-averaged stratification established by the surface heat flux. In the absence of the alongshore forcing, the cross-shore temperature gradient is generally positive, with cold water in the tip of the domain protruding downslope (Figure 2.8a). There is an average warm surface layer beginning near y = 50 m, with a warm region offshore of approximately $y = 400$ m. In the upwelling-favorable scenarios for $u_*/u_f < 1$, the positive cross-shore temperature gradient is still present, and the warm surface layer is pushed further offshore (Figure 2.8b, c). In these scenarios, cooler water now occupies a greater vertical and cross-shore portion of the domain, and the coldest water amongst all scenarios is seen in the nearshore tip of U3 (Figure 2.8c). In sharp contrast, for the $u_*/u_f > 1$ upwelling regime, the cross-shore temperature gradient has essentially reversed, such that the warmest water is in the tip of the wedge (Figure 2.8d). Here, vertical stratification is greatly reduced, and on average, the region inshore of 1 km is warm throughout the water column.

The time-averaged T_{anom} field of D1 (Figure 2.8e) most resembles that of BL, with a nearshore region of cold water, a warm surface layer, and a positive cross-shore gradient. Compared to BL however, here for D1 the region of nearshore cool water is closer to shore. As the strength of the downwelling-favorable current is increased, a warm surface layer is still present, while warm water overwhelms the nearshore (Figure 2.8f), with an average localized region of particularly warm water within $150 < y < 400$ m. The $u_*/u_f > 1$ downwelling regime also shows a dramatic departure from the prior trend, with a reversed cross-shore gradient, warm water confined to inshore of 200 m, and considerably reduced vertical stratification (Figure 2.8g).

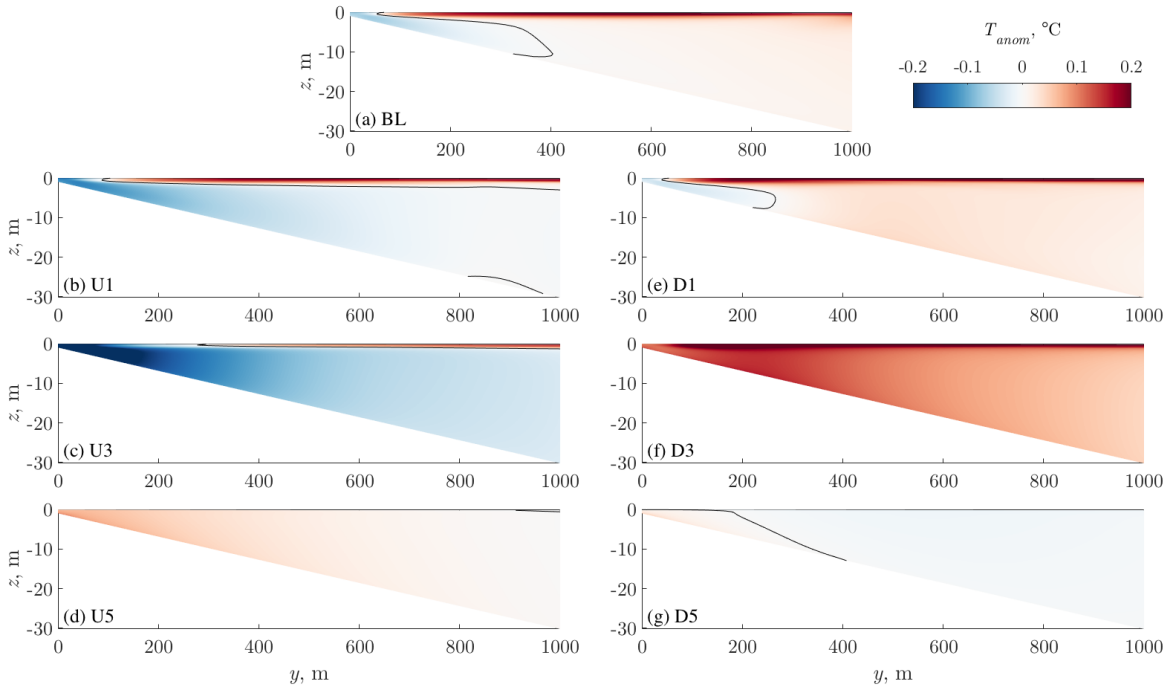

Figure 2.8: Diurnal time-averaged T_{anom} transects in the $z - y$ plane for the indicated simulations. The zero contour is indicated with a black line.

2.4 Discussion

Our model results demonstrate that thermally-driven baroclinic flows can induce the cross-shore exchange of water masses (Figure 2.5) and heat (Figure 2.7), resulting in persistent cross-shore temperature structure (Figure 2.8). Diurnal cycles in cross-shore exchange persist, and in some cases are even enhanced (e.g. U1), in scenarios with mild alongshore flow forcing ($u_*/u_f < 1$), where near-surface alongshore velocities at the 20 m isobath are ≈ 5 cm s^{-1} (U1 and D1). Within these numerical simulations, the putative effect of alongshore flow is to strengthen near-bed turbulence, therefore increasing vertical mixing and reducing the horizontal temperature gradients and baroclinic pressure gradients responsible for driving the cross-shore thermally-driven exchange. In simulations with strong alongshore flow ($u_*/u_f > 1$), in which near-surface alongshore velocities at the 20 m isobath are ≈ 0.5 m s^{-1} (U5 and D5), vertical temperature stratification, and thus baroclinic heat exchange, is negligibly small (e.g. Figure 2.7d, g).

2.4.1 The Modification of Thermally-Driven Exchange by Coriolis

From Ekman theory, we expect an alongshore flow in a rotating frame of reference will result in cross-shore transport because of the lateral veering of the current vector with distance from the bottom, due to the frictional boundary (Ekman, 1905). The resulting exchange associated with rotation arises independently from the buoyancy flux forcing. The total cross-shore exchange considered thus far has contributions from both the buoyancy-driven flow as well as rotational effects. In order to characterize the magnitude of the thermally-driven component of the exchange flow, the exchange rate for the scenarios without buoyancy flux forcing (NU1-NU6 and ND1-ND6 in Table 2.1) was computed and compared to that of their analogous simulations (U1-U6 and D1-D6). The exchange rates were averaged in both time (diurnally) and space (to the 20 m isobath), and are presented as a function of the similarly spatiotemporally-averaged ratios of u_*/u_f (Figure 2.9). It is clear that as the magnitude of the alongshore forcing increases, the thermally-driven portion of the exchange is diminished, and the exchange rate approaches that which is due only to Coriolis-driven cross-shore circulation. For $u_*/u_f \geq 1$, essentially all of the cross-shore exchange can be attributed to rotational effects, while for the mildest alongshore flow scenarios, the average exchange resulting from both buoyancy flux and alongshore flow forcings is 3-4 times the amount due solely to rotational effects. Figure 2.9 also reflects the qualitative features seen in Figure 2.5, such as the increased cross-shore exchange rate in U1 compared to BL, generally negligible *thermally-driven* exchange for $u_*/u_f > 1$, and an asymmetry between the exchange rate associated with upwelling- and downwelling-favorable alongshore forcings, as the strongest regions of exchange in the latter cases are compressed inshore compared to the upwelling-favorable cases.

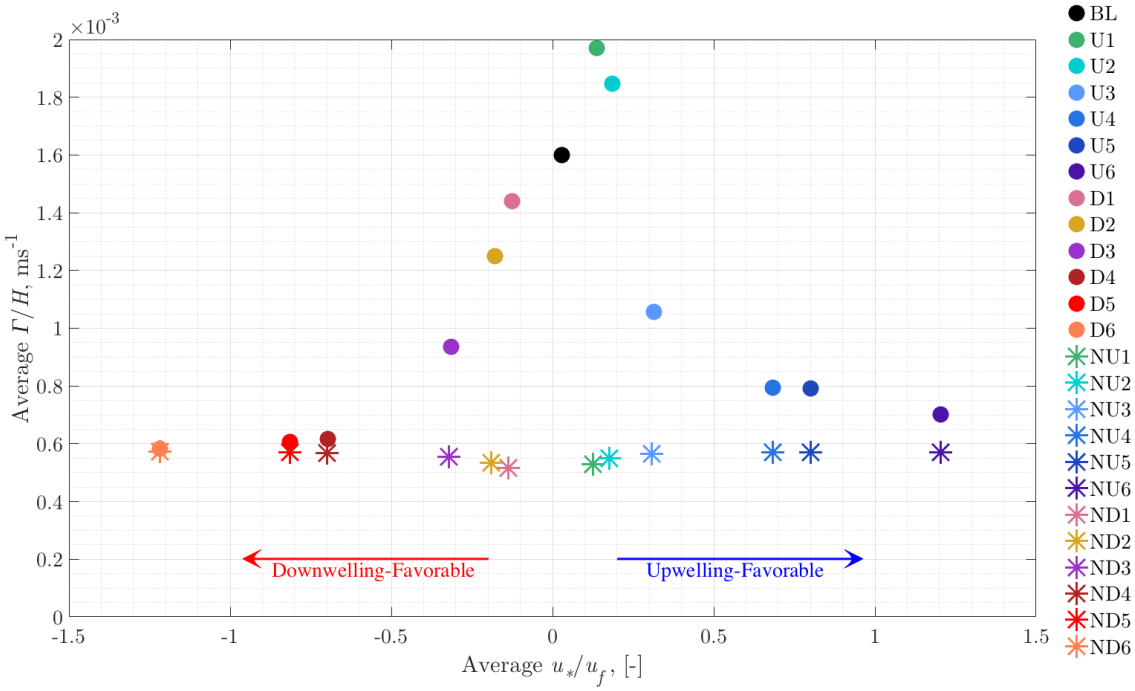

Figure 2.9: The exchange rate as a function of u_*/u_f for all runs listed in Table (2.1), where both quantities are averaged in time (diurnally) and space (to the 20 m isobath).

2.4.2 Bulk Cross-Shore Redistribution of Heat

Over a diurnal time scale, the thermally-driven cross-shore exchange establishes a cross-shore temperature gradient, the magnitude of which is modulated by varying u_*/u_f (Figure 2.8a). These diurnal timescale temperature patterns can be understood through the efficiency of the advective heat transport, Q_{ex}, in exporting or importing heat to the nearshore. During surface heating (08:00< t <16:00), the total amount of heat entering the domain at the 10 m isobath due to the surface buoyancy forcing is 3×10^9 Joules per meter alongshore distance. For BL, Q_{ex} at the 10 m isobath exports 8% of this over 24 hours. For U1, U3, D1, and D5, Q_{ex} exports 7.5%, 5.5%, 2.3%, and 0.33%, respectively, while for U5 and D3, Q_{ex} imports 0.5% and 3.2%, respectively. Decomposing the diurnal cycle into the cooling and warming responses therefore allows us to explore diurnal temperature variability associated with baroclinic cross-shore exchange. Integrated over the water column, cross-shore advective heat transport, Q_{ex}, associated with the downslope flow during the cooling

response ejects cold water offshore, thus warming the nearshore, and the opposite is true during the warming response. For BL, the peak Q_{ex} at the 10 m isobath during the warming response is approximately 50% greater than that of the cooling response (Figure 2.10a). Asymmetries in the Q_{ex} magnitudes between cooling and warming responses are facilitated by the background cross-shore circulation for a given scenario; the advective cross-shore export of heat is enhanced by upwelling, and the export of cold by downwelling (Figure 2.10). For U1 and U3, the 10 m isobath peak offshore export of heat is generally greater (16% and 85%, respectively) than the peak offshore export of cold. Conversely, the peak Q_{ex} at the 10 m isobath during the warming response for D1 and D3 is 13% and 45%, respectively, less than that of the cooling response. From Figure 2.10, it is clear that the cross-shore advective transport of heat requires a stratified water column, which for the present simulations occurs after convective cooling has yielded to net surface warming, which also allows for an advective response in the cross-shore momentum budget. Therefore, because vertical mixing substantially reduces vertical stratification for $u_*/u_f > 1$, Q_{ex} is generally 2 orders of magnitude lower for U5 and D5 than for the other simulations. For U5, there is a background cross-shore export of cold, with an intermittently strong export of heat from approximately 10:30$< t <$15:00, with a similar and opposite pattern for D5 (Figure 2.10d, g).

Defining Q_{net} as the cumulative heat input (08:00$\leq t \leq$16:00) from the buoyancy forcing as a function of cross-shore distance enables us to contextualize the bulk redistribution of heat during the cooling and warming response flows for each simulation. For BL, Q_{ex} exports a maximum of approximately 28% of the net surface heat input within the nearshore 200 m during the warming response, and imports at most only 16% during the cooling response (Figure 2.11a). Similar values apply for upwelling- and downwelling-favorable scenarios with $u_*/u_f < 1$; for U1, these values increase to 32% and 21% during warming and cooling responses, respectively (Figure 2.11b), while for D1, these values are 32% and 22%, respectively (Figure 2.11e). The cross-shore location of these peaks are closer inshore for

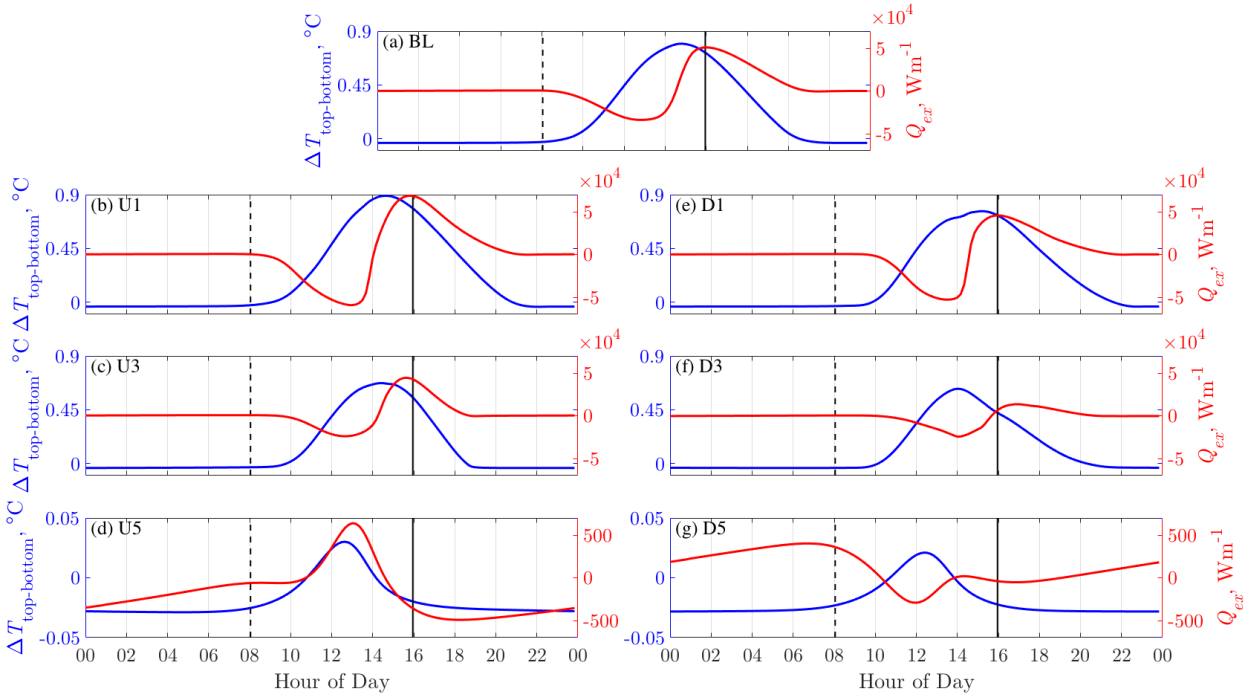

Figure 2.10: Diurnal time series of top-bottom temperature difference and Q_{ex} at the 10 m isobath for the indicated simulations. Note the smaller axis limits for panels (d) and (g).

D1 than for U1, reflecting the patterns in Γ/H and the cross-shore momentum budget discussed earlier. Q_{ex} diminishes with u_* (stronger alongshore forcing), and for U3 and D3, at most 16% and 15% of Q_{net} is exported during the warming response, respectively, within the nearshore 200 m, while a maximum of 6% of Q_{net} is imported during the cooling response for both U3 and D3 (Figure 2.11c, f). For $u_*/u_f > 1$, the cross-shore advective heat transport throughout the diurnal cycle is trivial compared to the heat input from the surface buoyancy forcing (Figure 2.11d, g). For the present simulations, the relative importance of Q_{ex} to the nearshore temperature ultimately decreases with distance offshore, reflecting the transitions in the cross-shore momentum and thermal energy budgets to an unsteady regime for large y. This is further supported by the behavior of the cross-shore advection terms seen in Figure 2.4.

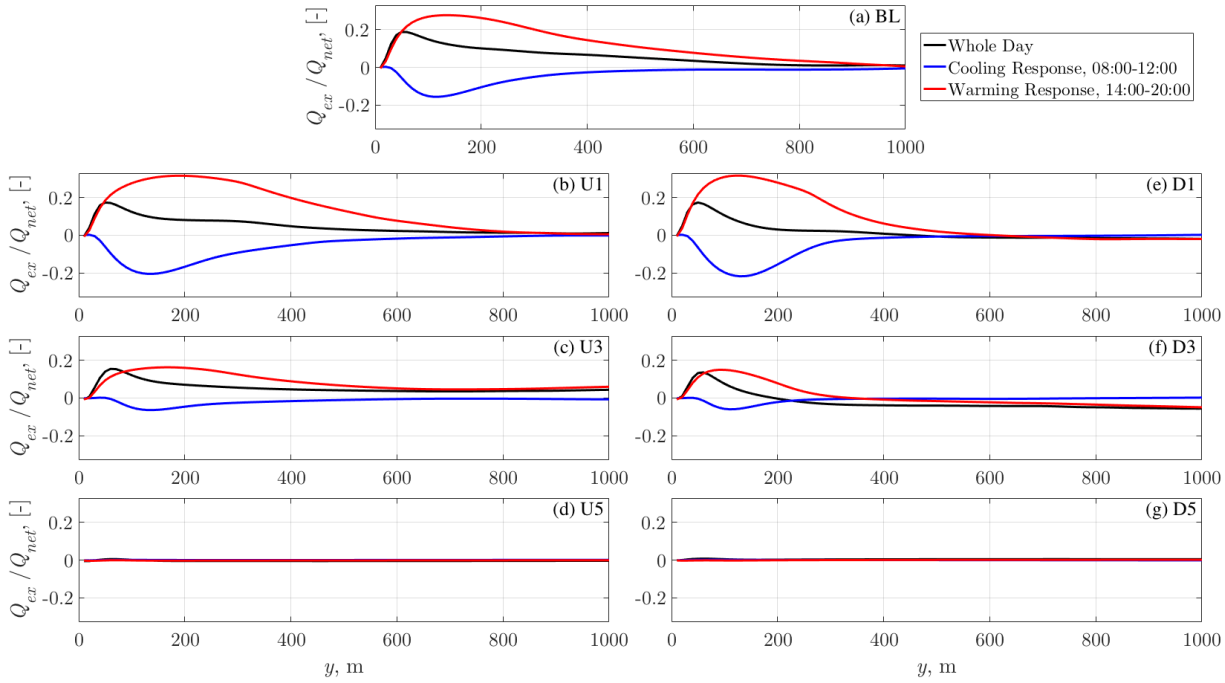

Figure 2.11: For the indicated simulations, time-integrated advective cross-shore heat transport, Q_{ex}, during diurnal (black line), cooling response (08:00 to 12:00, blue line), and warming response (14:00 to 20:00, red line) periods, divided by Q_{net}, the cumulative amount of heat entering the domain during the daytime (08:00 to 20:00) as a function of cross-shore distance.

2.5 Relevance to Nearshore Ecosystems

Periodic nearshore flushing facilitates the exchange of waters of differing nutrient concentrations, temperature, pH, salinity, and oxygen. Many coastal organisms rely on this periodic exchange for the regular supply of nutrients and larval transport (Hatcher, 1997), and as such, processes contributing directly to nearshore circulation bear significant importance to the health of coastal ecosystems. We expect thermal exchange to be particularly relevant to tropical shallow-water coasts with high optical clarity, where coral reefs typically form the ecosystem foundation. A particularly prominent feature of the thermal exchange mechanism for $u_*/u_f < 1$ is the downslope flow during the cooling response, noteworthy because in the context of coral environments, gravity currents enable corals at multiple depths to obtain heterotrophic supplies (Williams et al., 2018). However, while thermal exchange will be especially pronounced in such regions, rarely will it be the sole mechanism responsible for nearshore circulation. Of the numerous mechanisms capable of modulating thermally-driven exchange, such as alongshelf and cross-shelf wind stress, breaking waves, internal tides, and irregular bathymetry, we have focused our attention on steady alongshore currents and the ensuing vertical mixing.

Given the results of our periodically forced simulations, we can assess the impacts of alongshore currents on thermal exchange by quantifying the amount of volume and heat transported over the full 24 hour forcing cycle. As a bulk measure of the relative volume transported during one period of forcing, we define the diurnal flushing ratio as the diurnally-integrated cross-shore exchange normalized by the cross-sectional area (depth times distance from shore), as a function of y (Figure 2.12a). Figures 2.5 and 2.6 illustrate that the weak alongshore forcing cases yield stronger exchange, and here we apply this information to conclude that, in BL for example, thermally-driven exchange can flush the nearshore 200 m (7 m depth) almost twice a day. For $u_*/u_f < 1$, the exchange flushes the nearshore 200 m at least once per day, while for $u_*/u_f > 1$ only the nearshore 100 m (4 m depth) is flushed

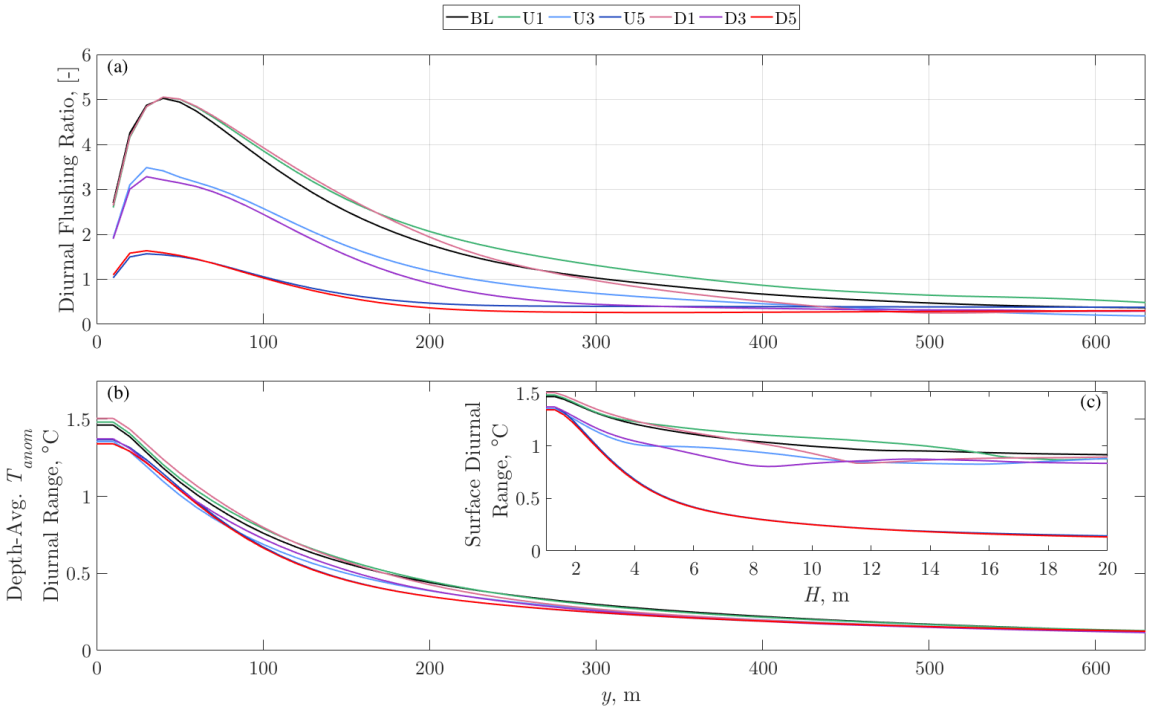

Figure 2.12: a) Diurnal flushing ratio, or the ratio of cross-shore volume exchange, Γ, to the inshore area as a function of cross-shore distance, integrated over the course of a day; b) Diurnal range in $\overline{T}_{anom}$ at each cross-shore location; c) Surface diurnal T_{anom} range. Each colored line corresponds to a simulation listed in the legend above.

diurnally. In general, all scenarios indicate that for $y \sim 1$ km, flushing approaches between approximately 20-40% of the area inshore of 1 km per day (Figure 2.12a).

Ocean temperature is of physiological relevance to a multitude of coastal organismal processes, such as the growth rate and mortality of fish larvae (Houde, 1989; Meekan et al., 2003), or the conditioning of coral reefs to acute thermal stress (Oliver and Palumbi, 2011). In the latter case, temperature variability on diurnal time scales may mitigate the prevalence or severity of bleaching (Davis et al., 2011; Safaie et al., 2018). For the idealized scenarios considered in this study, the daily range in the depth-averaged T_{anom} (which closely resembles that of the bottom) is reduced by approximately 0.7 °C within the nearshore 100 m (Figure 2.12b), decreasing with distance offshore. It is clear that within the nearshore 300 m (10 m depth), BL, U1, and D1 demonstrate a greater surface diurnal T_{anom} range than the other scenarios (Figure 2.12c); this is indicative of the role of the alongshore forcing in driving

vertical mixing, distributing the surface heating and cooling through the water column more energetically as u_*/u_f approaches and exceeds unity. Although scenarios with $u_*/u_f < 1$ demonstrate considerable nearshore flushing compared to those with $u_*/u_f > 1$ (Figure 2.12a), the difference in diurnal $\overline{T}_{anom}$ range among scenarios is marginal. Indeed, the strongest advective cross-shore heat transport only results in a small ($\sim$0.1 °C) temperature change, as shown by the highlighted contours in Figure (2.7). This implies that the cross-shore advection term in Eq. (2.6) is of secondary importance in determining the temperature field, thereby indicating an unsteady thermal regime. Knowledge of diurnal T_{anom} range as a function of u_*/u_f regimes (current speed) or depth allows for insight into the ability of corals to endure acute thermal stress events, as corals routinely exposed to diurnal-scale temperature variability may be more thermally tolerant (Safaie et al., 2018).

One of the fundamental length scales governing baroclinic cross-shore circulation over a sloped bottom driven by surface heat fluxes is the attenuation length of light through the water column. For Jerlov type I waters, more than 50% of the incident solar radiation is absorbed by the surface 1 m of the water column, and over 80% is absorbed within 20 m depth. These results therefore bear importance to coastal, as well as lake, littoral zone ecosystems, where flushing and temperature variability on diurnal time scales are of particular relevance to nutrient uptake, photosynthesis, thermal stress mitigation, and oxygen supply. Only in the most energetic of scenarios ($u_*/u_f > 1$), where enhanced vertical mixing associated with strong alongshore velocities diminishes the thermally-driven baroclinic exchange the most, is there trivial thermally-driven volume and heat transport, analogous to a coastal domain governed by shallow water Ekman dynamics.

As demonstrated by Lentz and Chapman (2004), both the slope and stratification may influence the vertical structure of the cross-shore exchange. The bottom slope is a fundamental parameter in thermal exchange theory (Mao et al., 2019; Monismith et al., 2006; Sturman et al., 1999; Farrow and Patterson, 1993), with implications for the gravity current speed,

length scales of thermal and turbulent boundary layers, and types of momentum and thermal balances. The slope has not been varied in this idealized numerical modeling investigation, and we indeed expect a variable slope to influence, for example, the speed and propagation distance of the observed convectively-driven flows, as well as the cross-shore extent of the diffusive region (Eq.2.11) where convective cooling homogenizes the water column.

All numerical simulations in this study were initialized with no stratification, and the surface buoyancy flux forcing was the sole source of stratification entering the numerical domain (excluding the influence of the offshore open boundary conditions). While the analyses presented above were derived from numerical model output retrieved after simulations attained a quasi-steady (diurnally periodic) state, we have not addressed the influence of initial stratification on the thermally-driven exchange. Stratification suppresses turbulent motion which, in the context of our simulations, arises from convective cooling or bottom stress. Therefore, we expect that variable stratification will affect the vertical structure of the veering current produced by bottom Ekman dynamics, and hence the Coriolis-driven cross-shore exchange. Additionally, we anticipate that increased stratification effectively will oppose convection during surface cooling, thereby influencing the cross-shore extent of the downslope flow, and therefore the cross-shore exchange during the cooling response.

2.6 Summary and Conclusions

We present an idealized numerical modeling investigation into thermally-driven, cross-shore exchange, and the modification of this exchange by varying upwelling- and downwelling-favorable steady alongshore flows. Within a relatively shallow coastal domain with quiescent background flow conditions, surface heat fluxes over a sloped bottom produce a baroclinic cross-shore pressure gradient that drives a vertically-sheared cross-shore velocity profile with $O(1)$ cm s^{-1} flows. This velocity profile leads to a cross-shore exchange, largely associated

with a surface warm front and a gravity current, with considerable implications for diurnal flushing of nearshore waters. Coupled with this cross-shore volume exchange, the thermal stratification established by a diurnally-periodic buoyancy flux forcing drives modest cross-shore transport of heat. Perturbing this base-case thermal exchange with a steady alongshore flow modulates the advective volume and heat transport, depending on the strength of the alongshore forcing, given by the ratio u_*/u_f. Initially, for relatively mild alongshore flows ($u_*/u_f \approx 0.2$), the strength of the cross-shore baroclinic exchange is enhanced, due to an increase in the baroclinic pressure gradient associated with the horizontal temperature gradient. As the strength of the alongshore forcing is increased, vertical mixing reduces thermal stratification as well as advective volume and heat exchange.

The idealized numerical set up used in this study was motivated by tropical reef environments, characterized by optically clear waters over steep, narrow shelves, and we expect that bathymetry and meteorological conditions will be leading-order parameters in assessing thermally-driven cross-shore exchange. Results of our numerical models demonstrate the importance of the thermal exchange mechanism in driving nearshore circulation, and are therefore applicable to studies concerned with nearshore ecosystems.

2.7 Acknowledgments

This study benefited greatly from conversations with Falk Feddersen (Scripps Institution of Oceanography), and Nirnimesh Kumar (University of Washington). Thanks to the ROMS community, particularly John Wilkin (Rutgers University), Kate Hedstrom (University of Alaska Fairbanks), John Warner (USGS), Alexander Shchepetkin (UCLA), and Jamie Pringle (University of New Hampshire), for technical support regarding the numerical model. This work would not be possible without the assistance of the UCI High Performance Computing Cluster staff, particularly Joseph Farran and Harry Mangalam. Model run setup files and

output used in this manuscript are available upon request. AS and KAD are supported by National Science Foundation (NSF) Award No. 1436254, and GP is supported by NSF Award No. 1436522.

Chapter 3

Shallow Water Bottom Ekman Dynamics Driving Cross-Shore Exchange

3.1 Introduction

The work of Ekman (1905) derived and detailed the water velocity profiles induced by a surface wind or sea-surface inclination over a rotating ocean. A fundamental consideration in Ekman's work is the ability of a water layer, through friction, to impart momentum vertically to the layer above or below it (a process Ekman referred to as "gliding"). Due to the earth's rotation, currents within adjacent layers will be deflected by a small angle from one another, such that a vertical profile of the horizontal velocity vectors through the water column produces what is known as an Ekman spiral. For an ocean of infinite depth, assuming a constant eddy viscosity, Ekman demonstrated the angle between the direction of a steady, uniform wind stress and the current at the water surface to equal 45°, and that the

transport through the water column is directed at a right angle to the wind, while for finite depths, these angles may be considerably smaller. Similarly, Ekman revealed the horizontal pressure gradients resulting from sea-surface inclinations to produce bottom currents directed 45° from the direction of the pressure gradient force (for infinite depths and constant eddy viscosity).

To date, numerous observational and analytical studies have offered amendments to Ekman's analysis within a particular scenario of interest. Welander (1957) applied Ekman's work to demonstrate that the wind stress divergence is most influential in determining the sea surface profile in shallower depths, where assumptions such as ignoring the latitudinal dependence of the Coriolis parameter are more justifiable. Cushman-Roisin and Malačič (1997) provide an analytical solution for the horizontal velocity components in the bottom Ekman layer of a deep ocean with a depth-varying eddy viscosity formulation, yielding a veering angle of less than 45°. Birchfield (1973) characterized the length and velocity scales governing coastal Ekman dynamics over a sloped bottom with the condition of no net transport normal to the coast, where the depth reduces to zero. Estrade et al. (2008) continue this analysis of coastal Ekman dynamics for an unstratified ocean subject to upwelling-favorable winds, investigating the retreat of the upwelling cell from the coast associated with the intersection of the surface and bottom boundary layers.

Bottom boundary Ekman theory, in particular, often eludes validation because observations of velocities and Reynolds stresses at the bottom are notoriously difficult to obtain. As noted by Lentz and Chapman (2004), unreliable estimates of the bottom stress, alongshelf pressure gradient, and Coriolis force obscure the depth-averaged alongshelf momentum budget, which is crucial for determining the cross-shelf flow. Furthermore, inner shelf turbulent fluxes are not readily estimated in the presence of other physical processes, notably surface gravity waves (Kirincich and Barth, 2009; Shaw and Trowbridge, 2001; Rosman et al., 2008; Lentz and Fewings, 2012). Nonetheless, Trowbridge and Lentz (1998) and Perlin et al.

(2005a) were able to present observations and analyses supporting the classical Ekman balance in the bottom boundary layer during periods of upwelling and downwelling on the northern California and Oregon shelves, respectively.

Another obstacle in characterizing bottom Ekman dynamics is the determination of the friction velocity and eddy viscosity, which themselves depend on certain local length scales. Specifically, the mixing length within an eddy viscosity model may be constrained solely by the local depth in relatively shallow regions (Mofjeld, 1988), or may be more appropriately described by the Ozmidov scale in sufficiently deep and stratified fluids (Ozmidov, 1965). To unify these ideas, Perlin et al. (2005b) present a variable length scale model that simultaneously accounts for both distance from the boundaries as well as the suppressing influence of stratification. An important parameter in this context is the ratio of the local depth to the vertical length to which the forcing (sea-surface inclination or surface wind) produce a current, typically referred to as the Ekman layer thickness. In this framework, "shallow" waters have depth less than or comparable to the Ekman layer thickness, whereas "deep" waters have depth greater than the Ekman layer thickness. This distinction is necessary because Coriolis dynamics are of more baroclinic relevance in a water column where the surface and bottom boundary layers do not overlap. For example, in relatively shallow waters, the direction of the bottom stress may be derived using the depth-averaged flow, while for moderate depths where the surface and bottom boundary layers are distinguishable, the use of a drag tensor will yield a more accurate computation of the bottom stress direction (Jenter and Madsen, 1989). Similarly, the vertical structure of an Ekman spiral, and therefore the velocity profile and resulting transport through the water column, has been shown to be highly dependent on the depth to Ekman layer thickness ratio. Kämpf (2015) demonstrates the degradation of the Ekman spiral in the transition from deep to shallow regimes, where the velocity profile is nearly aligned with the wind or pressure gradient forcing in the latter. Of more ecological pertinence, Kämpf (2015) demonstrates that the lee effect, a phenomenon in which the adverse sea surface inclination associated with offshore winds establishes an

onshore pressure gradient that leads to an upwelling-favorable undercurrent, occurs in deep water, while only unidirectional flow aligned with the pressure gradient develops in shallow water. Furthermore, in shallow water, irregularities in local bathymetry are more likely to supersede bottom boundary Ekman theory in determining the directional behavior of wind- or pressure-driven currents (Lilover et al., 2014).

An investigation into the role of steady Ekman dynamics in driving mass transport must similarly consider the assumptions Ekman made in developing his theory, mainly regarding the eddy viscosity, bathymetry, and water column height (time-variability will not be addressed in the present study). The vertically-sheared cross-shore velocity profile of an Ekman spiral with horizontal velocity components normal to a coast gives rise cross-shore exchange. The focus of this work is to examine the combined effects of friction and rotation in driving cross-shore transport. We begin with an unstratified, rotating ocean of uniform depth and constant eddy viscosity, forced only with a pressure gradient, and use finite differences of the governing equations to compute the resulting flow. This theoretical solution is then generalized by first implementing a depth-dependent eddy viscosity, and then introducing a coordinate transformation to attain the condition of zero net transport normal to a theoretical coast. We then compare results from the theoretical solution with those of a primitive equation numerical model (ROMS), which additionally allows us to determine the dynamical effects of a sloped bottom and nonlinear advection of momentum in the governing equations.

3.2 Theoretical Solution

For an unstratified, rotating ocean at steady state with uniform bathymetry, forced by a sea-surface inclination, the depth-averaged momentum equations in a coordinate system aligned

with the resulting bottom stress are:

$$g\frac{\partial \eta}{\partial x} = f\overline{v} - \frac{\tau_x^b}{\rho_0 H} \tag{3.1}$$

and

$$g\frac{\partial \eta}{\partial y} = -f\overline{u} \tag{3.2}$$

where x and y are the horizontal coordinates with respective velocity components u and v, g is the acceleration of gravity, η is the free-surface displacement, f is the Coriolis frequency, τ_x^b is the bottom stress in the x-direction, ρ_0 is the reference density, $H = h + \eta$ is the water column thickness, h is the local depth, and an overbar indicates depth-averaging. Reinserting Eqs. (3.1) and (3.2) into the corresponding 3D equations of motion, with the assumptions of an incompressible, Boussinesq fluid with an eddy viscosity model parameterizing Reynolds stresses, yields the following expressions for the depth-variable velocities:

$$u = \overline{u} + \frac{1}{f}\frac{\partial}{\partial z}\left(\nu_t \frac{\partial v}{\partial z}\right) \tag{3.3}$$

and

$$v = \overline{v} - \frac{1}{f}\left[\frac{\tau_x^b}{\rho_0 H} + \frac{\partial}{\partial z}\left(\nu_t \frac{\partial u}{\partial z}\right)\right] \tag{3.4}$$

Here z is the vertical coordinate, and ν_t is the turbulent eddy viscosity. The bottom boundary has a no-slip condition in addition to the x-directed bottom stress, while the condition of a stress-free surface is enforced:

$$\left.\frac{\partial u}{\partial z}\right|_b = \frac{\tau_x^b}{\rho_0 \nu_t} \tag{3.5a}$$

$$\left.\frac{\partial v}{\partial z}\right|_b = 0 \tag{3.5b}$$

$$u(-h) = v(-h) = 0 \tag{3.5c}$$

$$\tau_x^s = \tau_y^s = 0 \tag{3.5d}$$

Here the sub- and superscripts b and s refer to bottom and surface, respectively. The discretization of Eqs. (3.3) and (3.4) is performed using a central difference. For a generic field ϕ, the first and second order central differences are given by:

$$\left.\frac{\partial \phi}{\partial z}\right|_k = \frac{\phi_{k+1} - \phi_{k-1}}{2\Delta z} + O(\Delta z^2) \tag{3.6a}$$

$$\left.\frac{\partial^2 \phi}{\partial z^2}\right|_k = \frac{\phi_{k+1} + \phi_{k-1} - 2\phi_k}{\Delta z^2} + O(\Delta z^2) \tag{3.6b}$$

where k indexes vertically through the water column. The discretization of Eqs. (3.3) and (3.4) additionally depends on the form of ν_t, thus hereon we will proceed according to the choice of eddy viscosity model.

3.2.1 Solution with a constant eddy viscosity

The simplest case of Eqs. (3.3) and (3.4) arises from the assumption of a constant value of ν_t. Here we use a depth-averaged eddy viscosity of the form $\nu_t = 0.067 h u_*$ via Fischer et al. (1979), where $u_* = \sqrt{\frac{\tau_x^b}{\rho_0}}$ is the friction velocity. The discretization of Eqs. (3.3) and (3.4) through the water column with a vertical resolution of Δz yields:

$$u_{k+1} = 2u_k - u_{k-1} - \frac{f\Delta z^2}{\nu_t}\big(v_k - \overline{v} + \frac{\tau_x^b}{f\rho_0 H}\big) \tag{3.7}$$

and

$$v_{k+1} = 2v_k - v_{k-1} + \frac{f\Delta z^2}{\nu_t}\big(u_k - \overline{u}\big) \tag{3.8}$$

Using Eq. (3.5a), we can first find an expression for u_0:

$$\left.\frac{\partial u}{\partial z}\right|_{k=1} = \frac{u_2 - u_0}{2\Delta z} = \frac{\tau_x^b}{\rho_0 \nu_t} \tag{3.9}$$

$$u_0 = u_2 - \frac{2\Delta z \tau_x^b}{\rho_0 \nu_t}. \tag{3.10}$$

Inserting Eq. (3.10) into Eq. (3.7) for $k = 1$ and remembering $u_1 = 0$ via Eq. (3.5c) gives:

$$u_2 = \frac{\Delta z}{\nu_t}\left[\frac{\tau_x^b}{\rho_0} + \frac{f\Delta z}{2}\overline{v} - \frac{\tau_x^b \Delta z}{2\rho_0 H}\right] \tag{3.11}$$

In a similar manner, Eq. (3.5b) allows us to solve for v_2:

$$\left.\frac{\partial v}{\partial z}\right|_{k=1} = \frac{v_2 - v_0}{2\Delta z} = 0 \tag{3.12}$$

Eq. (3.12) reduces to $v_0 = v_2$, and inserting this into Eq. (3.8) for $k = 1$ gives:

$$v_2 = -\frac{1}{2}\frac{f\Delta z^2}{\nu_t}\overline{u} \tag{3.13}$$

Equipped with knowledge of u and v for $k = 1$ and 2, we are nearly ready to proceed with the iteration over all values of k to compute the horizontal velocity profiles. As Eqs. (3.11) and (3.13) require *a priori* estimates of $\overline{u}$ and $\overline{v}$, the use of a two-dimensional Newton-Raphson method enables us to solve for these depth-averaged velocities. The objective functions we seek to minimize are given by:

$$f_1(\overline{u}, \overline{v}) = \frac{1}{H}\int_{-h}^{\eta} u(z)dz - \overline{u} \tag{3.14a}$$

$$f_2(\overline{u}, \overline{v}) = \frac{1}{H}\int_{-h}^{\eta} v(z)dz - \overline{v} \tag{3.14b}$$

The Newton-Raphson iteration proceeds as follows:

1. An initial estimate is made for $\overline{u}$ and $\overline{v}$.
2. Eqs. (3.11) and (3.13) are solved.
3. Eqs. (3.7) and (3.8) are solved for the domain of k.

4. The objective functions (3.14a) and (3.14b) are then computed using the solutions for u and v and the initial estimates of $\overline{u}$ and $\overline{v}$.

5. If the absolute values of both f_1 and f_2 are below a threshold value, the procedure is terminated; otherwise, $\overline{u}$ and $\overline{v}$ are updated from their values at n to $n+1$ as:

$$\overline{\mathbf{U}}_{n+1} = \overline{\mathbf{U}}_n - J_n^{-1} F_n \tag{3.15}$$

and the procedure returns to the second step above. In Eq. (3.15), $\overline{\mathbf{U}} = \begin{bmatrix} \overline{u} \\ \overline{v} \end{bmatrix}$, $F = \begin{bmatrix} f_1 \\ f_2 \end{bmatrix}$, and the Jacobian, J, is given by:

$$J = \begin{bmatrix} \dfrac{\partial f_1}{\partial \overline{u}} & \dfrac{\partial f_1}{\partial \overline{v}} \\ \dfrac{\partial f_2}{\partial \overline{u}} & \dfrac{\partial f_2}{\partial \overline{v}} \end{bmatrix} \tag{3.16}$$

The scalars used in this theoretical solution are $g = 9.81$ m s^{-1}, $\rho_0 = 1027$ kg m^{-3}, and $f = 5.4 \times 10^{-5}$ s^{-1} (representative of tropical coasts), and the parameters are Δz, h, τ_x^b, and the threshold value. For $\Delta z = 0.001$ m, $h = 20$ m, and a threshold of 6E-12, the solution is generally found within 5 iterations for τ_x^b ranging from -0.9 to 0.9 Pa. It is convenient to present solutions in terms of the non-dimensional depth H/d_E, where d_E is the theoretical Ekman layer thickness written as:

$$d_E = \frac{2\kappa u_*}{f} \tag{3.17}$$

where we note that $\nu_t \sim \kappa u_* d$ for a given depth d, and κ is the von Kármán constant, equal to 0.41. Hence for a given depth, the ratio H/d_E decreases with increasing bottom stress.

For a constant eddy viscosity, u velocity profiles for various values of H/d_E at a depth of 20 m are shown in Fig. 3.1a, whereby the direction of the pressure gradient was varied to produce both upwelling- and downwelling-favorable flows. The solution for v (Fig. 3.1b)

reveals a velocity profile growing with distance from the bottom and reaching its maximum value at the surface. The influence of rotation in turning the velocity vector through the water column is also evidenced by the shape of the v profiles.

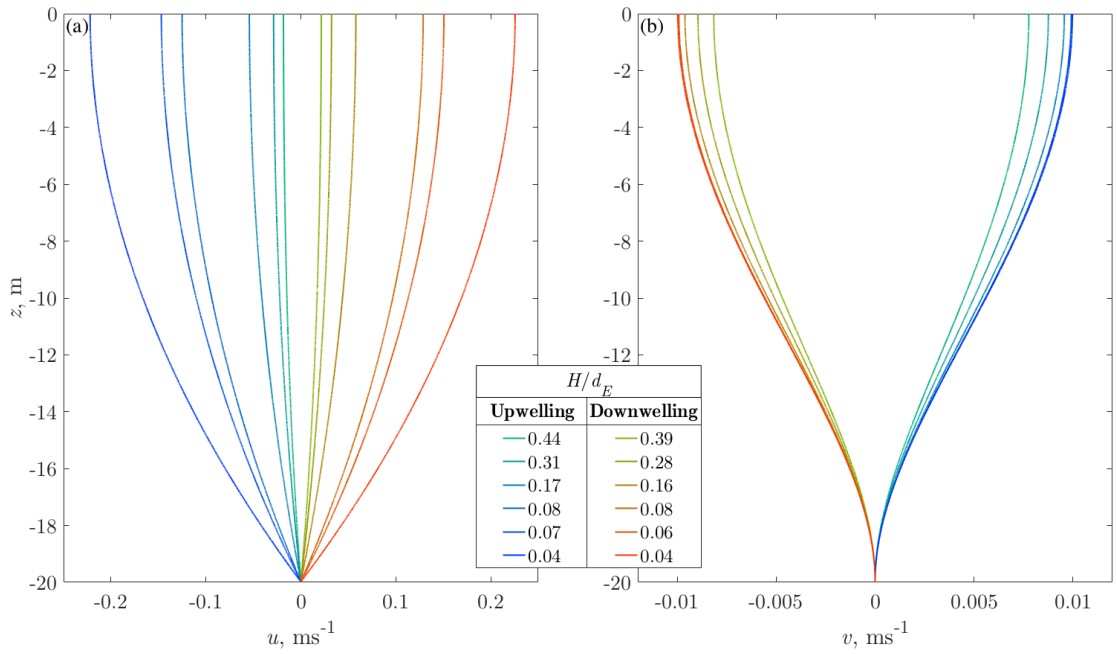

Figure 3.1: Profiles of the (a) u and (b) v velocities for various values of H/d_E at a depth of 20 m, computed from the theoretical solution using a constant eddy viscosity. For comparison with subsequent figures, the legend distinguishes between upwelling-favorable ($u_* > 0$) and downwelling-favorable ($u_* < 0$) flow scenarios.

3.2.2 Depth-Variable Eddy Viscosity

Relaxing the assumption of a constant eddy viscosity, we can rewrite the discretizations for u and v as

$$u_{k+1} = \left[\frac{1}{2\Delta z}\frac{\partial \nu_t}{\partial z}\bigg|_k + \frac{\nu_{tk}}{\Delta z^2}\right]^{-1}\left[f(\overline{v}-v_k) - \frac{\tau_x^b}{\rho_0 H} + u_{k-1}\left(\frac{1}{2\Delta z}\frac{\partial \nu_t}{\partial z}\bigg|_k - \frac{\nu_{tk}}{\Delta z^2}\right) + 2u_k\frac{\nu_{tk}}{\Delta z^2}\right] \quad (3.18)$$

and

$$v_{k+1} = \left[\frac{1}{2\Delta z}\frac{\partial \nu_t}{\partial z}\bigg|_k + \frac{\nu_{tk}}{\Delta z^2}\right]^{-1}\left[f(u_k - \overline{u}) + v_{k-1}\left(\frac{1}{2\Delta z}\frac{\partial \nu_t}{\partial z}\bigg|_k - \frac{\nu_{tk}}{\Delta z^2}\right) + 2v_k\frac{\nu_{tk}}{\Delta z^2}\right] \quad (3.19)$$

Note that in the case of a constant eddy viscosity, Eqs. (3.18) and (3.19) reduce to (3.7) and (3.8), respectively. Using Eqs. (3.11) and (3.13), we can derive expressions for u_2 and v_2 when $k = 1$ as:

$$u_2 = \left(\frac{\Delta z^2}{2\nu_{tk=1}}\right)\left[f\overline{v} - \frac{\tau_x^b}{\rho_0 H} - \left(\frac{2\Delta z \tau_x^b}{\rho_0 \nu_{tk=1}}\right)\left(\frac{1}{2\Delta z}\frac{\partial \nu_t}{\partial z}\bigg|_{k=1} - \frac{\nu_{tk=1}}{\Delta z^2}\right)\right] \quad (3.20)$$

and

$$v_2 = -\frac{f\overline{u}\Delta z^2}{2\nu_{tk=1}} \quad (3.21)$$

Perlin et al. (2005b) suggest a parabolic eddy viscosity profile, which constrains the turbulent eddy length scale by the distance from either boundary:

$$\nu_t = -\kappa u_* z\big(1 + \frac{z}{H}\big) \quad (3.22)$$

For a given value of τ_x^b, the depth-averaged value of ν_t resulting from Eq. (3.22) is approximately equal to the constant eddy viscosity given by Fischer et al. (1979). Note that in employing Eq. (3.22) to solve Eqs. (3.20) and (3.21), a singularity appears when $z = -h$. To avoid this, we begin our computational domain an arbitrary length of $z_0 = 2$ cm above the bottom, such that $z(k = 1) = -h + z_0$.

The solutions for u and v computed using a depth-variable eddy viscosity (Fig. 3.2) notably show different shapes compared to those of the constant eddy viscosity solutions. Specifically, the near-bottom gradients in the profiles of u are larger than before (Fig. 3.2a), and the magnitudes are also considerably greater than those of Fig. 3.1a. The solution for v computed using the depth-variable eddy viscosity (Fig. 3.2b) also demonstrates different

rates of momentum transfer through the water column, though the velocities are of similar magnitudes to those computed using the constant eddy viscosity.

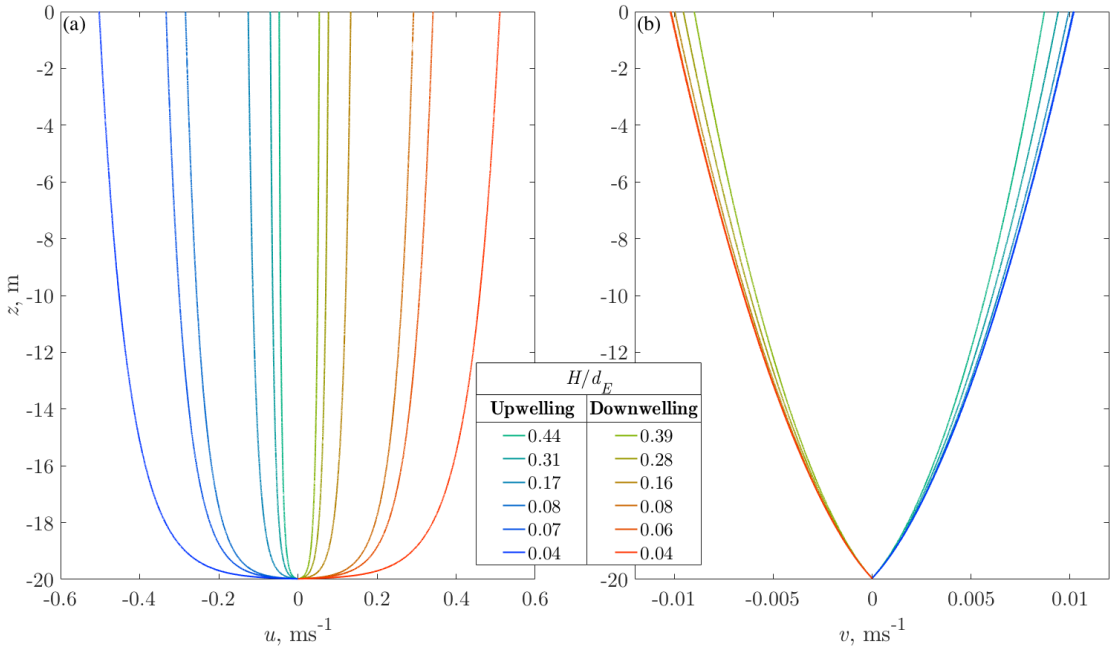

Figure 3.2: Profiles of the (a) u and (b) v velocities for various values of H/d_E at a depth of 20 m, computed from the theoretical solution using a parabolic eddy viscosity given by Eq. (3.22).

3.2.3 Imposing a Coastal Boundary

We can contextualize the theoretical model described by Eqs. (3.1)-(3.5) by imposing a coastal boundary, in which case continuity requires that cross-shore transport is zero throughout the domain, as there must be no normal transport at the coastal boundary. To accommodate this within the theoretical model, a coordinate transformation is required, such that the x-directed bottom stress will now have alongshore and cross-shore components. Note that a coastal domain necessitates a sloped bottom, whereas a locally flat bottom was assumed in developing the theoretical solution. Rotating our coordinate system from (x, y) to (x', y')

by an angle θ (Fig. 3.3), where x' is aligned with the coast and y' is normal to it, yields:

$$\tau_x^b \cos(\theta) = \tau_{x'}^b \tag{3.23}$$

and

$$\tau_x^b \sin(\theta) = \tau_{y'}^b \tag{3.24}$$

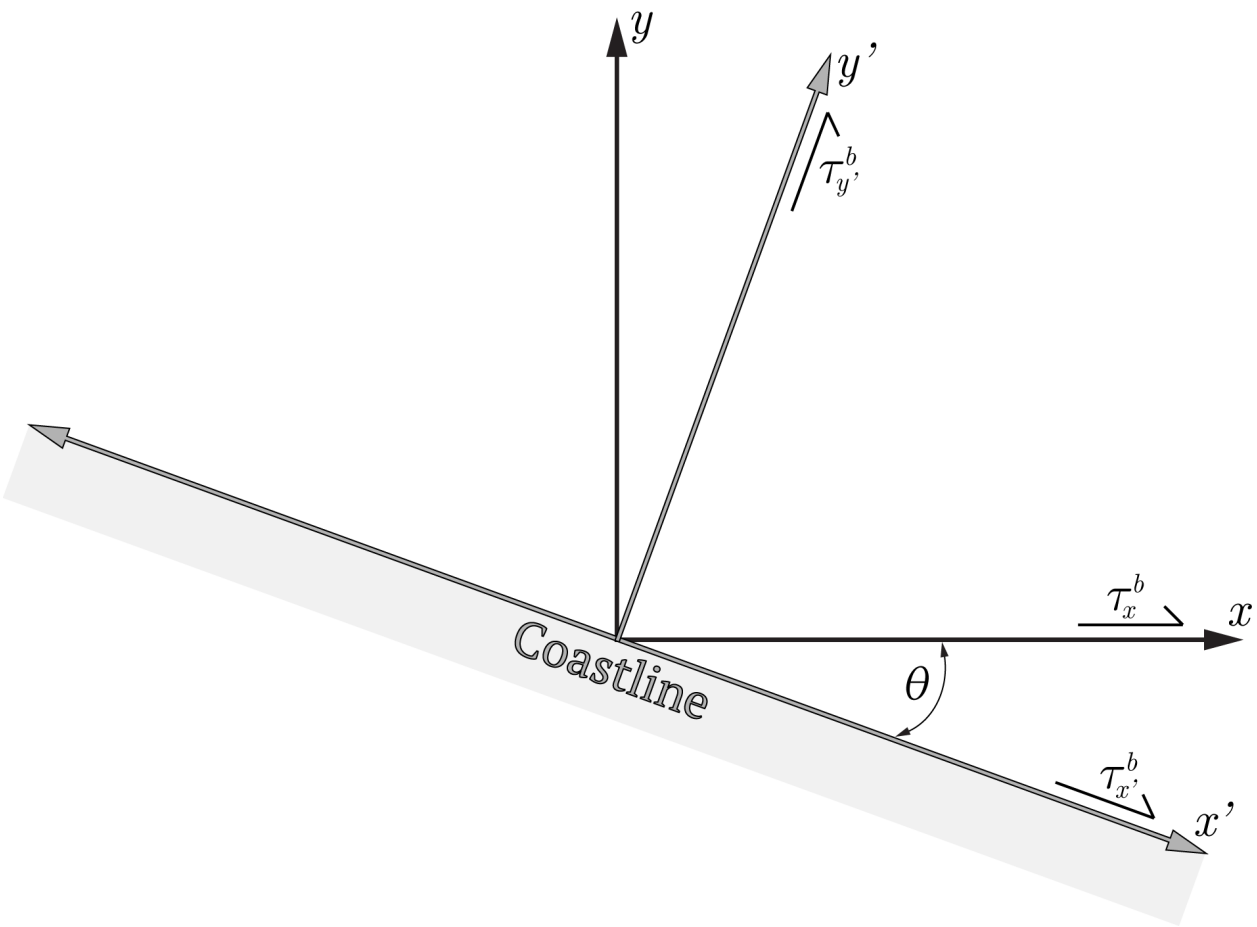

Figure 3.3: Top view of arbitrary (x, y) coordinate system with an applied x-directed bottom stress, τ_x^b, and rotated coordinate system with alongshore and cross-shore components denoted by x' and y', respectively. Rotating the (x, y) axis by an angle of θ results in alongshore and cross-shore bottom stress components of $\tau_{x'}^b$ and $\tau_{y'}^b$, respectively. The coastal boundary is shaded in grey.

Defining T as the two-dimensional transformation matrix for rotation about the z-axis:

$$T = \begin{pmatrix} \cos\theta & \sin\theta \\ -\sin\theta & \cos\theta \end{pmatrix} \tag{3.25}$$

allows us to write (u', v'), the alongshore and cross-shore velocity components, respectively, as:

$$\begin{pmatrix} u' \\ v' \end{pmatrix} = T \begin{pmatrix} u \\ v \end{pmatrix} = \begin{pmatrix} u\cos\theta + v\sin\theta \\ -u\sin\theta + v\cos\theta \end{pmatrix} \tag{3.26}$$

Enforcing the coastal boundary condition and using the definition of depth-averaging, we have:

$$\int_{-h}^{\eta} v' dz = \int_{-h}^{\eta} \big(- u\sin\theta + v\cos\theta \big) dz = 0 \tag{3.27}$$

and

$$H(\overline{v}\cos\theta - \overline{u}\sin\theta) = 0 \tag{3.28}$$

Finally, solving for θ yields:

$$\theta = \arctan\big(\overline{v}/\overline{u}\big) \tag{3.29}$$

The effect of the coordinate transformation on the alongshore and cross-shore velocities relative to u and v is clear from Eq. (3.26). For small values of θ, as can be expected given a purely x-directed bottom stress, $\cos\theta \gg \sin\theta$, and the v contribution to u' is inevitably trivial, such that u' will closely resemble u (Fig. 3.4a). However, v' is modulated by the competing contributions from u, which dominates near the bottom where v is small, and v, which grows with distance from the bottom, hence the zero-crossing in the v' profiles (Fig. 3.4b). Accordingly, the depth-integral of v' over the water column vanishes.

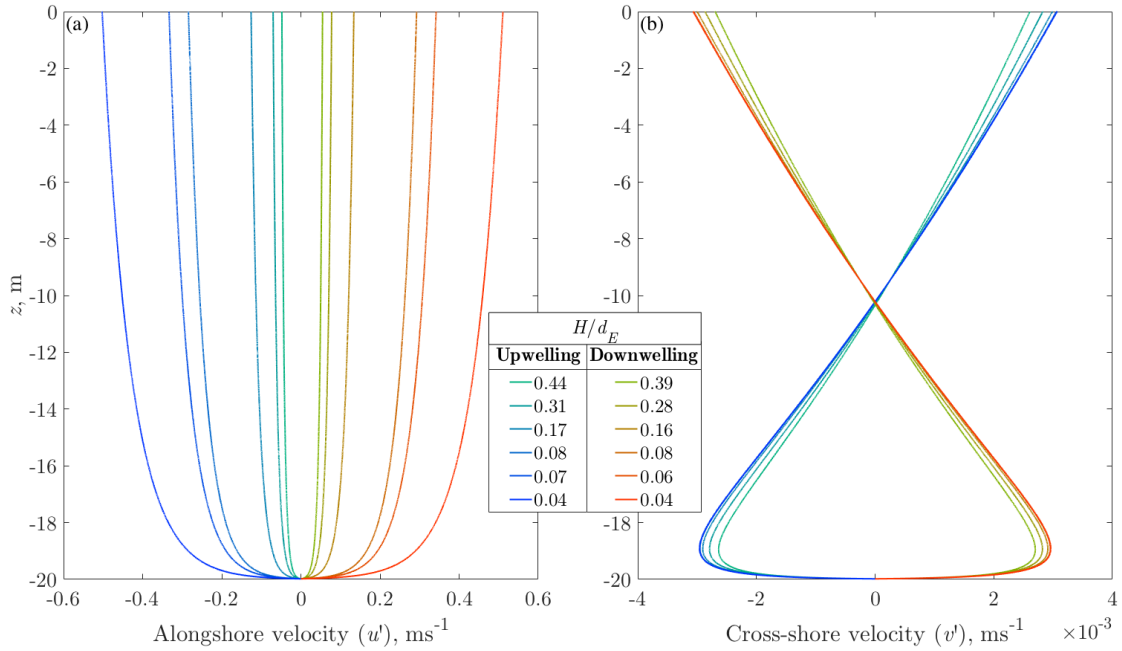

Figure 3.4: Results for (a) alongshore and (b) cross-shore velocity profiles from the theoretical solution for a coastal boundary.

3.3 ROMS Simulations

The steady-state response of an unstratified, rotating ocean over a sloped bottom, forced with upwelling- and downwelling-favorable alongshore currents is examined using the Regional Ocean Modeling System (ROMS), a hydrostatic primitive equation model with stretched terrain-following coordinates in the vertical and multiple turbulence closure options (Song and Haidvogel, 1994; Shchepetkin and McWilliams, 2005; Haidvogel et al., 2008; Warner et al., 2005). The complete details of the model setup are described in Safaie et al. (prep), and are briefly outlined here. The computational domain is 1 km and 5 km in the alongshore and cross-shore directions, respectively, with a uniform lateral resolution of 10 m, a bottom slope of 0.03, minimum and maximum depths of 1 m and 151 m, respectively, 30 vertical grid points, and uniform bathymetry in the alongshore dimension. Simulations are initialized from rest with no stratification, and are integrated for 10 days of simulation time, with a baroclinic time step of 2 s. The boundary conditions for the free-surface, momentum,

tracer, and turbulent kinetic energy (TKE) fields are periodic at the alongshore ends and closed onshore. At the offshore boundary, the free-surface and 2D momentum fields are set to the conditions of Chapman (1985) and Mason et al. (2010), respectively, the 3D momentum fields are set to the radiation condition of Orlanski (1976), and the TKE field has a gradient boundary condition. A logarithmic bottom drag formulation with a bottom roughness parameter of 2 cm is activated, and the ROMS default advection schemes of third-order upstream-biased for 3D horizontal momentum (Shchepetkin and McWilliams, 2005), and fourth-order centered difference for 2D horizontal and 3D vertical momentum are used.

The ROMS simulations in this study implement upwelling- and downwelling-favorable alongshore currents through a steady pressure gradient (implemented via an alongshore-uniform kinematic momentum flux that is scaled with depth), and applied as a body force to the water column in the alongshore direction. For comparison to the theoretical model presented in this study, the ROMS bottom stress values at a given isobath were prescribed as parameters to the theoretical model, such that the theoretical and ROMS results would have the same H/d_E values (Table 3.1). Additionally, eddy viscosity profiles from the ROMS simulations were used in the theoretical model. The eddy viscosity in the ROMS simulations was computed from a two-equation $k-\epsilon$ turbulence closure (Rodi, 1987), and implemented in ROMS as a generic length scale (GLS) approach (Umlauf and Burchard, 2003; Warner et al., 2005). An important distinction between the theoretical model and ROMS simulations is that the former assumes a uniform depth and neglects the nonlinear advection of momentum in Eqs. (3.1)-(3.4), whereas the ROMS equations of motion retain the advection terms (i.e. $\mathbf{v} \cdot \nabla u$) and are solved over a sloping bottom.

The velocity profiles from the theoretical solution (with ROMS-derived ν_t) and ROMS are in qualitative agreement (Fig. 3.5). The alongshore velocities demonstrate the behavior of a shallow turbulent boundary layer (Fig. 3.5a), and the cross-shore velocities show a vertically-sheared exchange profile, with a vanishing depth-average (Fig. 3.5b).

Upwelling-Favorable		**Downwelling-Favorable**	
u_*, ms^{-1}	H/d_E	u_*, ms^{-1}	H/d_E
0.003	0.44	-0.0034	0.39
0.0043	0.31	-0.0047	0.28
0.0075	0.17	-0.008	0.16
0.0168	0.08	-0.0173	0.08
0.0197	0.07	-0.0202	0.06
0.0297	0.04	-0.0302	0.04

Table 3.1: List of u_* and H/d_E parameters at a depth of 20 m, used to obtain alongshore and cross-shore velocities computed from the theoretical solution and ROMS.

Near-surface alongshore velocities for the theoretical solution and ROMS are in near agreement (to within 7%); for upwelling-favorable flows, the difference increases with H/d_E, while for downwelling-favorable flows, the difference decreases with H/d_E. Near-surface cross-shore velocities between the two models for both upwelling- and downwelling-favorable flows are also in good agreement, and the difference increases with H/d_E (Fig. 3.5b).

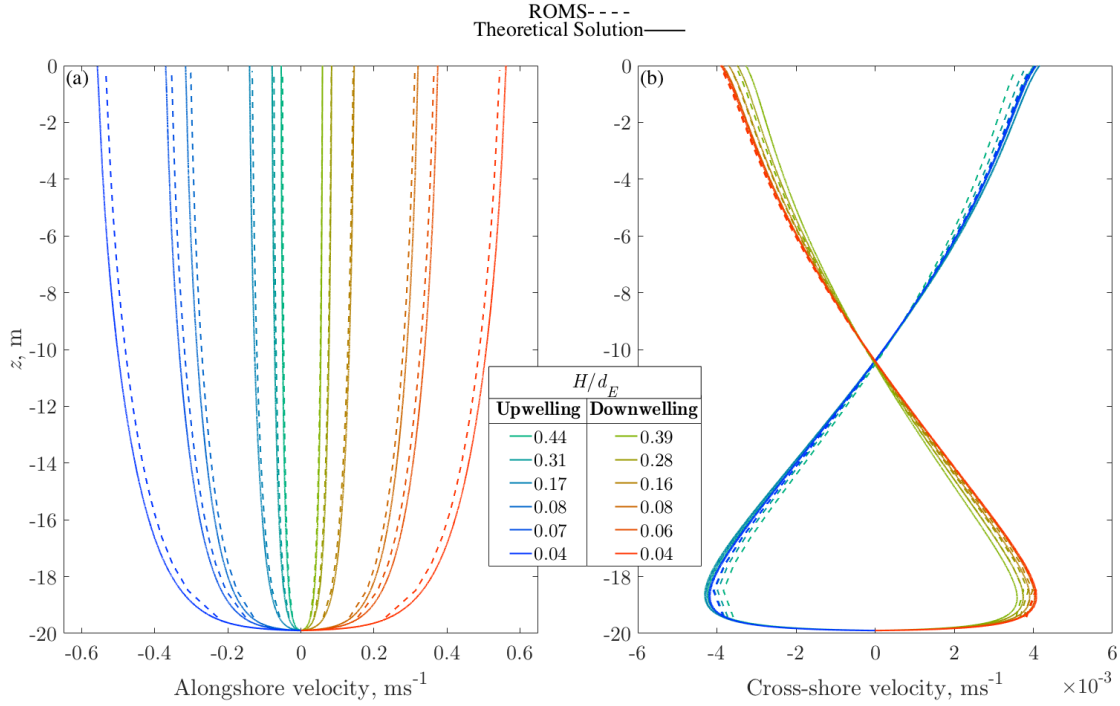

Figure 3.5: Alongshore (a) and cross-shore (b) velocity profiles at a depth of 20 m from ROMS (dashed lines) and the theoretical solution (solid lines).

A pragmatic metric for comparing the cross-shore velocities from the theoretical solution

to those of ROMS, one that is also of ecological pertinence, can be computed by depth-normalizing the cross-shore advective volume exchange given by Molina et al. (2014):

$$\gamma = \frac{1}{2H}\int_{-h}^{\eta} |v'(z) - \overline{v'}|dz \tag{3.30}$$

The quantity γ can be interpreted as a depth-averaged baroclinic velocity scale, allowing for the comparison of scalar values between the ROMS results and the theoretical solution. Indeed, as the magnitude of the alongshore forcing increases, the discrepancy in the results of the two models is reduced (Fig. 3.6). For upwelling-favorable flows, the theoretical solution shows larger γ compared to ROMS, with a difference of 9.4% for $H/d_E = 0.44$, and 0.45% for $H/d_E = 0.04$. For downwelling-favorable flows, γ for the theoretical solution is lower than it is for the ROMS results, with a difference of -7.5% for $H/d_E = 0.39$, and -1.8% for $H/d_E = 0.04$.

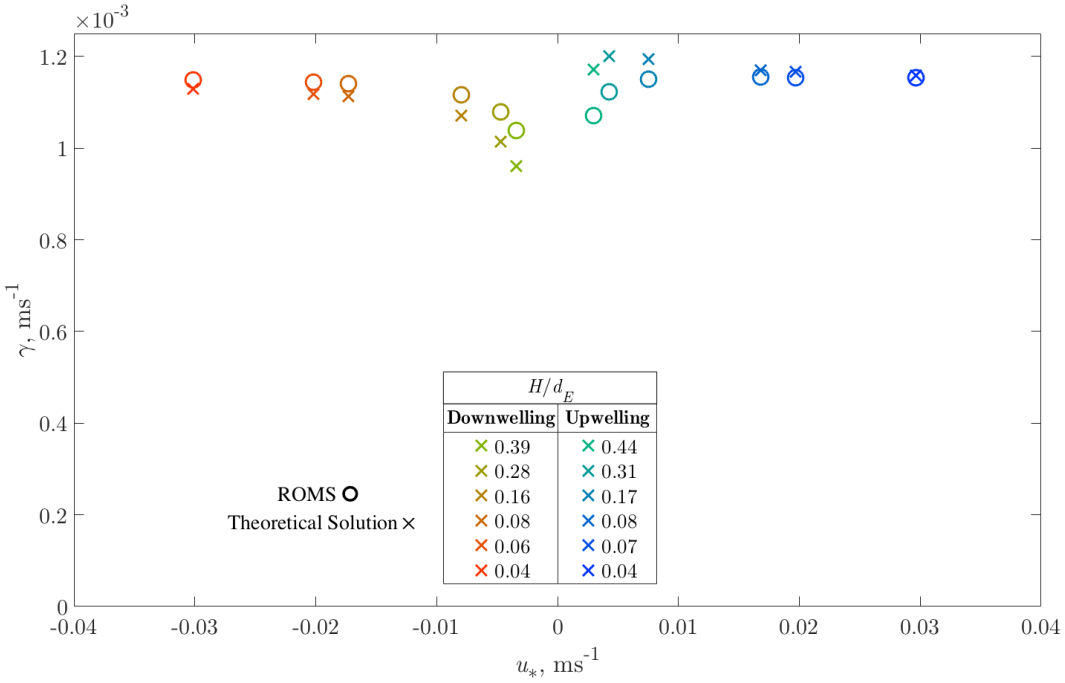

Figure 3.6: γ, or depth-normalized cross-shore advective volume exchange, at a depth of 20 m from ROMS and the theoretical solution as a function of u_*.

3.4 Discussion

For both the theoretical solution and ROMS, velocity profiles show the strongest gradient near the bottom. Though the magnitude of the alongshore velocity increases with increasing pressure gradient forcing, the cross-shore velocity profiles for different H/d_E values are of similar magnitudes. This is due to a balance between the Coriolis acceleration and turbulent diffusion in the baroclinic cross-shore momentum budget. While the differences in cross-shore velocities between the theoretical solution and ROMS are relatively small for increasing H/d_E, it is evident from Figure 3.6 that upwelling- and downwelling-favorable γ values for the theoretical solution systematically deviate from those of ROMS, such that γ is larger for the theoretical solution during upwelling-favorable flows, and larger for ROMS during downwelling-favorable flows. The momentum equations governing the theoretical solution (i.e. Eqs. (3.1)-(3.4)) exclude contributions from nonlinear advection, whereas such terms are included in the alongshore and cross-shore momentum balances within the ROMS simulations. Within the alongshore momentum balance, an important consequence of the cross-shore advection term is discussed in Lentz and Chapman (2004); for upwelling-favorable flows, faster alongshore momentum at the surface is transported offshore, while slower alongshore momentum near the bottom is brought onshore, establishing a net inshore deficit of alongshore momentum. Conversely, for downwelling-favorable flows, the faster, near-surface alongshore momentum is transported onshore, while slower alongshore momentum near the bottom travels offshore, resulting in a net inshore surplus of alongshore momentum. Remembering that $\overline{v'} = 0$ by definition, it is clear from Eq. (3.30) that γ depends on the magnitude of v'. Therefore, rearranging the baroclinic alongshore momentum balance applicable to the steady, alongshore-uniform ROMS simulations reveals the link between the cross-shore advection of alongshore momentum and γ:

$$fv' = v'\frac{\partial u'}{\partial y} + w\frac{\partial u'}{\partial z} - \frac{\partial}{\partial z}\left(\nu_t \frac{\partial u'}{\partial z}\right) \tag{3.31}$$

For a given bottom stress, retaining the advection terms implies that the inshore momentum deficit during upwelling-favorable flows will reduce v', and therefore γ, while for downwelling-favorable flows, the inshore momentum surplus will increase v' and hence γ (Fig. 3.6).

Although the magnitude of the pressure gradient is equal between corresponding upwelling- and downwelling-favorable ROMS scenarios, the resulting friction velocity magnitudes differ slightly (Table 3.1). The reason for this can be identified upon examining the appropriate depth-integrated alongshore momentum balance:

$$-\frac{\tau^b_{x'}}{\rho_0} \sim gH\frac{\partial \eta}{\partial x} + \int_{-h}^{\eta} v'\frac{\partial u'}{\partial y}dz \tag{3.32}$$

Here we see the direct correspondence between the friction velocity ($u_* = \sqrt{\tau^b_{x'}/\rho_0}$) and the cross-shore advection of alongshore momentum. The inshore deficit of alongshore momentum for upwelling-favorable flows will lower u_*, while the inshore surplus for downwelling-favorable flows will increase u_*. This also reveals why the values of H/d_E for the downwelling-favorable scenarios are less than those for the upwelling-favorable scenarios, as H/d_E is proportional to $1/u_*$. Furthermore, as the eddy viscosity scales with u_*, the values of ν_t for downwelling-favorable flows will be larger than those for upwelling-favorable flows (Fig. 3.7). As a result, stronger frictional momentum transfer will reduce v', and therefore γ, in the downwelling-favorable scenarios at a given depth compared to the upwelling-favorable scenarios. This is evidenced by the asymmetry between the upwelling- and downwelling-favorable γ values in Fig. 3.6.

We have neglected the effects of stratification in the development of the theoretical model presented here. We expect stratification will be important, however, as stratification suppresses turbulent motion, and will not only confine the vertical extent of the veering Ekman layer (Perlin et al., 2007), but also modulate the vertical structure of the cross-shore circulation. Indeed, the role of stratification on a sloped shelf under steady, wind-

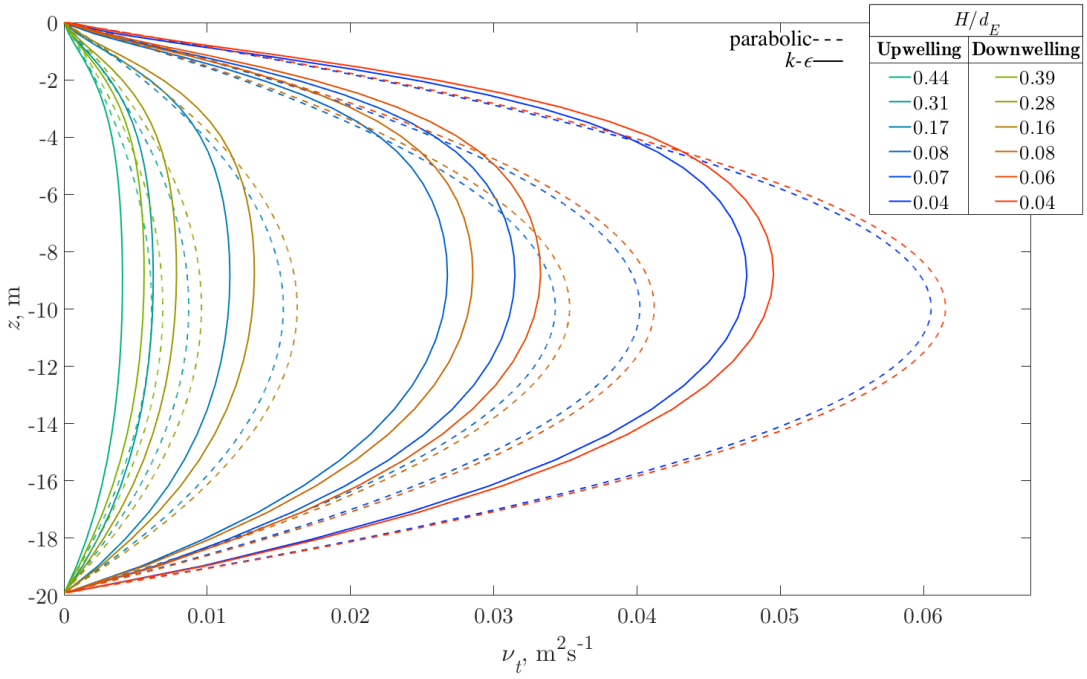

Figure 3.7: Parabolic eddy viscosity profiles (dotted lines) of the form given by Eq. (3.22), and from the ROMS $k-\epsilon$ turbulence closure (solid lines).

driven flow was investigated by Lentz and Chapman (2004). Their analysis characterized the structure of upwelling-favorable cross-shelf circulation as a function of the bottom slope and buoyancy frequency, determining that for weakly stratified conditions, the wind stress is balanced by bottom stress, and the onshore flow occurs predominantly in the bottom boundary layer, while for increased stratification, the relative importance of the bottom stress in the alongshelf momentum balance is reduced, and the subsurface onshore flow occurs above the bottom boundary layer. Hence, the future consideration of density gradients in our theoretical model will yield a more refined assessment of the vertical structure of the cross-shore flow, which may be of particular interest to ecological studies of cross-shelf transport in which the vertical distribution of nutrients and extent of photosynthesis are consequential.

3.5 Summary and Conclusions

The horizontal velocity profiles induced by a bottom stress applied over an alongshore-uniform domain in a rotating, unstratified ocean at steady-state were computed from a theoretical model of the classical Ekman balances. Analysis is limited to the dependence of the resulting flow on the form of the eddy viscosity. For a rotating ocean, the horizontal current driven by an alongshore pressure gradient will veer through the water column due to the influence of friction, attaining cross-shore velocity components and therefore driving cross-shore exchange. The theoretical model is therefore placed in the context of coastal regions by introducing a sloping bottom and a coordinate system transformation, enforcing the condition of zero cross-shore transport. An eddy viscosity computed from a $k-\epsilon$ turbulence closure is inserted into the theoretical solution for comparison against the results of a primitive equation model (ROMS) with the same forcing. Here, the role of nonlinear advection of momentum becomes apparent. The consequence of retaining these terms in the governing equations is that the vertically-sheared cross-shore velocity profile establishes an inshore deficit of alongshore momentum for upwelling-favorable flows, and an inshore surplus for downwelling-favorable flows. Compared to the theoretical model, the ROMS results therefore show greater advective cross-shore volume exchange for downwelling-favorable flows, and less for upwelling-favorable flows. Results are expected to be important to ecological studies of cross-shelf exchange in nearshore environments.

Bibliography

Ainsworth, T. D., Heron, S. F., Ortiz, J. C., Mumby, P. J., Grech, A., Ogawa, D., Eakin, C. M., and Leggat, W. (2016). Climate change disables coral bleaching protection on the Great Barrier Reef. *Science*, 352(6283):338–342.

Austin, J. A. and Lentz, S. J. (2002). The inner shelf response to wind-driven upwelling and downwelling. *Journal of Physical Oceanography*, 32(7):2171–2193.

Australian Institute of Marine Science (AIMS). (2017a). Sea Water Temperature Logger Data at Bird Island, From 14 Feb 2013 To 04 Feb 2016. `http://data.aims.gov.au/metadataviewer/faces/view.xhtml?uuid=bf04b7d7-583e-4cff-bf1f-e5ed5add34c1`. accessed 27/04/2017.

Australian Institute of Marine Science (AIMS). (2017b). Sea Water Temperature Logger Data at Border Island, From 24 Mar 2011 To 18 Jan 2015. `http://data.aims.gov.au/metadataviewer/faces/view.xhtml?uuid=c3a08a7e-c29d-4a38-9e61-c2cd1a996b49`. accessed 27/04/2017.

Australian Institute of Marine Science (AIMS). (2017c). Sea Water Temperature Logger Data at Cattle Bay, Great Barrier Reef From 11 Feb 1993 To 06 Jun 2016. `http://data.aims.gov.au/metadataviewer/faces/view.xhtml?uuid=c6d2c182-7c07-4d7b-b9d4-a5b9c73f8aaa`. accessed 27/04/2017.

Australian Institute of Marine Science (AIMS). (2017d). Sea Water Temperature Logger Data at Chicken Reef, Great Barrier Reef From 27 Apr 1996 To 30 Jul 2016. `http://data.aims.gov.au/metadataviewer/faces/view.xhtml?uuid=f0436176-ee83-4f3a-babd-34eadd6d140d`. accessed 27/04/2017.

Australian Institute of Marine Science (AIMS). (2017e). Sea Water Temperature Logger Data at Davies Reef, Great Barrier Reef From 02 May 1996 To 28 Mar 2016. `http://data.aims.gov.au/metadataviewer/faces/view.xhtml?uuid=0ba80e4d-eeb9-4b34-9fff-fc6d2787bad1`. accessed 27/04/2017.

Australian Institute of Marine Science (AIMS). (2017f). Sea Water Temperature Logger Data at Daydream Island, Great Barrier Reef From 26 Jun 1996 To 06 May 2016. `http://data.aims.gov.au/metadataviewer/faces/view.xhtml?uuid=9ea12078-6571-4baf-9d47-e91c556967c2`. accessed 27/04/2017.

Australian Institute of Marine Science (AIMS). (2017g). Sea Water Temperature Logger Data at Dent Island, Great Barrier Reef From 18 Dec 2005 To 11 Jul 2015. http://data.aims.gov.au/metadataviewer/faces/view.xhtml?uuid=f2a2d747-06cf-4d24-b9cd-310ca719216e. accessed 27/04/2017.

Australian Institute of Marine Science (AIMS). (2017h). Sea Water Temperature Logger Data at Geoffrey Bay, Great Barrier Reef From 20 Nov 1991 To 08 Jun 2016. http://data.aims.gov.au/metadataviewer/faces/view.xhtml?uuid=cb760466-76dc-4e32-84b6-a7bd5a8ef806. accessed 27/04/2017.

Australian Institute of Marine Science (AIMS). (2017i). Sea Water Temperature Logger Data at Halfway Island, Great Barrier Reef From 07 Dec 1995 To 11 Aug 2013. http://data.aims.gov.au/metadataviewer/faces/view.xhtml?uuid=9a661fb5-ba2f-4b7f-8e9d-d3d007932eff. accessed 27/04/2017.

Australian Institute of Marine Science (AIMS). (2017j). Sea Water Temperature Logger Data at Hardy Reef, Great Barrier Reef From 13 Jun 2002 To 20 Nov 2002. http://data.aims.gov.au/metadataviewer/faces/view.xhtml?uuid=fc73ac05-a4a7-4bcb-931d-c246f47aed93. accessed 27/04/2017.

Australian Institute of Marine Science (AIMS). (2017k). Sea Water Temperature Logger Data at Heron Island, Great Barrier Reef From 24 Nov 1995 To 30 Mar 2015. http://data.aims.gov.au/metadataviewer/faces/view.xhtml?uuid=446a0e73-7c30-4712-9ddb-ba1fc29b8b9a. accessed 27/04/2017.

Australian Institute of Marine Science (AIMS). (2017l). Sea Water Temperature Logger Data at Kelso Reef, Great Barrier Reef From 04 Jul 1995 To 02 Jul 2015. http://data.aims.gov.au/metadataviewer/faces/view.xhtml?uuid=43950f6a-0ee7-4291-bed8-c6f9a90ce15f. accessed 27/04/2017.

Australian Institute of Marine Science (AIMS). (2017m). Sea Water Temperature Logger Data at Low Isles, Great Barrier Reef From 30 Mar 1996 To 05 Sep 2016. http://data.aims.gov.au/metadataviewer/faces/view.xhtml?uuid=ef62b2ad-bfd2-41b3-8c1d-c89715052c64. accessed 27/04/2017.

Australian Institute of Marine Science (AIMS). (2017n). Sea Water Temperature Logger Data at Miall, Great Barrier Reef From 27 Apr 2010 To 02 Mar 2011. http://data.aims.gov.au/metadataviewer/faces/view.xhtml?uuid=c7ffcbab-813f-469f-be0c-25a434f78612. accessed 27/04/2017.

Australian Institute of Marine Science (AIMS). (2017o). Sea Water Temperature Logger Data at Middle Island, Great Barrier Reef From 07 Dec 1995 To 15 Jul 1997. http://data.aims.gov.au/metadataviewer/faces/view.xhtml?uuid=b7195bb8-d017-4d8a-9778-e164b6eae835. accessed 27/04/2017.

Australian Institute of Marine Science (AIMS). (2017p). Sea Water Temperature Logger Data at Middle Reef, Great Barrier Reef From 25 Jan 1996 To

02 Nov 2012. http://data.aims.gov.au/metadataviewer/faces/view.xhtml?uuid=42994f7d-ddef-4509-9fef-49d6fc8e246b. accessed 27/04/2017.

Australian Institute of Marine Science (AIMS). (2017q). Sea Water Temperature Logger Data at Myrmidon Reef, Great Barrier Reef From 13 Apr 1995 To 04 Jun 2015. http://data.aims.gov.au/metadataviewer/faces/view.xhtml?uuid=1342bfa4-57e9-4d8a-ac77-1ec34ec2d16b. accessed 27/04/2017.

Australian Institute of Marine Science (AIMS). (2017r). Sea Water Temperature Logger Data at Nelly Bay, Great Barrier Reef From 25 Jan 1996 To 02 Nov 2012. http://data.aims.gov.au/metadataviewer/faces/view.xhtml?uuid=0e781a14-fbac-482d-afdd-e348c4996ea9. accessed 27/04/2017.

Australian Institute of Marine Science (AIMS). (2017s). Sea Water Temperature Logger Data at Norman Reef, Great Barrier Reef From 25 Mar 1996 To 11 Aug 2011. http://data.aims.gov.au/metadataviewer/faces/view.xhtml?uuid=56dd3569-eb17-466c-b139-7ea491d5b4b7. accessed 27/04/2017.

Australian Institute of Marine Science (AIMS). (2017t). Sea Water Temperature Logger Data at North Keppel Island, Great Barrier Reef From 07 Dec 1995 To 13 May 2015. http://data.aims.gov.au/metadataviewer/faces/view.xhtml?uuid=d825864f-e3a1-4465-9efb-aeb581458610. accessed 27/04/2017.

Australian Institute of Marine Science (AIMS). (2017u). Sea Water Temperature Logger Data at Orpheus Island, Great Barrier Reef From 07 Jul 2011 To 16 Apr 2015. http://data.aims.gov.au/metadataviewer/faces/view.xhtml?uuid=b3035761-4ea4-4bdd-a64e-45871a9c94bb. accessed 27/04/2017.

Australian Institute of Marine Science (AIMS). (2017v). Sea Water Temperature Logger Data at Pelorus Island, Great Barrier Reef From 04 Aug 1993 To 19 Sep 2016. http://data.aims.gov.au/metadataviewer/faces/view.xhtml?uuid=6f58a3d8-6c3d-4e22-8a9e-4cdf08e861ca. accessed 27/04/2017.

Australian Institute of Marine Science (AIMS). (2017w). Sea Water Temperature Logger Data at Pioneer Bay, Great Barrier Reef From 08 Mar 1992 To 07 Jul 2011. http://data.aims.gov.au/metadataviewer/faces/view.xhtml?uuid=594050fd-fe1e-4921-9b87-4ccd4835e974. accessed 27/04/2017.

Australian Institute of Marine Science (AIMS). (2017x). Sea Water Temperature Logger Data at Wallace Islet, Great Barrier Reef From 21 Nov 1996 To 23 Oct 2013. http://data.aims.gov.au/metadataviewer/faces/view.xhtml?uuid=dc97de8f-a9e9-4922-99c2-30b29e376f46. accessed 27/04/2017.

Baird, A. and Marshall, P. (2002). Mortality, growth and reproduction in scleractinian corals following bleaching on the Great Barrier Reef. *Marine Ecology Progress Series*, 237:133–141.

Baker, A. C., Glynn, P. W., and Riegl, B. (2008). Climate change and coral reef bleaching: An ecological assessment of long-term impacts, recovery trends and future outlook. *Estuarine, Coastal and Shelf Science*, 80(4):435–471.

Baker, A. C., McClanahan, T. R., Starger, C. J., and Boonstra, R. K. (2013). Long-term monitoring of algal symbiont communities in corals reveals stability is taxon dependent and driven by site-specific thermal regime. *Marine Ecology Progress Series*, 479:85–97.

Barshis, D. J., Ladner, J. T., Oliver, T. A., Seneca, F. O., Traylor-Knowles, N., and Palumbi, S. R. (2013). Genomic basis for coral resilience to climate change. *Proceedings of the National Academy of Sciences*, 110(4):1387–1392.

Belsley, D. A., Kuh, E., and Welsch, R. E. (2005). *Regression diagnostics: Identifying influential data and sources of collinearity*, volume 571. John Wiley & Sons.

Berkelmans, R. (2002). Time-integrated thermal bleaching thresholds of reefs and their variation on the Great Barrier Reef. *Marine Ecology Progress Series*, 229:73–82.

Berkelmans, R., De'ath, G., Kininmonth, S., and Skirving, W. J. (2004). A comparison of the 1998 and 2002 coral bleaching events on the Great Barrier Reef: spatial correlation, patterns, and predictions. *Coral Reefs*, 23(1):74–83.

Berkelmans, R., Jones, A. M., and Schaffelke, B. (2012). Salinity thresholds of Acropora spp. on the Great Barrier Reef. *Coral Reefs*, 31(4):1103–1110.

Berkelmans, R. and Oliver, J. (1999). Large-scale bleaching of corals on the Great Barrier Reef. *Coral Reefs*, 18(1):55–60.

Berkelmans, R. and Van Oppen, M. J. (2006). The role of zooxanthellae in the thermal tolerance of corals: a 'nugget of hope' for coral reefs in an era of climate change. *Proceedings of the Royal Society B: Biological Sciences*, 273(1599):2305–2312.

Birchfield, G. E. (1973). An Ekman model of coastal currents in a lake or shallow sea. *Journal of Physical Oceanography*, 3(4):419–428.

Boylan, P. and Kleypas, J. (2008). New insights into the exposure and sensitivity of coral reefs to ocean warming. In *Proc 11th Int Coral Reef Symp*, volume 2, pages 854–858.

Brant, R. (1990). Assessing proportionality in the proportional odds model for ordinal logistic regression. *Biometrics*, pages 1171–1178.

Brink, K. (2016). Cross-shelf exchange. *Annual Review of Marine Science*, 8:59–78.

Brown, B. E., Dunne, R. P., Goodson, M., and Douglas, A. (2000). Bleaching patterns in reef corals. *Nature*, 404(6774):142–143.

Burnham, K. P. and Anderson, D. R. (2002). A practical information-theoretic approach. *Model Selection and Multimodel Inference, 2nd ed. Springer, New York*, 2.

Cantin, N. E. and Lough, J. M. (2014). Surviving coral bleaching events: Porites growth anomalies on the Great Barrier Reef. *PloS One*, 9(2):e88720.

Carilli, J., Donner, S. D., and Hartmann, A. C. (2012). Historical temperature variability affects coral response to heat stress. *PLoS One*, 7(3):e34418.

Casey, K., Selig, E., Zhang, D., Saha, K., Krishnan, A., and McMichael, E. (2015). The Coral Reef Temperature Anomaly Database (CoRTAD) Version 5—Global, 4 km sea surface temperature and related thermal stress metrics for 1982–2012. *NOAA National Centers for Environmental Information. Dataset. doi*, 10:V5CZ3545.

Castillo, K. and Helmuth, B. (2005). Influence of thermal history on the response of Montastraea annularis to short-term temperature exposure. *Marine Biology*, 148(2):261–270.

Castillo, K. D., Ries, J. B., Weiss, J. M., and Lima, F. P. (2012). Decline of forereef corals in response to recent warming linked to history of thermal exposure. *Nature Climate Change*, 2(10):756–760.

Chapman, D. C. (1985). Numerical treatment of cross-shelf open boundaries in a barotropic coastal ocean model. *Journal of Physical Oceanography*, 15(8):1060–1075.

Chollett, I., Enríquez, S., and Mumby, P. J. (2014). Redefining thermal regimes to design reserves for coral reefs in the face of climate change. *PLoS One*, 9(10):e110634.

Coenen, W., Sánchez, A., Félez, R., Davis, K., and Pawlak, G. (in review). Residual streaming flows in buoyancy-driven cross-shore exchange.

Conand, F., Marsac, F., Tessier, E., and Conand, C. (2008). A ten-year period of daily sea surface temperature at a coastal station in Reunion Island, Indian Ocean (July 1993–April 2004): patterns of variability and biological responses. *Western Indian Ocean Journal of Marine Science*, 6(1).

Costanza, R., De Groot, R., Sutton, P., Van der Ploeg, S., Anderson, S. J., Kubiszewski, I., Farber, S., and Turner, R. K. (2014). Changes in the global value of ecosystem services. *Global Environmental Change*, 26:152–158.

Cowen, R. K. and Sponaugle, S. (2009). Larval dispersal and marine population connectivity. *Annual Review of Marine Science*.

Craig, P., Birkeland, C., and Belliveau, S. (2001). High temperatures tolerated by a diverse assemblage of shallow-water corals in American Samoa. *Coral Reefs*, 20(2):185–189.

Cushman-Roisin, B. and Malačič, V. (1997). Bottom Ekman pumping with stress-dependent eddy viscosity. *Journal of Physical Oceanography*, 27(9):1967–1975.

Darling, E. S., McClanahan, T. R., and Côté, I. M. (2013). Life histories predict coral community disassembly under multiple stressors. *Global Change Biology*, 19(6):1930–1940.

Davis, K., Lentz, S., Pineda, J., Farrar, J., Starczak, V., and Churchill, J. (2011). Observations of the thermal environment on Red Sea platform reefs: a heat budget analysis. *Coral Reefs*, 30(1):25–36.

Davis, K. A., Leichter, J. J., Hench, J. L., and Monismith, S. G. (2008). Effects of western boundary current dynamics on the internal wave field of the Southeast Florida shelf. *Journal of Geophysical Research: Oceans*, 113(C9).

Davis, K. A. and Monismith, S. G. (2011). The modification of bottom boundary layer turbulence and mixing by internal waves shoaling on a barrier reef. *Journal of Physical Oceanography*, 41(11):2223–2241.

DeCarlo, T. M., Cohen, A. L., Wong, G. T., Davis, K. A., Lohmann, P., and Soong, K. (2017). Mass coral mortality under local amplification of 2 °C ocean warming. *Scientific Reports*, 7:44586.

Donner, S. D. (2011). An evaluation of the effect of recent temperature variability on the prediction of coral bleaching events. *Ecological Applications*, 21(5):1718–1730.

Dunn, S., Thomason, J., Le Tissier, M., and Bythell, J. (2004). Heat stress induces different forms of cell death in sea anemones and their endosymbiotic algae depending on temperature and duration. *Cell Death & Differentiation*, 11(11):1213–1222.

Edmunds, P. J. (2013). Decadal-scale changes in the community structure of coral reefs of St. John, US Virgin Islands. *Marine Ecology Progress Series*, 489:107–123.

Ekman, V. W. (1905). On the influence of the earth's rotation on ocean-currents.

Elvidge, C. D., Dietz, J. B., Berkelmans, R., Andrefouet, S., Skirving, W., Strong, A. E., and Tuttle, B. T. (2004). Satellite observation of Keppel Islands (Great Barrier Reef) 2002 coral bleaching using IKONOS data. *Coral Reefs*, 23(1):123–132.

Estrade, P., Marchesiello, P., De Verdière, A. C., and Roy, C. (2008). Cross-shelf structure of coastal upwelling: A two—dimensional extension of Ekman's theory and a mechanism for inner shelf upwelling shut down. *Journal of Marine Research*, 66(5):589–616.

Falkowski, P. G., Barber, R. T., and Smetacek, V. (1998). Biogeochemical controls and feedbacks on ocean primary production. *Science*, 281(5374):200–206.

Falter, J. L., Lowe, R. J., Zhang, Z., and McCulloch, M. (2013). Physical and biological controls on the carbonate chemistry of coral reef waters: effects of metabolism, wave forcing, sea level, and geomorphology. *PloS One*, 8(1):e53303.

Farrow, D. and Patterson, J. (1993). On the response of a reservoir sidearm to diurnal heating and cooling. *Journal of Fluid Mechanics*, 246:143–161.

Fischer, H. B., List, J. E., Koh, C. R., Imberger, J., and Brooks, N. H. (1979). *Mixing in inland and coastal waters*. Elsevier.

Fitt, W. K., McFarland, F., Warner, M. E., and Chilcoat, G. C. (2000). Seasonal patterns of tissue biomass and densities of symbiotic dinoflagellates in reef corals and relation to coral bleaching. *Limnology and Oceanography*, 45(3):677–685.

Furby, K. A., Bouwmeester, J., and Berumen, M. L. (2013). Susceptibility of central Red Sea corals during a major bleaching event. *Coral Reefs*, 32(2):505–513.

Glynn, P. (1993). Coral reef bleaching: ecological perspectives. *Coral Reefs*, 12(1):1–17.

Goreau, T., McClanahan, T., Hayes, R., and Strong, A. (2000). Conservation of coral reefs after the 1998 global bleaching event. *Conservation Biology*, 14(1):5–15.

Goreau, T. J. and Hayes, R. L. (1994). Coral bleaching and ocean "hot spots". *Ambio-Journal of Human Environment Research and Management*, 23(3):176–180.

Graham, M. H. (2003). Confronting multicollinearity in ecological multiple regression. *Ecology*, 84(11):2809–2815.

Graham, N. A., Jennings, S., MacNeil, M. A., Mouillot, D., and Wilson, S. K. (2015). Predicting climate-driven regime shifts versus rebound potential in coral reefs. *Nature*, 518(7537):94–97.

Green, D. H., Edmunds, P. J., Pochon, X., and Gates, R. D. (2010). The effects of substratum type on the growth, mortality, and photophysiology of juvenile corals in St. John, US Virgin Islands. *Journal of Experimental Marine Biology and Ecology*, 384(1-2):18–29.

Grottoli, A. G., Rodrigues, L. J., and Palardy, J. E. (2006). Heterotrophic plasticity and resilience in bleached corals. *Nature*, 440(7088):1186–1189.

Grottoli, A. G., Warner, M. E., Levas, S. J., Aschaffenburg, M. D., Schoepf, V., McGinley, M., Baumann, J., and Matsui, Y. (2014). The cumulative impact of annual coral bleaching can turn some coral species winners into losers. *Global Change Biology*, 20(12):3823–3833.

Gruber, R. K., Lowe, R. J., and Falter, J. L. (2017). Metabolism of a tide-dominated reef platform subject to extreme diel temperature and oxygen variations. *Limnology and Oceanography*, 62(4):1701–1717.

Guadayol, O., Silbiger, N. J., Donahue, M. J., and Thomas, F. I. (2014). Patterns in temporal variability of temperature, oxygen and pH along an environmental gradient in a coral reef. *PloS One*, 9(1):e85213.

Guisan, A. and Harrell, F. E. (2000). Ordinal response regression models in ecology. *Journal of Vegetation Science*, 11(5):617–626.

Haidvogel, D. B., Arango, H., Budgell, W. P., Cornuelle, B. D., Curchitser, E., Di Lorenzo, E., Fennel, K., Geyer, W. R., Hermann, A. J., Lanerolle, L., et al. (2008). Ocean forecasting in terrain-following coordinates: Formulation and skill assessment of the Regional Ocean Modeling System. *Journal of Computational Physics*, 227(7):3595–3624.

Hatcher, B. G. (1997). Coral reef ecosystems: how much greater is the whole than the sum of the parts? *Coral Reefs*, 16(1):S77–S91.

Herdman, L. M., Hench, J. L., and Monismith, S. G. (2015). Heat balances and thermally driven lagoon-ocean exchanges on a tropical coral reef system (Moorea, French Polynesia). *Journal of Geophysical Research: Oceans*, 120(2):1233–1252.

Hoegh-Guldberg, O., Mumby, P. J., Hooten, A. J., Steneck, R. S., Greenfield, P., Gomez, E., Harvell, C. D., Sale, P. F., Edwards, A. J., Caldeira, K., et al. (2007). Coral reefs under rapid climate change and ocean acidification. *Science*, 318(5857):1737–1742.

Houde, E. D. (1989). Comparative growth, mortality, and energetics of marine fish larvae: temperature and implied latitudinal effects. *Fishery Bulletin*, 87(3):471–495.

Hughes, T. P., Kerry, J. T., Álvarez-Noriega, M., Álvarez-Romero, J. G., Anderson, K. D., Baird, A. H., Babcock, R. C., Beger, M., Bellwood, D. R., Berkelmans, R., et al. (2017). Global warming and recurrent mass bleaching of corals. *Nature*, 543(7645):373–377.

Hurvich, C. M. and Tsai, C.-L. (1989). Regression and time series model selection in small samples. *Biometrika*, 76(2):297–307.

Ilıcak, M., Özgökmen, T. M., Peters, H., Baumert, H. Z., and Iskandarani, M. (2008). Performance of two-equation turbulence closures in three-dimensional simulations of the Red Sea overflow. *Ocean Modelling*, 24(3-4):122–139.

Jackson, L., Hallberg, R., and Legg, S. (2008). A parameterization of shear-driven turbulence for ocean climate models. *Journal of Physical Oceanography*, 38(5):1033–1053.

Jenter, H. L. and Madsen, O. S. (1989). Bottom stress in wind-driven depth-averaged coastal flows. *Journal of Physical Oceanography*, 19(7):962–974.

Jerlov, N. G. (1976). *Marine optics*. Elsevier.

Jokiel, P., Rosenberg, E., and Loya, Y. (2004). Coral health and disease.

Kämpf, J. (2015). Interference of wind-driven and pressure gradient-driven flows in shallow homogeneous water bodies. *Ocean Dynamics*, 65(11):1399–1410.

Kirincich, A. R. and Barth, J. A. (2009). Time-varying across-shelf Ekman transport and vertical eddy viscosity on the inner shelf. *Journal of Physical Oceanography*, 39(3):602–620.

Kleypas, J. A., McManus, J. W., and Menez, L. A. (1999). Environmental limits to coral reef development: where do we draw the line? *American Zoologist*, 39(1):146–159.

Large, W. G., McWilliams, J. C., and Doney, S. C. (1994). Oceanic vertical mixing: A review and a model with a nonlocal boundary layer parameterization. *Reviews of Geophysics*, 32(4):363–403.

Lei, C. and Patterson, J. C. (2006). Natural convection induced by diurnal heating and cooling in a reservoir with slowly varying topography. *JSME International Journal Series B Fluids and Thermal Engineering*, 49(3):605–615.

Leichter, J. J., Deane, G., and Stokes, M. (2005). Spatial and temporal variability of internal wave forcing on a coral reef. *Journal of Physical Oceanography*, 35(11):1945–1962.

Leichter, J. J. and Miller, S. L. (1999). Predicting high-frequency upwelling: Spatial and temporal patterns of temperature anomalies on a Florida coral reef. *Continental Shelf Research*, 19(7):911–928.

Leichter, J. J., Wing, S. R., Miller, S. L., and Denny, M. W. (1996). Pulsed delivery of subthermocline water to Conch Reef (Florida Keys) by internal tidal bores. *Limnology and Oceanography*, 41(7):1490–1501.

Lentz, S., Churchill, J., Davis, K., Farrar, J., Pineda, J., and Starczak, V. (2016). The characteristics and dynamics of wave-driven flow across a platform coral reef in the Red Sea. *Journal of Geophysical Research: Oceans*, 121(2):1360–1376.

Lentz, S. J. and Chapman, D. C. (2004). The importance of nonlinear cross-shelf momentum flux during wind-driven coastal upwelling. *Journal of Physical Oceanography*, 34(11):2444–2457.

Lentz, S. J., Fewings, M., Howd, P., Fredericks, J., and Hathaway, K. (2008). Observations and a model of undertow over the inner continental shelf. *Journal of Physical Oceanography*, 38(11):2341–2357.

Lentz, S. J. and Fewings, M. R. (2012). The wind-and wave-driven inner-shelf circulation. *Annual Review of Marine Science*, 4:317–343.

Lesser, M. P. and Farrell, J. H. (2004). Exposure to solar radiation increases damage to both host tissues and algal symbionts of corals during thermal stress. *Coral Reefs*, 23(3):367–377.

Lilover, M.-J., Pavelson, J., and Kõuts, T. (2014). On the nature of low-frequency currents over a shallow area of the southern coast of the Gulf of Finland. *Journal of Marine Systems*, 129:66–75.

Liu, G., Heron, S. F., Eakin, C. M., Muller-Karger, F. E., Vega-Rodriguez, M., Guild, L. S., De La Cour, J. L., Geiger, E. F., Skirving, W. J., Burgess, T. F., et al. (2014). Reef-scale thermal stress monitoring of coral ecosystems: new 5-km global products from NOAA Coral Reef Watch. *Remote Sensing*, 6(11):11579–11606.

Liu, G., Strong, A. E., Skirving, W., and Arzayus, L. F. (2006). Overview of NOAA coral reef watch program's near-real time satellite global coral bleaching monitoring activities. In *Proceedings of the 10th international coral reef symposium*, volume 1793, pages 1783–1793.

Logan, C. A., Dunne, J., Eakin, C., and Donner, S. (2012). A framework for comparing coral bleaching thresholds. In *Proceedings of the 12th International Coral Reef Symposium (ed Yellowlees D, Hughes TP), pp 10A3 Townsville [Internet]*.

Lowe, R. J., Falter, J. L., Monismith, S. G., and Atkinson, M. J. (2009). Wave-driven circulation of a coastal reef–lagoon system. *Journal of Physical Oceanography*, 39(4):873–893.

Lowe, R. J., Pivan, X., Falter, J., Symonds, G., and Gruber, R. (2016). Rising sea levels will reduce extreme temperature variations in tide-dominated reef habitats. *Science Advances*, 2(8):e1600825.

Manzello, D. P., Berkelmans, R., and Hendee, J. C. (2007). Coral bleaching indices and thresholds for the Florida reef tract, Bahamas, and St. Croix, US Virgin Islands. *Marine Pollution Bulletin*, 54(12):1923–1931.

Mao, Y., Lei, C., and Patterson, J. C. (2019). Natural convection in a reservoir induced by sinusoidally varying temperature at the water surface. *International Journal of Heat and Mass Transfer*, 134:610–627.

Marques, G. M. and Özgökmen, T. M. (2014). On modeling turbulent exchange in buoyancy-driven fronts. *Ocean Modelling*, 83:43–62.

Marshall, P. and Baird, A. (2000). Bleaching of corals on the Great Barrier Reef: differential susceptibilities among taxa. *Coral Reefs*, 19(2):155–163.

Mason, E., Molemaker, J., Shchepetkin, A. F., Colas, F., McWilliams, J. C., and Sangrà, P. (2010). Procedures for offline grid nesting in regional ocean models. *Ocean Modelling*, 35(1-2):1–15.

Maynard, J., Anthony, K., Marshall, P., and Masiri, I. (2008a). Major bleaching events can lead to increased thermal tolerance in corals. *Marine Biology*, 155(2):173–182.

Maynard, J. A., Turner, P. J., Anthony, K. R., Baird, A. H., Berkelmans, R., Eakin, C. M., Johnson, J., Marshall, P. A., Packer, G. R., Rea, A., et al. (2008b). Reeftemp: An interactive monitoring system for coral bleaching using high-resolution SST and improved stress predictors. *Geophysical Research Letters*, 35(5).

McClanahan, T. and Maina, J. (2003). Response of coral assemblages to the interaction between natural temperature variation and rare warm-water events. *Ecosystems*, 6(6):551–563.

McClanahan, T., Maina, J., Moothien-Pillay, R., and Baker, A. C. (2005). Effects of geography, taxa, water flow, and temperature variation on coral bleaching intensity in Mauritius. *Marine Ecology Progress Series*, 298:131–142.

McClanahan, T., Muthiga, N., and Mangi, S. (2001). Coral and algal changes after the 1998 coral bleaching: interaction with reef management and herbivores on Kenyan reefs. *Coral Reefs*, 19(4):380–391.

McClanahan, T. R., Ateweberhan, M., Muhando, C. A., Maina, J., and Mohammed, M. S. (2007a). Effects of climate and seawater temperature variation on coral bleaching and mortality. *Ecological Monographs*, 77(4):503–525.

McClanahan, T. R., Ateweberhan, M., Omukoto, J., and Pearson, L. (2009). Recent seawater temperature histories, status, and predictions for Madagascar's coral reefs. *Marine Ecology Progress Series*, 380:117–128.

McClanahan, T. R., Ateweberhan, M., Sebastian, C. R., Graham, N., Wilson, S., Bruggemann, J. H., and Guillaume, M. M. (2007b). Predictability of coral bleaching from synoptic satellite and in situ temperature observations. *Coral Reefs*, 26(3):695–701.

McCullagh, P. (1980). Regression models for ordinal data. *Journal of the Royal Statistical Society: Series B (Methodological)*, 42(2):109–127.

Meekan, M. G., Carleton, J., McKinnon, A., Flynn, K., and Furnas, M. (2003). What determines the growth of tropical reef fish larvae in the plankton: food or temperature? *Marine Ecology Progress Series*, 256:193–204.

Mellin, C., Aaron MacNeil, M., Cheal, A. J., Emslie, M. J., and Julian Caley, M. (2016). Marine protected areas increase resilience among coral reef communities. *Ecology letters*, 19(6):629–637.

Mellor, G. L. and Yamada, T. (1974). A hierarchy of turbulence closure models for planetary boundary layers. *Journal of Atmospheric Sciences*, 31(7):1791–1806.

Middlebrook, R., Anthony, K. R., Hoegh-Guldberg, O., and Dove, S. (2010). Heating rate and symbiont productivity are key factors determining thermal stress in the reef-building coral Acropora formosa. *Journal of Experimental Biology*, 213(7):1026–1034.

Middlebrook, R., Hoegh-Guldberg, O., and Leggat, W. (2008). The effect of thermal history on the susceptibility of reef-building corals to thermal stress. *Journal of Experimental Biology*, 211(7):1050–1056.

Mofjeld, H. (1988). Depth dependence of bottom stress and quadratic drag coefficient for barotropic pressure-driven currents. *Journal of Physical Oceanography*, 18(11):1658–1669.

Molina, L., Pawlak, G., Wells, J., Monismith, S., and Merrifield, M. (2014). Diurnal cross-shore thermal exchange on a tropical forereef. *Journal of Geophysical Research: Oceans*, 119(9):6101–6120.

Monismith, S. G., Genin, A., Reidenbach, M. A., Yahel, G., and Koseff, J. R. (2006). Thermally driven exchanges between a coral reef and the adjoining ocean. *Journal of Physical Oceanography*, 36(7):1332–1347.

Monismith, S. G., Imberger, J., and Morison, M. L. (1990). Convective motions in the sidearm of a small reservoir. *Limnology and Oceanography*, 35(8):1676–1702.

Nittrouer, C. A. and Wright, L. D. (1994). Transport of particles across continental shelves. *Reviews of Geophysics*, 32(1):85–113.

Oliver, T. and Palumbi, S. (2011). Do fluctuating temperature environments elevate coral thermal tolerance? *Coral Reefs*, 30(2):429–440.

Oliver, T. A. and Palumbi, S. R. (2009). Distributions of stress-resistant coral symbionts match environmental patterns at local but not regional scales. *Marine Ecology Progress Series*, 378:93–103.

Orlanski, I. (1976). A simple boundary condition for unbounded hyperbolic flows. *Journal of Computational Physics*, 21(3):251–269.

Ozmidov, R. (1965). On the turbulent exchange in a stably stratified ocean. *Izv. Acad. Sci. USSR, Atmos. Oceanic Phys*, 1(8):853–860.

Palumbi, S. R., Barshis, D. J., Traylor-Knowles, N., and Bay, R. A. (2014). Mechanisms of reef coral resistance to future climate change. *Science*, 344(6186):895–898.

Paulson, C. A. and Simpson, J. J. (1977). Irradiance measurements in the upper ocean. *Journal of Physical Oceanography*, 7(6):952–956.

Perlin, A., Moum, J., and Klymak, J. (2005a). Response of the bottom boundary layer over a sloping shelf to variations in alongshore wind. *Journal of Geophysical Research: Oceans*, 110(C10).

Perlin, A., Moum, J., Klymak, J., Levine, M., Boyd, T., and Kosro, P. (2007). Organization of stratification, turbulence, and veering in bottom Ekman layers. *Journal of Geophysical Research: Oceans*, 112(C5).

Perlin, A., Moum, J. N., Klymak, J., Levine, M. D., Boyd, T., and Kosro, P. M. (2005b). A modified law-of-the-wall applied to oceanic bottom boundary layers. *Journal of Geophysical Research: Oceans*, 110(C10).

Pineda, J., Hare, J. A., and Sponaugle, S. (2007). Larval transport and dispersal in the coastal ocean and consequences for population connectivity. *Oceanography*, 20(3):22–39.

Pineda, J., Starczak, V., Tarrant, A., Blythe, J., Davis, K., Farrar, T., Berumen, M., and da Silva, J. C. (2013). Two spatial scales in a bleaching event: Corals from the mildest and the most extreme thermal environments escape mortality. *Limnology and Oceanography*, 58(5):1531–1545.

Pringle, J. M. (2001). Cross-shelf eddy heat transport in a wind-free coastal ocean undergoing winter time cooling. *Journal of Geophysical Research: Oceans*, 106(C2):2589–2604.

Reid, E. C., DeCarlo, T. M., Cohen, A. L., Wong, G. T., Lentz, S. J., Safaie, A., Hall, A., and Davis, K. A. (2019). Internal waves influence the thermal and nutrient environment on a shallow coral reef. *Limnology and Oceanography*, 64(5):1949–1965.

Riegl, B. and Piller, W. E. (2003). Possible refugia for reefs in times of environmental stress. *International Journal of Earth Sciences*, 92(4):520–531.

Rodi, W. (1987). Examples of calculation methods for flow and mixing in stratified fluids. *Journal of Geophysical Research: Oceans*, 92(C5):5305–5328.

Rogers, J. S., Monismith, S. G., Koweek, D. A., Torres, W. I., and Dunbar, R. B. (2016). Thermodynamics and hydrodynamics in an atoll reef system and their influence on coral cover. *Limnology and Oceanography*, 61(6):2191–2206.

Rosman, J. H., Hench, J. L., Koseff, J. R., and Monismith, S. G. (2008). Extracting Reynolds stresses from acoustic doppler current profiler measurements in wave-dominated environments. *Journal of Atmospheric and Oceanic Technology*, 25(2):286–306.

Roughgarden, J., Gaines, S., and Possingham, H. (1988). Recruitment dynamics in complex life cycles. *Science*, 241(4872):1460–1466.

Rowan, R. (2004). Thermal adaptation in reef coral symbionts. *Nature*, 430(7001):742–742.

Safaie, A., Pawlak, G., and Davis, K. (in prep.). Thermally-driven cross-shore exchange in steady alongshore currents. Manuscript in preparation.

Safaie, A., Silbiger, N. J., McClanahan, T. R., Pawlak, G., Barshis, D. J., Hench, J. L., Rogers, J. S., Williams, G. J., and Davis, K. A. (2018). High frequency temperature variability reduces the risk of coral bleaching. *Nature Communications*, 9(1):1–12.

Saffman, P. G. (1970). A model for inhomogeneous turbulent flow. *Proceedings of the Royal Society of London. A. Mathematical and Physical Sciences*, 317(1530):417–433.

Schabenberger, O. (1995). The use of ordinal response methodology in forestry. *Forest Science*, 41(2):321–336.

Schoepf, V., Stat, M., Falter, J. L., and McCulloch, M. T. (2015). Limits to the thermal tolerance of corals adapted to a highly fluctuating, naturally extreme temperature environment. *Scientific Reports*, 5(1):1–14.

Selig, E. R., Casey, K. S., and Bruno, J. F. (2012). Temperature-driven coral decline: the role of marine protected areas. *Global Change Biology*, 18(5):1561–1570.

Shaw, W. J. and Trowbridge, J. H. (2001). The direct estimation of near-bottom turbulent fluxes in the presence of energetic wave motions. *Journal of Atmospheric and Oceanic Technology*, 18(9):1540–1557.

Shchepetkin, A. F. and McWilliams, J. C. (2005). The regional oceanic modeling system (ROMS): a split-explicit, free-surface, topography-following-coordinate oceanic model. *Ocean Modelling*, 9(4):347–404.

Sheldon, K. S. and Dillon, M. E. (2016). Beyond the mean: biological impacts of cryptic temperature change. *Integrative and Comparative Biology*, 56(1):110–119.

Song, Y. and Haidvogel, D. (1994). A semi-implicit ocean circulation model using a generalized topography-following coordinate system. *Journal of Computational Physics*, 115(1):228–244.

Stips, A., Burchard, H., Bolding, K., and Eifler, W. (2002). Modelling of convective turbulence with a two-equation k-ϵ turbulence closure scheme. *Ocean Dynamics*, 52(4):153–168.

Sturman, J. J., Oldham, C. E., and Ivey, G. N. (1999). Steady convective exchange flows down slopes. *Aquatic Sciences*, 61(3):260–278.

Swain, T. D., Vega-Perkins, J. B., Oestreich, W. K., Triebold, C., DuBois, E., Henss, J., Baird, A., Siple, M., Backman, V., and Marcelino, L. (2016). Coral bleaching response index: a new tool to standardize and compare susceptibility to thermal bleaching. *Global Change Biology*, 22(7):2475–2488.

Team, R. C. (2017). R: a language and environment for statistical computing. R Foundation for Statistical Computing, Vienna. https. *www.R-project.org*.

Trowbridge, J. and Lentz, S. (1998). Dynamics of the bottom boundary layer on the northern California shelf. *Journal of Physical Oceanography*, 28(10):2075–2093.

Ulloa, H. N., Davis, K. A., Monismith, S. G., and Pawlak, G. (2018). Temporal variability in thermally driven cross-shore exchange: The role of semidiurnal tides. *Journal of Physical Oceanography*, 48(7):1513–1531.

Umlauf, L. and Burchard, H. (2003). A generic length-scale equation for geophysical turbulence models. *Journal of Marine Research*, 61(2):235–265.

Van Hooidonk, R., Maynard, J., Tamelander, J., Gove, J., Ahmadia, G., Raymundo, L., Williams, G., Heron, S. F., and Planes, S. (2016). Local-scale projections of coral reef futures and implications of the Paris Agreement. *Scientific Reports*, 6(1):1–8.

Warner, J. C., Sherwood, C. R., Arango, H. G., and Signell, R. P. (2005). Performance of four turbulence closure models implemented using a generic length scale method. *Ocean Modelling*, 8(1-2):81–113.

Warner, R. M. (1998). *Spectral analysis of time-series data*. Guilford Press.

Welander, P. (1957). Wind action on a shallow sea: some generalizations of Ekman's theory. *Tellus*, 9(1):45–52.

West, J. M. and Salm, R. V. (2003). Resistance and resilience to coral bleaching: implications for coral reef conservation and management. *Conservation Biology*, 17(4):956–967.

Williams, G. J., Knapp, I. S., Maragos, J. E., and Davy, S. K. (2010). Modeling patterns of coral bleaching at a remote Central Pacific atoll. *Marine Pollution Bulletin*, 60(9):1467–1476.

Williams, G. J., Sandin, S. A., Zgliczynski, B. J., Fox, M. D., Gove, J. M., Rogers, J. S., Furby, K. A., Hartmann, A. C., Caldwell, Z. R., Price, N. N., et al. (2018). Biophysical drivers of coral trophic depth zonation. *Marine Biology*, 165(4):60.

Winters, K. B., Lombard, P. N., Riley, J. J., and D'Asaro, E. A. (1995). Available potential energy and mixing in density-stratified fluids. *Journal of Fluid Mechanics*, 289:115–128.

Yee, S. H. and Barron, M. G. (2010). Predicting coral bleaching in response to environmental stressors using 8 years of global-scale data. *Environmental Monitoring and Assessment*, 161(1-4):423–438.

Yee, S. H., Santavy, D. L., and Barron, M. G. (2008). Comparing environmental influences on coral bleaching across and within species using clustered binomial regression. *Ecological Modelling*, 218(1-2):162–174.

Appendix A

Supplementary Information for Chapter 1

A.1 Supplementary Note 1: High-frequency Spectral Content

Power Spectral Density (PSD) estimates of the 118 temperature time series reveal that all had significant diurnal and semidiurnal spectral peaks, emphasizing the ubiquity of significant high-frequency variance throughout our data set (Supplementary Fig. A.1). The majority of time series also showed significant peaks corresponding to the shallow water terdiurnal and quarterdiurnal frequencies (99.2% and 92.4% of time series, respectively). Finally, 43 (30.5%) of the time series showed significant spectral peaks corresponding to long term, annual frequencies (1/90 – 1/540 cpd). Statistically significant spectral peaks are indicated in Supplementary Figure A.1 to illustrate the persistence of high frequency water temperature variability among many different types of coral reef environments. Regardless of oceanographic region or latitudinal gradient, there is a considerable amount of temperature

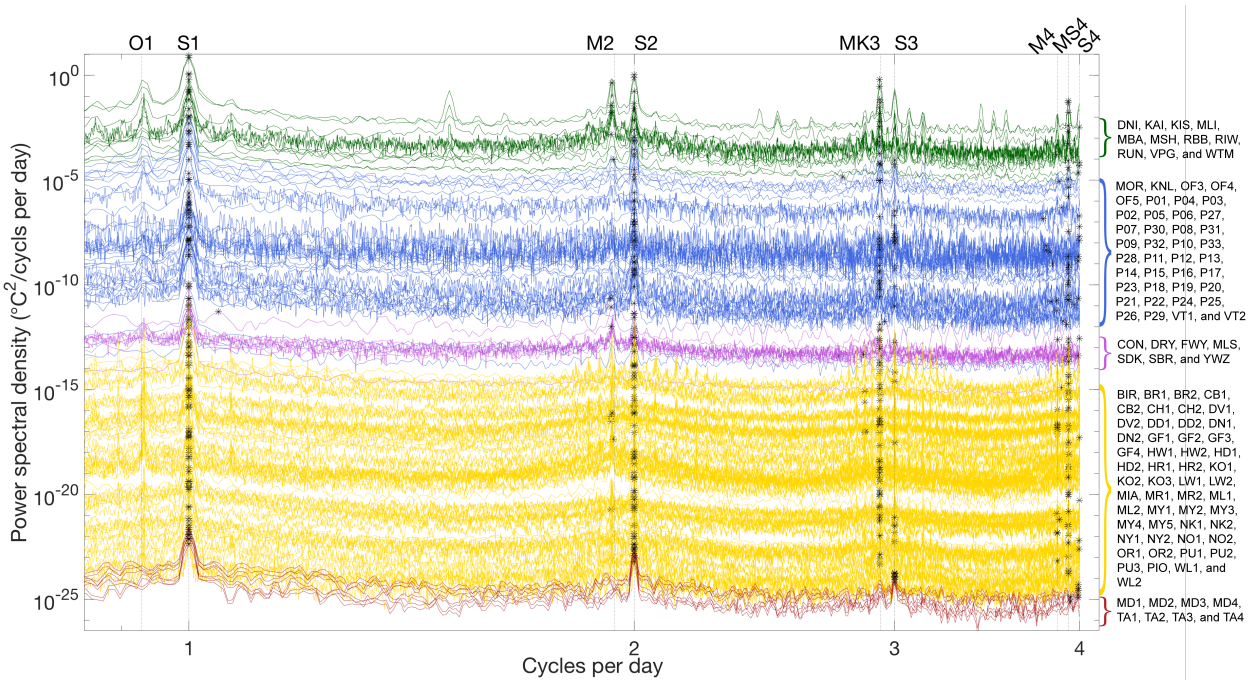

Figure A.1: **Power spectra at high-frequencies.** Power Spectral Density (PSD) estimates of water temperature from every time series, focused on the high frequency (0.727 to 4 cpd) part of the spectrum. PSD estimates are sequentially offset by 10-0.2 $°C^2$/cpd, and significant peaks are marked with an asterisk. The 3-letter abbreviations for each temperature time series are listed following their PSD estimates, and grouped by oceanographic region.

variability within diurnal and shorter periods that reefs are exposed to.

A.2 Supplementary Note 2: Seasonal Variation in Daily Temperature Range

The results of Kruskal-Wallis tests for 113 of 118 (96%) temperature records (all except MD1, MD2 from Abu Madafi, Saudi Arabia, and P13, P23, and P32 from Palmyra Atoll, United States), allow us to conclude that daily temperature range (DTR) values are significantly different in distribution across the four astronomical seasons ($p < 0.01$), where seasons were defined such that each season spanned 3 complete months, and austral and boreal summers were December through February and June through August, respectively. This seasonality

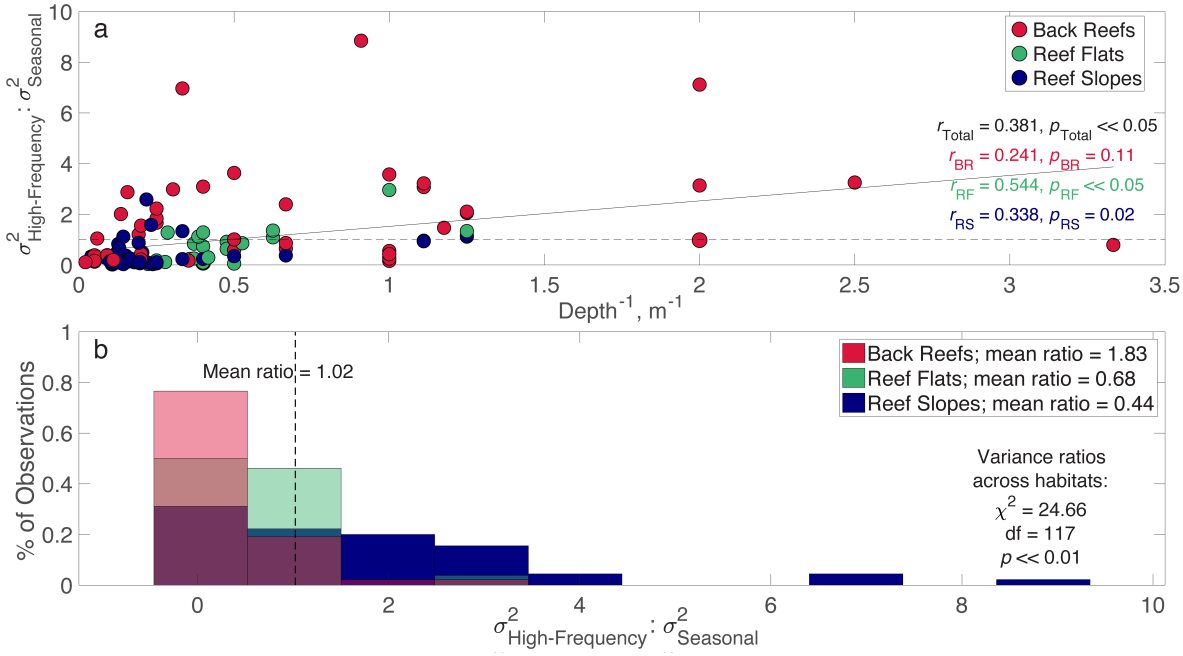

Figure A.2: **Ratios of high-frequency to seasonal variance by habitat.** For all temperature time series, high-frequency (1/33 to 1/6 h) and seasonal (1/7 to 1/84 d) variance were computed via integration of power spectral densities within these respective frequency bands. **a**) Variance ratios plotted against depth and colored by reef habitat, along with a linear regression line (solid black) and unity (dashed black); **b**) Histograms of the variance ratios are shown grouped by reef habitat, and the results of a Kruskal-Wallis test are indicated.

is illustrated for six representative time series as yearly composite averages in column (**b**) of Figure 1.2. The variable width of the pink patch in each yearly composite time series illustrates the variability of DTRs at these sites, while the red lines indicate the seasonally-averaged DTR. Maximum DTR values are most common during late spring to summer (boreal and austral) months (Supplementary Fig. A.3), when solar heating of the ocean surface is largest, with the average summer DTR 1.2-2.1 times as large as the average winter DTR.

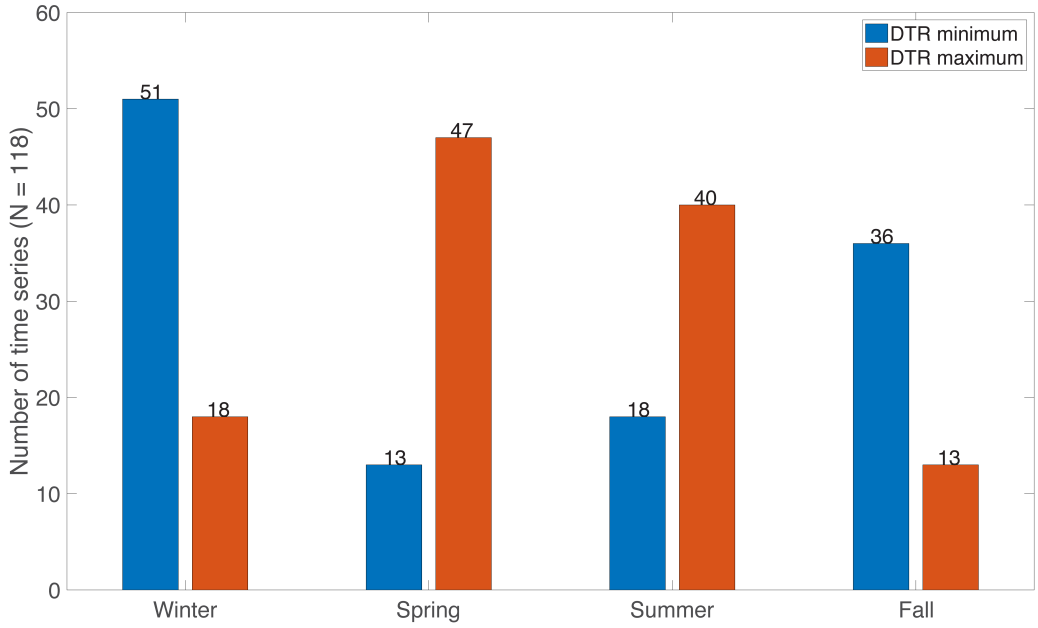

Figure A.3: **DTR extrema by season.** Orange bars: counts of time series with maximum DTR values in winter (18), spring (47), summer (40), and fall (13); blue bars: counts of time series with minimum DTR valuess in winter (51), spring (13), summer (18), and fall (36). Seasons were distinguished among northern and southern hemispheres, and arranged such that austral and boreal summers were December through February and June through August, respectively.

Interaction Term	**Interaction Coefficient**	**Coefficient for:**		**AIC_C**	**ΔAIC_C**
		DHW_{30}	**DTR_{30}**		
Depth x DHW_{30}	1.78	2.11	-2.31	143.57	-0.18
Depth x DTR_{30}	2.69	1.77	-1.72	142.74	-1.01
Depth x $ROTC_{SS}$	-0.09	0.95	-2.63	146.32	2.57
Depth x MMM	-0.11	0.96	-2.6	146.31	2.56
MMM x DHW_{30}	0.8	2.04	-2.85	144.41	0.66
MMM x TT	-0.4	0.83	-2.89	145	1.25
MMM x Acute1	0.32	1.14	-2.8	145.3	1.55
MMM x $ROTC_{SS}$	-0.01	0.97	-2.67	146.35	2.60
Acute1 x DHW_{30}	-3.94	5.99	-3.06	143.37	-0.38
TT x DHW_{30}	-0.55	2.1	-2.51	144.27	0.52
$ROTC_{SS}$ x DTR_{30}	-0.15	0.97	-2.63	146.32	2.57

Table A.1: **Nonlinear Ordinal Logistic Regression Models.** *In situ* variable interaction terms added to the highest-ranked OLR model (Fig. 1.3b), coefficient parameter estimates for these interaction terms, the corresponding DHW_{30} and DTR_{30} coefficient parameter estimates, and AIC_C and ΔAIC_C values of the resulting models.

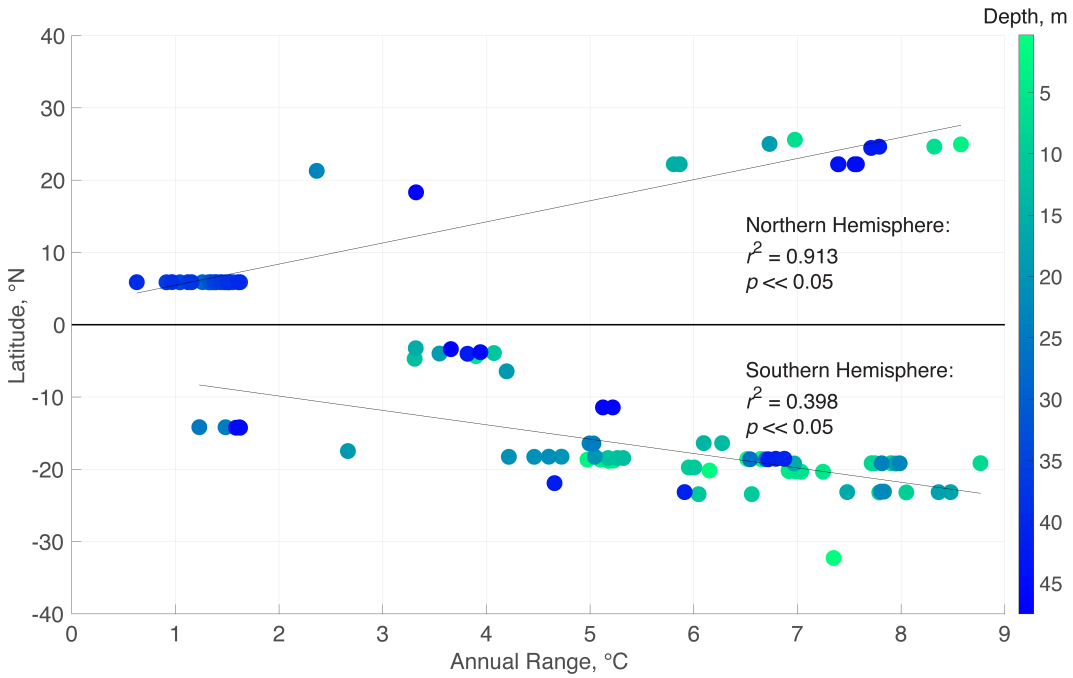

Figure A.4: **Latitude vs annual temperature ranges.** Latitudinal gradient in annual temperature ranges for every time series, arranged by hemisphere and colored according to in situ logger depth (m). Linear correlations and regression lines are shown for each hemisphere.

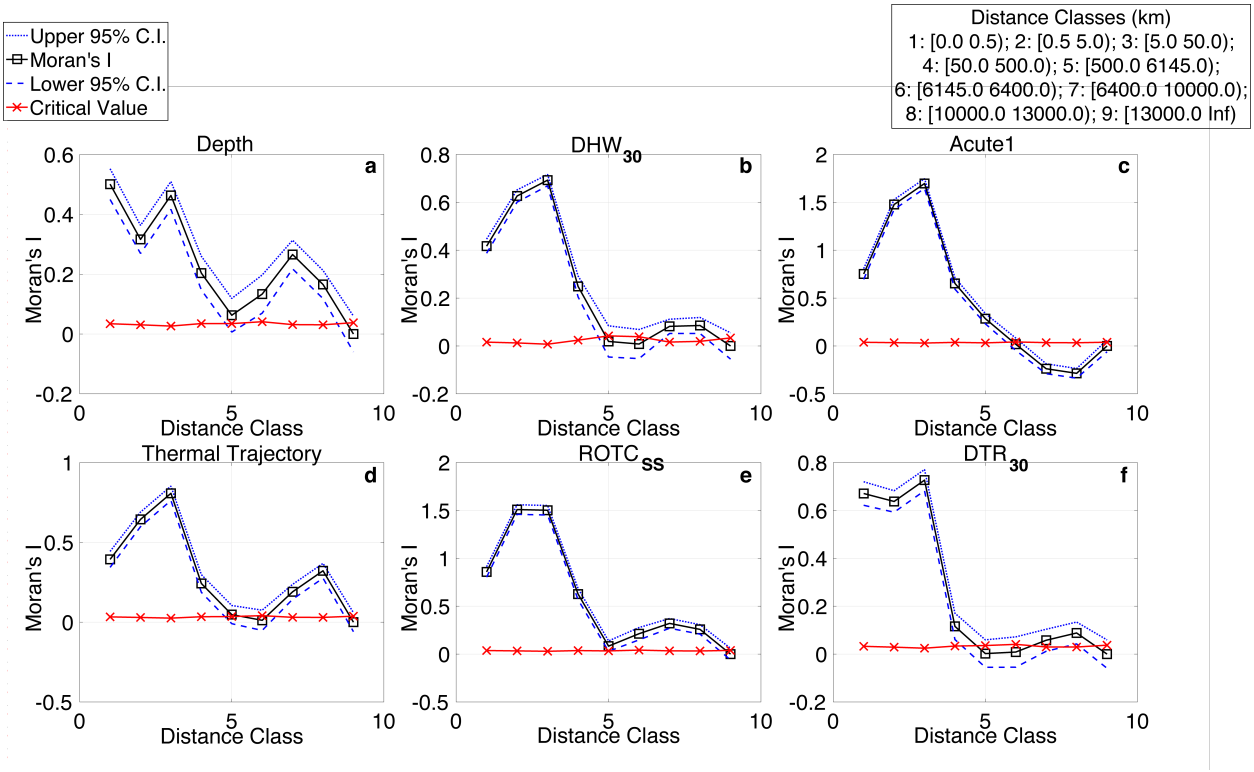

Figure A.5: **Moran's I Correlograms.** For the in situ covariates in the highest-ranked OLR model, Moran's I was computed using distance classes (km) of 1: [0, 0.5); 2: [0.5, 5.0); 3: [5.0, 50.0); 4: [50.0, 500.0); 5: [500.0, 6145.0); 6: [6145.0, 6400.0); 7: [6400.0, 10000.0); 8: [10000.0, 13000.0); 9: [13000.0, ∞). 95% confidence intervals are shown, and critical values for Moran's I were computed using a correction for small sample sizes. Covariates in the highest-ranked in situ model include **a**) Depth, **b**) DHW_{30}, **c**) Acute1, **d**) Thermal Trajectory, **e**) $ROTC_{SS}$, and **f**) DTR_{30}.

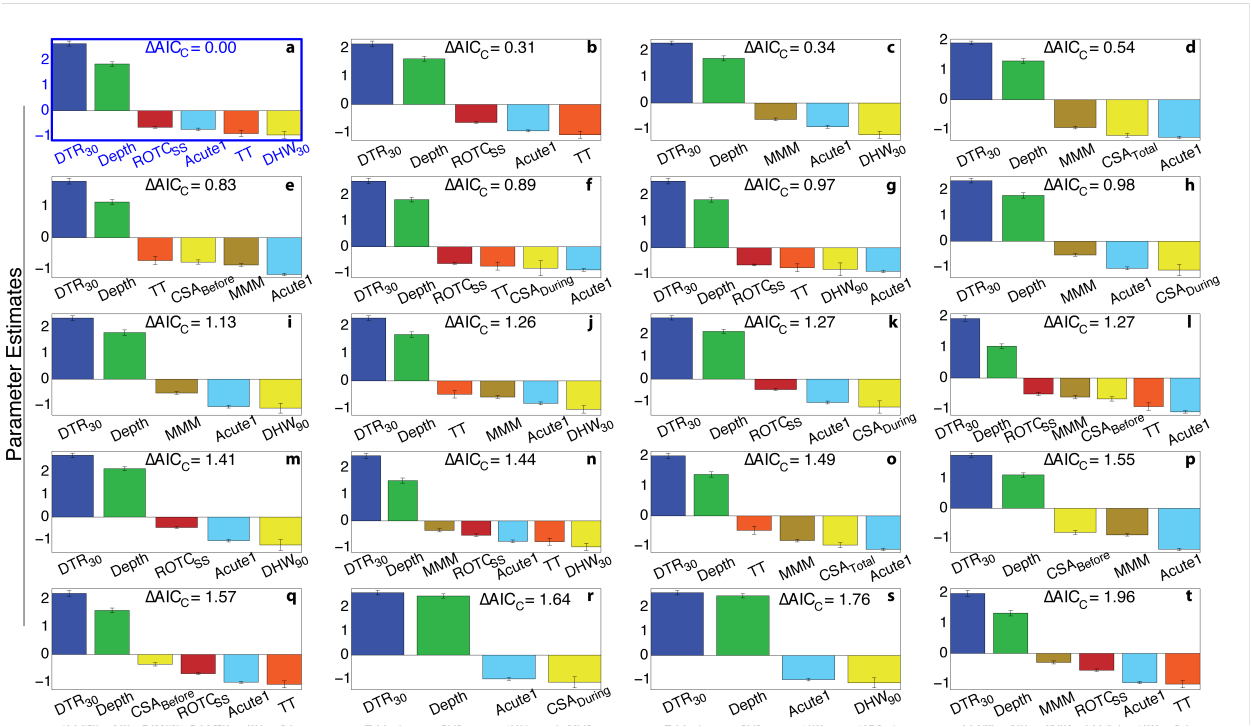

Figure A.6: **All in situ-based logit models within $\Delta\text{AIC}_\text{C} \leq 2$ of the highest ranked model.** Standardized model coefficients (y-axis) and their corresponding explanatory variable (x-axis), with jackknifed standard error bars and $\Delta\text{AIC}_\text{C}$ values indicated. (**a**) The global best model with $\Delta\text{AIC}_\text{C} = 0$; (**b-t**) all models within $\Delta\text{AIC}_\text{C} \leq 2$, which are statistically indistinguishable from (**a**).

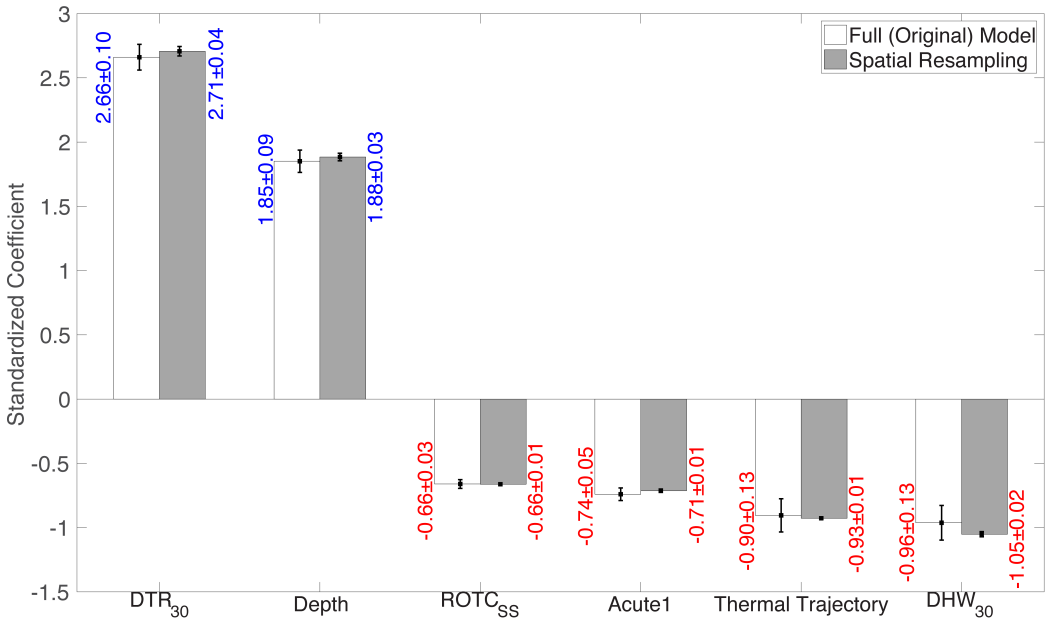

Figure A.7: **Highest-ranked in situ model results after spatial resampling.** Standardized coefficients for the highest-ranked model parameter estimates fit to the entire data set are shown in white (± s.e.), while the average of the resampled parameter estimates for the same covariates are shown in grey (± s.e.). The modified jackknife resampling scheme involved grouping sites within 10 km of each other and removing each of these proximity groups incrementally before fitting OLR models to the remaining data.

Appendix B

Time Series Metadata

Table B.1: **Description and metadata of temperature time series incorporated in this study.** Ocean regions are defined as: WIO: Western Indian Ocean; PO: Pacific Ocean; CS: Caribbean Sea; GBR: Great Barrier Reef; RS: Red Sea. Habitat categories defined as: BR: backreefs, lagoons; RF = reef flats, wave-protected reef platforms; RS = reef crests, reef slopes, and everything seaward.

Region	Location	Abbr.	Duration	Latitude (°N)	Longitude (°E)	Logger Depth (m)	Logger Habitat	Logger Accuracy (°C)	Data Source	Related Publication
WIO	Diani, Kenya	DNI	01-Feb-2001 09-Mar-2008	-4.3528	39.5781	0.5	BR	±0.35	Tim McClanahan	McClanahan and Maina (2003)
WIO	Kanamai, Kenya	KAI	23-Feb-2001 17-Nov-2009	-3.9207	39.7868	0.4	BR	± 0.35	Tim McClanahan	McClanahan and Maina (2003)
WIO	Kisite, Kenya	KIS	18-Jul-2003 31-Dec-2007	-4.709	39.37033333	2	BR	± 0.35	Tim McClanahan	McClanahan et al. (2007b)
WIO	Malindi, Kenya	MLI	27-Feb-1995 30-Nov-2011	-3.255666667	40.14066667	1.5	BR	±0.35	Tim McClanahan	McClanahan et al. (2007b)
WIO	Mombasa, Kenya	MBA	22-Aug-1996 09-Dec-2010	-3.988333333	39.75033333	1	BR	±0.35	Tim McClanahan	McClanahan and Maina (2003)
WIO	Mshingwi Island, Tanzania	MSH	08-Mar-2009 11-Aug-2011	-6.445718397	38.95672173	1	RS	?	Tim McClanahan	
WIO	Rano Be Beantsisy, Madagascar	RBB	27-Mar-2007 21-Sep-2008	-23.15708333	43.57925	1	BR	?	Tim McClanahan	
WIO	Ras Iwatine, Kenya	RIW	30-Oct-2002 12-Oct-2011	-4.0195	39.72616667	1.5	BR	±0.35	Tim McClanahan	McClanahan et al. (2007b)
WIO	Pointe des Galets, Reunion Island, France	RUN	26-Nov-1997 09-May-2004	-21.9167	55.2833	3	RS	±0.5	Tim McClanahan	Conand et al. (2008)
WIO	Vipingo, Kenya	VPG	29-Jan-2001 07-Dec-2010	-3.799333333	39.83616667	0.5	BR	±0.35	Tim McClanahan	McClanahan and Maina (2003)
WIO	Watamu, Kenya	WTM	09-Aug-2002 30-Nov-2011	-3.3765	39.98883333	1	BR	±0.35	Tim McClanahan	McClanahan et al. (2007b)
PO	Moorea, French Polynesia	MOR	11-Jan-2012 28-Jul-2012	-17.47799833	-149.8391317	0.3	BR	±0.002	James Hench	
PO	Kilo Nalu, Hawaii	KNL	30-Mar-2007 03-Jan-2011	21.288	-157.865	12	RS	?	Geno Pawlak	
PO	Ofu Island Pool 300, American Samoa	OF3	03-Jan-2004 11-Sep-2011	-14.18287	-169.65951	0.8	BR	±0.2	National Park of American Samoa	Oliver and Palumbi (2011, 2009)

Continued on next page

Table B.1 – continued from previous page

Region	Location	Abbr.	Duration	Latitude (°N)	Longitude (°E)	Logger Depth (m)	Logger Habitat	Logger Accuracy (°C)	Data Source	Related Publication
PO	Ofu Island Pool 400, American Samoa	OF4	18-Dec-2003 01-Sep-2011	-14.17888	-169.65416	1.5	BR	±0.2	National Park of American Samoa	Oliver and Palumbi (2011, 2009)
PO	Ofu Island Pool 500, American Samoa	OF5	24-Aug-2002 12-Feb-2010	-14.17325	-169.6479667	0.85	BR	±0.2	National Park of American Samoa	Oliver and Palumbi (2011, 2009)
PO	Palmyra Atoll, US	P01	03-Oct-2012 14-Jul-2014	5.879866667	-162.1013	2	BR	±0.2	Justin Rogers, Gareth Williams	Williams et al. (2010); Rogers et al. (2016)
PO	Palmyra Atoll, US	P02	30-Sep-2011 13-Jul-2014	5.878238333	-162.1046883	7.4	BR	±0.2	Justin Rogers, Gareth Williams	Williams et al. (2010); Rogers et al. (2016)
PO	Palmyra Atoll, US	P03	16-Mar-2002 30-Jun-2014	5.870366667	-162.0449667	2	BR	±0.2	Justin Rogers, Gareth Williams	Williams et al. (2010); Rogers et al. (2016)
PO	Palmyra Atoll, US	P04	02-Apr-2011 01-Jun-2014	5.890166667	-162.1256667	5.2	BR	±0.2	Justin Rogers, Gareth Williams	Williams et al. (2010); Rogers et al. (2016)
PO	Palmyra Atoll, US	P05	02-Apr-2004 13-Jul-2014	5.887533333	-162.08705	2.833333333	BR	±0.2	Justin Rogers, Gareth Williams	Williams et al. (2010); Rogers et al. (2016)
PO	Palmyra Atoll, US	P06	03-Oct-2012 15-Jun-2014	5.88395	-162.0681333	1.5	RS	±0.2	Justin Rogers, Gareth Williams	Williams et al. (2010); Rogers et al. (2016)
PO	Palmyra Atoll, US	P07	02-Apr-2004 11-Jul-2014	5.86629	-162.11362	20	BR	±0.2	Justin Rogers, Gareth Williams	Williams et al. (2010); Rogers et al. (2016)
PO	Palmyra Atoll, US	P08	03-Aug-2008 11-Jul-2014	5.869528333	-162.0751667	20	RS	±0.2	Justin Rogers, Gareth Williams	Williams et al. (2010); Rogers et al. (2016)
PO	Palmyra Atoll, US	P09	23-Jul-2008 10-Jul-2014	5.89738	-162.07835	20	BR	±0.2	Justin Rogers, Gareth Williams	Williams et al. (2010); Rogers et al. (2016)
PO	Palmyra Atoll, US	P10	01-Aug-2008 10-Jul-2014	5.89702	-162.12836	20	BR	±0.2	Justin Rogers, Gareth Williams	Williams et al. (2010); Rogers et al. (2016)
PO	Palmyra Atoll, US	P11	03-Oct-2012 28-Aug-2013	5.877166667	-162.119	4	BR	±0.2	Justin Rogers, Gareth Williams	Williams et al. (2010); Rogers et al. (2016)
PO	Palmyra Atoll, US	P12	05-Jun-2005 10-Jun-2014	5.881333333	-162.0420167	2.5	BR	±0.002	Justin Rogers, Gareth Williams	Williams et al. (2010); Rogers et al. (2016)
PO	Palmyra Atoll, US	P13	10-Sep-2013 14-Jul-2014	5.892883333	-162.0772167	0.5	BR	±0.2	Justin Rogers, Gareth Williams	Williams et al. (2010); Rogers et al. (2016)
PO	Palmyra Atoll, US	P14	03-Oct-2012 12-Jul-2014	5.871666667	-162.1131667	6.4	BR	±0.2	Justin Rogers, Gareth Williams	Williams et al. (2010); Rogers et al. (2016)
PO	Palmyra Atoll, US	P15	01-Apr-2004 14-Jul-2014	5.8715	-162.107	3.3	BR	±0.2	Justin Rogers, Gareth Williams	Williams et al. (2010); Rogers et al. (2016)

Continued on next page

Table B.1 – continued from previous page

Region	Location	Abbr.	Duration	Latitude (°N)	Longitude (°E)	Logger Depth (m)	Logger Habitat	Logger Accuracy (°C)	Data Source	Related Publication
PO	Palmyra Atoll, US	P16	29-May-2003 14-Jul-2014	5.871	-162.1103333	5	BR	±0.2	Justin Rogers, Gareth Williams	Williams et al. (2010); Rogers et al. (2016)
PO	Palmyra Atoll, US	P17	16-Oct-2008 29-May-2014	5.869333333	-162.1108333	4	BR	±0.2	Justin Rogers, Gareth Williams	Williams et al. (2010); Rogers et al. (2016)
PO	Palmyra Atoll, US	P18	29-Sep-2000 14-Jul-2014	5.886183333	-162.1262833	5.2	RS	±0.002	Justin Rogers, Gareth Williams	Williams et al. (2010); Rogers et al. (2016)
PO	Palmyra Atoll, US	P19	03-Oct-2012 18-Nov-2013	5.888566667	-162.1243333	3	RS	±0.2	Justin Rogers, Gareth Williams	Williams et al. (2010); Rogers et al. (2016)
PO	Palmyra Atoll, US	P20	03-Oct-2012 14-Jul-2014	5.886483333	-162.12015	4.6	RS	±0.2	Justin Rogers, Gareth Williams	Williams et al. (2010); Rogers et al. (2016)
PO	Palmyra Atoll, US	P21	03-Oct-2012 14-Jul-2014	5.882883333	-162.12195	4.3	RS	±0.2	Justin Rogers, Gareth Williams	Williams et al. (2010); Rogers et al. (2016)
PO	Palmyra Atoll, US	P22	03-Oct-2012 18-Jun-2013	5.873733333	-162.1103333	3	BR	±0.2	Justin Rogers, Gareth Williams	Williams et al. (2010); Rogers et al. (2016)
PO	Palmyra Atoll, US	P23	05-Sep-2013 15-Jul-2014	5.874566667	-162.1200667	17	BR	±0.2	Justin Rogers, Gareth Williams	Williams et al. (2010); Rogers et al. (2016)
PO	Palmyra Atoll, US	P24	03-Oct-2012 25-Jun-2014	5.892333333	-162.1175	4	BR	±0.2	Justin Rogers, Gareth Williams	Williams et al. (2010); Rogers et al. (2016)
PO	Palmyra Atoll, US	P25	03-Oct-2012 28-Aug-2013	5.87095	-162.0493333	1.1	BR	±0.2	Justin Rogers, Gareth Williams	Williams et al. (2010); Rogers et al. (2016)
PO	Palmyra Atoll, US	P26	03-Oct-2012 13-Jul-2014	5.884566667	-162.0899833	47.5	BR	±0.2	Justin Rogers, Gareth Williams	Williams et al. (2010); Rogers et al. (2016)
PO	Palmyra Atoll, US	P27	24-Mar-2006 27-Feb-2008	5.88276	-162.06182	24.99	RS	±0.2	Justin Rogers, Gareth Williams	Williams et al. (2010); Rogers et al. (2016)
PO	Palmyra Atoll, US	P28	25-Mar-2006 02-Mar-2008	5.86422	-162.03066	10.97	BR	±0.2	Justin Rogers, Gareth Williams	Williams et al. (2010); Rogers et al. (2016)
PO	Palmyra Atoll, US	P29	30-Mar-2004 01-Apr-2008	5.88468	-162.1028	1	BR	±0.2	Justin Rogers, Gareth Williams	Williams et al. (2010); Rogers et al. (2016)
PO	Palmyra Atoll, US	P30	02-Apr-2004 11-Jul-2014	5.86769	-162.11362	5	BR	±0.2	Justin Rogers, Gareth Williams	Williams et al. (2010); Rogers et al. (2016)
PO	Palmyra Atoll, US	P31	03-Aug-2008 11-Jul-2014	5.870928333	-162.0751667	5	RS	±0.2	Justin Rogers, Gareth Williams	Williams et al. (2010); Rogers et al. (2016)
PO	Palmyra Atoll, US	P32	23-Jul-2008 10-Jul-2014	5.89598	-162.07835	5	BR	±0.2	Justin Rogers, Gareth Williams	Williams et al. (2010); Rogers et al. (2016)
PO	Palmyra Atoll, US	P33	01-Aug-2008 10-Jul-2014	5.89502	-162.12836	5	BR	±0.2	Justin Rogers, Gareth Williams	Williams et al. (2010); Rogers et al. (2016)

Continued on next page

Table B.1 – continued from previous page

Region	Location	Abbr.	Duration	Latitude (°N)	Longitude (°E)	Logger Depth (m)	Logger Habitat	Logger Accuracy (°C)	Data Source	Related Publication
PO	Vatia Bay, American Samoa	VT1	02-Dec-2003 21-Dec-2010	-14.24793	-170.66983	2	RS	±0.2	National Park of American Samoa	
PO	Vatia Bay, American Samoa	VT2	13-Nov-2003 21-Dec-2010	-14.24787	-170.66988	10	RS	±0.2	National Park of American Samoa	
CS	Conch Reef, Florida Keys, US	CON	21-Jun-2005 01-Jun-2006	24.95	-80.455	8	RS	±0.002	Kristen Davis, Stephen Monismith	Davis and Monismith (2011)
CS	Dry Tortugas, Flordia Keys, US	DRY	09-Dec-1992 21-Sep-2005	24.638	-82.862	2	RF	±0.08, ±0.002 or ±0.005	NDBC	Manzello et al. (2007)
CS	Fowey Rocks, Florida Keys, US	FWY	01-Jan-2003 31-Dec-2007	25.59	-80.097	1	RF	±0.08, ±0.002, or ±0.005	NDBC	Manzello et al. (2007)
CS	Molasses Reef, Florida Keys, US	MLS	27-Jul-1992 31-Dec-2007	25.012	-80.376	2.7	RF	±0.08, ±0.002, or ±0.005	NDBC	Manzello et al. (2007)
CS	Sand Key, Florida Keys, US	SDK	01-Jan-2003 20-Sep-2005	24.456	-81.877	1	BR	±0.08, ±0.002, or ±0.005	NDBC	Manzello et al. (2007)
CS	Sombrero Reef, Florida Keys, US	SBR	01-Jan-2003 31-Dec-2007	24.627	-81.11	1	BR	±0.08, ±0.002, or ±0.005	NDBC	Manzello et al. (2007)
CS	Yawzi Point, St. John, USVI	YWZ	01-Aug-2005 22-Jul-2013	18.3152	-64.725	9	BR	±0.2	Peter Edmunds	Edmunds (2013)
GBR	Bird Island, Australia	BIR	14-Feb-2013 04-Feb-2016	-32.27683333	115.6867333	2.5	RF	±0.2	AIMS	Australian Institute of Marine Science (AIMS). (2017a)
GBR	Border Island, Australia	BR1	24-Mar-2011 18-Jan-2015	-20.18189	149.03772	9.3	RS	±0.8	AIMS	Australian Institute of Marine Science (AIMS). (2017b)
GBR	Border Island, Australia	BR2	20-Apr-2013 18-Jan-2015	-20.17097	149.03194	1.6	RF	±0.8	AIMS	Australian Institute of Marine Science (AIMS). (2017b)
GBR	Cattle Bay, Australia	CB1	30-Mar-1993 04-Jul-2010	-18.571817	146.482983	6.5	RS	±0.8	AIMS	Australian Institute of Marine Science (AIMS). (2017c)
GBR	Cattle Bay, Australia	CB2	11-Feb-1993 04-Jul-2010	-18.57185	146.483333	3.5	RF	±0.8	AIMS	Australian Institute of Marine Science (AIMS). (2017c)

Continued on next page

Table B.1 – continued from previous page

Region	Location	Abbr.	Duration	Latitude (°N)	Longitude (°E)	Logger Depth (m)	Logger Habitat	Logger Accuracy (°C)	Data Source	Related Publication
GBR	Chicken Reef, Australia	CH1	27-Apr-1996 04-May-2015	-18.65337	147.71988	2.7	RF	±0.8	AIMS	Australian Institute of Marine Science (AIMS). (2017d)
GBR	Chicken Reef, Australia	CH2	27-Apr-1996 04-May-2015	-18.65213	147.7217	7.7	RS	±0.8	AIMS	Australian Institute of Marine Science (AIMS). (2017d)
GBR	Davies Reef, Australia	DV1	18-Oct-1991 21-Jun-2016	-18.83162	147.6345	4	RF	±0.1	AIMS	Australian Institute of Marine Science (AIMS). (2017e)
GBR	Davies Reef, Australia	DV2	02-May-1996 02-May-2015	-18.806	147.66862	8.4	RS	±0.8	AIMS	Australian Institute of Marine Science (AIMS). (2017e)
GBR	Daydream Island, Australia	DD1	26-Jun-1996 07-Mar-2015	-20.25575	148.81215	7.2	RS	±0.8	AIMS	Australian Institute of Marine Science (AIMS). (2017f)
GBR	Daydream Island, Australia	DD2	26-Jun-1996 07-May-2014	-20.25575	148.81215	3.6	RF	±0.8	AIMS	Australian Institute of Marine Science (AIMS). (2017f)
GBR	Dent Island, Australia	DN1	18-Dec-2005 03-Jul-2013	-20.34498	148.93822	4.5	RF	±0.8	AIMS	Australian Institute of Marine Science (AIMS). (2017g)
GBR	Dent Island, Australia	DN2	18-Dec-2005 11-Jul-2015	-20.34498	148.93822	4.2	RS	±0.8	AIMS	Australian Institute of Marine Science (AIMS). (2017g)
GBR	Geoffrey Bay, Australia	GF1	09-Mar-1993 01-Nov-2012	-19.15483	146.86923	7	RS	±0.8	AIMS	Australian Institute of Marine Science (AIMS). (2017h)
GBR	Geoffrey Bay, Australia	GF2	16-Feb-1995 27-Jun-1996	-19.155	146.865	4	RS	±0.8	AIMS	Australian Institute of Marine Science (AIMS). (2017h)
GBR	Geoffrey Bay, Australia	GF3	04-Jul-2010 12-Apr-2016	-19.15495	146.868483	2.5	RS	±0.8	AIMS	Australian Institute of Marine Science (AIMS). (2017h)
GBR	Geoffrey Bay, Australia	GF4	18-Dec-1992 29-Sep-2011	-19.15493	146.86447	2.1	RF	±0.8	AIMS	Australian Institute of Marine Science (AIMS). (2017h)

Continued on next page

Table B.1 – continued from previous page

Region	Location	Abbr.	Duration	Latitude (°N)	Longitude (°E)	Logger Depth (m)	Logger Habitat	Logger Accuracy (°C)	Data Source	Related Publication
GBR	Halfway Island, Australia	HW1	07-Dec-1995 11-Aug-2013	-23.20046	150.97062	2.4	RF	±0.8	AIMS	Australian Institute of Marine Science (AIMS). (2017i)
GBR	Halfway Island, Australia	HW2	07-Dec-1995 11-Aug-2013	-23.20148	150.9701	5.6	RS	±0.8	AIMS	Australian Institute of Marine Science (AIMS). (2017i)
GBR	Hardy Reef, Australia	HD1	25-Dec-2003 21-Jun-2016	-19.745928	149.182583	9	RS	±0.1	AIMS	Australian Institute of Marine Science (AIMS). (2017j)
GBR	Hardy Reef, Australia	HD2	14-Jun-1989 15-Sep-2010	-19.745928	149.182583	2.5	RF	±0.1	AIMS	Australian Institute of Marine Science (AIMS). (2017j)
GBR	Heron Island, Australia	HR1	24-Nov-1995 19-Mar-2012	-23.43843	151.91818	1	RF	±0.8	AIMS	Australian Institute of Marine Science (AIMS). (2017k)
GBR	Heron Island, Australia	HR2	24-Nov-1995 30-Mar-2012	-23.443536	151.908119	7.9	RS	±0.8	AIMS	Australian Institute of Marine Science (AIMS). (2017k)
GBR	Kelso Reef, Australia	KO1	10-Jun-1996 11-May-2015	-18.4448	146.99328	2.1	RF	±0.8	AIMS	Australian Institute of Marine Science (AIMS). (2017l)
GBR	Kelso Reef, Australia	KO2	23-Jul-1996 06-Jun-2015	-18.44701	146.98907	18.5	RS	±0.8	AIMS	Australian Institute of Marine Science (AIMS). (2017l)
GBR	Kelso Reef, Australia	KO3	04-Jul-1995 06-Jun-2015	-18.44432	146.99333	6.6	RS	±0.8	AIMS	Australian Institute of Marine Science (AIMS). (2017l)
GBR	Low Isles, Australia	LW1	30-Mar-1996 01-Aug-2011	-16.383361	145.562481	4.9	RS	±0.8	AIMS	Australian Institute of Marine Science (AIMS). (2017m)
GBR	Low Isles, Australia	LW2	30-Mar-1996 02-Mar-2015	-16.383269	145.562231	1.6	RF	±0.8	AIMS	Australian Institute of Marine Science (AIMS). (2017m)
GBR	Miall, Australia	MIA	27-Apr-2010 02-Mar-2011	-23.15483	150.903625	2.8	RF	±0.8	AIMS	Australian Institute of Marine Science (AIMS). (2017n)

Continued on next page

Table B.1 – continued from previous page

Region	Location	Abbr.	Duration	Latitude (°N)	Longitude (°E)	Logger Depth (m)	Logger Habitat	Logger Accuracy (°C)	Data Source	Related Publication
GBR	Middle Reef, Australia	MR1	17-May-2009 26-Mar-2011	-19.1945	146.8102	4.5	RS	±0.8	AIMS	Australian Institute of Marine Science (AIMS). (2017p)
GBR	Middle Reef, Australia	MR2	25-Jan-1996 01-Nov-2012	-19.20112	146.8209	7	RS	±0.8	AIMS	Australian Institute of Marine Science (AIMS). (2017p)
GBR	Middle Island, Australia	ML1	07-Dec-1995 15-Jul-1997	-23.16333	150.92167	4	RF	?	AIMS	Australian Institute of Marine Science (AIMS). (2017o)
GBR	Middle Island, Australia	ML2	18-Jul-1996 15-Jul-1997	-23.165	150.92333	4	RS	?	AIMS	Australian Institute of Marine Science (AIMS). (2017o)
GBR	Myrmidon Reef, Australia	MY1	13-Apr-1995 16-Aug-2012	-18.258945	147.38118	2.5	RF	±0.1	AIMS	Australian Institute of Marine Science (AIMS). (2017q)
GBR	Myrmidon Reef, Australia	MY2	13-Apr-1995 04-Jun-2015	-18.25702	147.38116	2.5	RS	±0.1	AIMS	Australian Institute of Marine Science (AIMS). (2017q)
GBR	Myrmidon Reef, Australia	MY3	02-Nov-1987 01-Feb-2011	-18.274247	147.381736	7	RS	±0.1	AIMS	Australian Institute of Marine Science (AIMS). (2017q)
GBR	Myrmidon Reef, Australia	MY4	02-Nov-1987 01-Feb-2011	-18.274247	147.381736	5	RS	±0.1	AIMS	Australian Institute of Marine Science (AIMS). (2017q)
GBR	Myrmidon Reef, Australia	MY5	13-Apr-1995 24-May-2013	-18.25673	147.38104	20.1	RS	±0.8	AIMS	Australian Institute of Marine Science (AIMS). (2017q)
GBR	North Keppel Island, Australia	NK1	27-Apr-2008 13-May-2015	-23.08645	150.905183	7.3	RS	±0.8	AIMS	Australian Institute of Marine Science (AIMS). (2017r)
GBR	North Keppel Island, Australia	NK2	28-Apr-2008 13-May-2015	-23.08645	150.905183	5.1	RF	±0.8	AIMS	Australian Institute of Marine Science (AIMS). (2017r)
GBR	Nelly Bay, Australia	NY1	25-Jan-1996 01-Nov-2012	-19.17217	146.84843	5.1	RS	±0.8	AIMS	Australian Institute of Marine Science (AIMS). (2017s)

Continued on next page

Table B.1 – continued from previous page

Region	Location	Abbr.	Duration	Latitude (°N)	Longitude (°E)	Logger Depth (m)	Logger Habitat	Logger Accuracy (°C)	Data Source	Related Publication
GBR	Nelly Bay, Australia	NY2	25-Jan-1996 01-Nov-2012	-19.1715	146.8475	2.4	RF	±0.8	AIMS	Australian Institute of Marine Science (AIMS). (2017s)
GBR	Norman Reef, Australia	NO1	25-Mar-1996 05-Dec-2008	-16.425	145.99333	0.8	RF	±0.8	AIMS	Australian Institute of Marine Science (AIMS). (2017t)
GBR	Norman Reef, Australia	NO2	26-Mar-1996 05-Dec-2008	-16.42667	145.995	8.1	RS	±0.8	AIMS	Australian Institute of Marine Science (AIMS). (2017t)
GBR	Orpheus Island, Australia	OR1	09-Dec-2002 02-Sep-2010	-18.612808	146.483094	1.9	RF	±0.002	AIMS	Australian Institute of Marine Science (AIMS). (2017u)
GBR	Orpheus Island, Australia	OR2	09-Dec-2002 02-Sep-2010	-18.612808	146.483094	6	RS	±0.002	AIMS	Australian Institute of Marine Science (AIMS). (2017u)
GBR	Pelorus Island, Australia	PU1	04-Aug-1993 16-Jun-2015	-18.54635	146.48803	2.6	RF	±0.8	AIMS	Australian Institute of Marine Science (AIMS). (2017v)
GBR	Pelorus Island, Australia	PU2	07-Aug-1993 29-Sep-2015	-18.54628	146.48752	5.1	RS	±0.8	AIMS	Australian Institute of Marine Science (AIMS). (2017v)
GBR	Pelorus Island, Australia	PU3	04-Aug-1993 16-Jun-2015	-18.54635	146.48803	2.6	RF	±0.8	AIMS	Australian Institute of Marine Science (AIMS). (2017v)
GBR	Pioneer Bay, Australia	PIO	17-Jul-1994 10-Sep-2010	-18.61158	146.48388	7.7	RS	±0.8	AIMS	Australian Institute of Marine Science (AIMS). (2017w)
GBR	Wallace Islet, Australia,	WL1	05-Dec-1997 18-Nov-2012	-11.44133	143.03355	2.5	RF	±0.8	AIMS	Australian Institute of Marine Science (AIMS). (2017x)
GBR	Wallace Islet, Australia,	WL2	21-Nov-1996 23-Oct-2013	-11.44087	143.03362	7.7	RS	±0.8	AIMS	Australian Institute of Marine Science (AIMS). (2017x)
RS	Abu Madafi (wave-exposed), Saudi Arabia	MD1	02-Feb-2010 01-May-2011	22.2	38.9	0.8	RS	±0.2	Kristen Davis, Jesus Pineda	Davis et al. (2011); Pineda et al. (2013)

Continued on next page

Table B.1 – continued from previous page

Region	Location	Abbr.	Duration	Latitude (°N)	Longitude (°E)	Logger Depth (m)	Logger Habitat	Logger Accuracy (°C)	Data Source	Related Publication
RS	Abu Madafi (wave-exposed), Saudi Arabia	MD2	02-Feb-2010 01-May-2011	22.2	38.9	0.8	RS	±0.2	Kristen Davis, Jesus Pineda	Davis et al. (2011); Pineda et al. (2013)
RS	Abu Madafi (wave-protected), Saudi Arabia	MD3	02-Feb-2010 01-May-2011	22.2	38.9	0.8	BR	±0.2	Kristen Davis, Jesus Pineda	Davis et al. (2011); Pineda et al. (2013)
RS	Abu Madafi (wave-protected), Saudi Arabia	MD4	02-Feb-2010 01-May-2011	22.2	38.9	0.8	BR	±0.2	Kristen Davis, Jesus Pineda	Davis et al. (2011); Pineda et al. (2013)
RS	Tahala (wave-exposed), Saudi Arabia	TA1	01-Feb-2010 30-Apr-2011	22.2	38.9	0.9	RS	±0.2	Kristen Davis, Jesus Pineda	Davis et al. (2011); Pineda et al. (2013)
RS	Tahala (wave-exposed), Saudi Arabia	TA2	01-Feb-2010 30-Apr-2011	22.2	38.9	0.9	RS	±0.2	Kristen Davis, Jesus Pineda	Davis et al. (2011); Pineda et al. (2013)
RS	Tahala (wave-protected), Saudi Arabia	TA3	01-Feb-2010 30-Apr-2011	22.2	38.9	0.9	BR	±0.2	Kristen Davis, Jesus Pineda	Davis et al. (2011); Pineda et al. (2013)
RS	Tahala (wave-protected), Saudi Arabia	TA4	01-Feb-2010 30-Apr-2011	22.2	38.9	0.9	BR	±0.2	Kristen Davis, Jesus Pineda	Davis et al. (2011); Pineda et al. (2013)

Appendix C

Bleaching Data

Table C.1: **Bleaching Data.** For each time series, the approximate survey date and computed bleaching prevalence score are noted, as well as a reference which details the bleaching event. Ocean regions and time series abbreviations are defined in Supplementary Data B.

Ocean Region	Time Series Abbreviation	Reef	Date	Bleaching Prevalence Score	Reference
WIO	MBA	Mombasa, Kenya	11-May-98	4	McClanahan et al. (2001)
WIO	MBA	Mombasa, Kenya	15-Apr-98	4	McClanahan et al. (2007a)
PO	P08	Palmyra SE Forereef	15-Oct-08	0	Williams et al. (2010), Gareth Williams (personal communication)
PO	P08	Palmyra SE Forereef	15-Jul-09	0	Williams et al. (2010), Gareth Williams (personal communication)
PO	P08	Palmyra SE Forereef	15-Oct-09	1	Williams et al. (2010), Gareth Williams (personal communication)
PO	P31	Palmyra South Forereef	15-Oct-08	0	Williams et al. (2010), Gareth Williams (personal communication)
PO	P31	Palmyra South Forereef	15-Jul-09	0	Williams et al. (2010), Gareth Williams (personal communication)
PO	P31	Palmyra South Forereef	15-Oct-09	2	Williams et al. (2010), Gareth Williams (personal communication)
PO	P12	Palmyra Eastern Backreef	15-Aug-08	0	Williams et al. (2010), Gareth Williams (personal communication)
PO	P12	Palmyra Eastern Backreef	15-Oct-08	0	Williams et al. (2010), Gareth Williams (personal communication)

Continued on next page

Table C.1 – continued from previous page

Ocean Region	Time Series Abbreviation	Reef	Date	Bleaching Prevalence Score	Reference
PO	P12	Palmyra Eastern Backreef	15-Jul-09	1	Williams et al. (2010), Gareth Williams (personal communication)
PO	P12	Palmyra Eastern Backreef	15-Oct-09	1	Williams et al. (2010), Gareth Williams (personal communication)
PO	P15	Palmyra SW Inner Backreef	15-Aug-08	0	Williams et al. (2010), Gareth Williams (personal communication)
PO	P15	Palmyra SW Inner Backreef	15-Oct-08	0	Williams et al. (2010), Gareth Williams (personal communication)
PO	P15	Palmyra SW Inner Backreef	15-Jul-09	0	Williams et al. (2010), Gareth Williams (personal communication)
PO	P15	Palmyra SW Inner Backreef	15-Oct-09	2	Williams et al. (2010), Gareth Williams (personal communication)
PO	P16	Palmyra SW Mid Backreef	15-Aug-08	0	Williams et al. (2010), Gareth Williams (personal communication)
PO	P16	Palmyra SW Mid Backreef	15-Oct-08	0	Williams et al. (2010), Gareth Williams (personal communication)
PO	P16	Palmyra SW Mid Backreef	15-Jul-09	0	Williams et al. (2010), Gareth Williams (personal communication)
PO	P16	Palmyra SW Mid Backreef	15-Oct-09	1	Williams et al. (2010), Gareth Williams (personal communication)
PO	P17	Palmyra SW Outer Backreef	15-Jul-09	0	Williams et al. (2010), Gareth Williams (personal communication)
PO	P17	Palmyra SW Outer Backreef	15-Oct-09	2	Williams et al. (2010), Gareth Williams (personal communication)
PO	P18	Palmyra Western Terrace	15-Aug-08	0	Williams et al. (2010), Gareth Williams (personal communication)
PO	P18	Palmyra Western Terrace	15-Oct-08	0	Williams et al. (2010), Gareth Williams (personal communication)
PO	P18	Palmyra Western Terrace	15-Jul-09	1	Williams et al. (2010), Gareth Williams (personal communication)
PO	P18	Palmyra Western Terrace	15-Oct-09	1	Williams et al. (2010), Gareth Williams (personal communication)
CS	DRY	Dry Tortugas	15-Aug-97	4	Manzello et al. (2007)
CS	DRY	Dry Tortugas	15-Aug-98	4	Manzello et al. (2007)
CS	MLS	Molasses Reef	15-Aug-97	4	Manzello et al. (2007)

Continued on next page

Table C.1 – continued from previous page

Ocean Region	Time Series Abbreviation	Reef	Date	Bleaching Prevalence Score	Reference
CS	MLS	Molasses Reef	15-Aug-98	4	Manzello et al. (2007)
CS	MLS	Molasses Reef	15-Aug-05	3	Manzello et al. (2007)
CS	SDK	Sand Key	15-Aug-05	3	Manzello et al. (2007)
CS	SBR	Sombrero Reef	15-Aug-04	2	Manzello et al. (2007)
CS	SBR	Sombrero Reef	15-Aug-05	4	Manzello et al. (2007)
GBR	CB1	Cattle Bay	15-Mar-98	4	Berkelmans and Oliver (1999)
GBR	CB2	Cattle Bay	15-Mar-98	4	Berkelmans and Oliver (1999)
GBR	CH2	Chicken Reef	15-Mar-98	1	Berkelmans (2002)
GBR	DV1	Davies Reef	15-Jan-98	1	Berkelmans et al. (2004)
GBR	DV2	Davies Reef	15-Jan-98	1	Berkelmans et al. (2004)
GBR	DD1	Daydream Island	15-Mar-98	1	Berkelmans and Oliver (1999)
GBR	HW1	Halfway Island	21-Dec-10	0	Berkelmans et al. (2012)
GBR	HW1	Halfway Island	23-May-11	4	Berkelmans et al. (2012)
GBR	HW2	Halfway Island	15-Mar-98	4	Berkelmans (2002)
GBR	HW2	Halfway Island	21-Dec-10	0	Berkelmans et al. (2012)
GBR	HW2	Halfway Island	23-May-11	4	Berkelmans et al. (2012)
GBR	HW2	Halfway Island	15-Feb-02	4	Elvidge et al. (2004)
GBR	HR1	Heron Island	15-Mar-98	1	Berkelmans (2002)
GBR	HR1	Heron Island	25-Feb-06	1	Maynard et al. (2008b)
GBR	HR1	Heron Island	25-Feb-07	0	Maynard et al. (2008b)
GBR	KO1	Kelso Reef	15-Feb-98	1	Maynard et al. (2008a)
GBR	KO2	Kelso Reef	15-Feb-98	1	Maynard et al. (2008a)
GBR	KO3	Kelso Reef	15-Feb-98	1	Maynard et al. (2008a)
GBR	KO1	Kelso Reef	15-Feb-02	3	Maynard et al. (2008a)
GBR	KO3	Kelso Reef	15-Feb-02	3	Maynard et al. (2008a)
GBR	LW1	Low Isles	15-Mar-98	4	Berkelmans (2002)
GBR	MIA	Miall Island	21-Dec-10	0	Berkelmans et al. (2012)
GBR	MR2	Middle Reef	15-Mar-98	4	Berkelmans and Oliver (1999)
GBR	MY1	Myrmidon Reef	15-Mar-98	1	Berkelmans (2002)
GBR	MY3	Myrmidon Reef	15-Mar-98	1	Berkelmans (2002)
GBR	MY5	Myrmidon Reef	15-Mar-98	1	Berkelmans (2002)
GBR	NK1	North Keppel Island	21-Dec-10	0	Berkelmans et al. (2012)
GBR	NK2	North Keppel Island	21-Dec-10	0	Berkelmans et al. (2012)
GBR	NK2	North Keppel Island	23-May-11	3	Berkelmans et al. (2012)
GBR	NY1	Nelly Bay	15-Mar-98	4	Berkelmans and Oliver (1999)
GBR	NY2	Nelly Bay	15-Mar-98	2	Marshall and Baird (2000)
GBR	NO1	Norman Reef	15-Mar-98	1	Berkelmans (2002)
GBR	NO2	Norman Reef	15-Mar-98	1	Berkelmans (2002)
GBR	PU1	Pelorus Island	15-Mar-98	4	Marshall and Baird (2000)
GBR	PU1	Pelorus Island	15-Feb-02	1	Maynard et al. (2008a)
GBR	PU2	Pelorus Island	15-Mar-98	4	Marshall and Baird (2000)
GBR	PU2	Pelorus Island	15-Feb-98	3	Maynard et al. (2008a)
GBR	PU2	Pelorus Island	15-Feb-02	1	Maynard et al. (2008a)

Continued on next page

Table C.1 – continued from previous page

Ocean Region	Time Series Abbreviation	Reef	Date	Bleaching Prevalence Score	Reference
GBR	PU3	Pelorus Island	15-Mar-98	4	Marshall and Baird (2000)
GBR	PU3	Pelorus Island	15-Feb-02	1	Maynard et al. (2008a)
GBR	PIO	Pioneer Bay	15-Mar-98	4	Marshall and Baird (2000)
GBR	WL1	Wallace Islet	15-Mar-98	1	Berkelmans (2002)
GBR	WL2	Wallace Islet	15-Mar-98	1	Berkelmans (2002)
RS	MD1	Abu Madafi	15-Sep-10	2	Furby et al. (2013)
RS	MD2	Abu Madafi	15-Sep-10	2	Furby et al. (2013)
RS	TA1	Tahala	15-Sep-10	4	Furby et al. (2013)
RS	TA2	Tahala	15-Sep-10	4	Furby et al. (2013)

Appendix D

Mixed Effects Ordinal Logistic Regression

Table D.1: **Results of Mixed Effects Ordinal Logistic Regression Models.** After identifying the *in situ* covariates and their coefficients from the highest-ranked models ($\Delta AIC_C \leq 2$), we computed these same models with the addition of a random effect accounting for reef proximities to each other; reefs within 5 km of each other were grouped together. Parameter estimates for the intercepts, as well as the covariate coefficients included in each of the highest-ranked models, are shown below. Also given are the standard deviations for the random effects terms in the mixed effects models, AIC_C values, likelihood ratio statistics and the associated p-values, and McFadden's pseudo R^2 values. Mixed effects models were computed with the statistical computing software R (`www.r-project.org`), which uses the equation below, and therefore, here covariates with negative coefficients act as bleaching 'mitigators'. $\ln\left(\frac{P(y_i \leq j)}{P(y_i > j)}\right) = C_j - \left(B_1 z_{i1} + \cdots + B_p z_{ip}\right)$

Model Type: Fixed Effects (FE) or Mixed Effects (ME)	**Intercept Estimates**			**Covariate Parameter Estimates**						**Mean Random Effect Parameter Estimate**	**Random Effect Standard Deviation**	**AIC_C**	**Likelihood Ratio Statistic**	***p*-value**	**McFadden's pseudo R^2**
	C_1	**C_2**	**C_3**	**Depth**	**DHW_{30}**	**Acute1**	**TT**	**$ROTC_{SS}$**	**DTR_{30}**						
FE	0.72	1.41	2.00	-1.85	0.96	0.74	0.90	0.66	-2.66	NA	NA	143.747	0.37800	0.53870	0.296
ME	0.81	1.53	2.14	-2.02	1.14	0.68	0.84	0.67	-2.89	-0.62	0.53719	145.976			0.298
	C_1	**C_2**	**C_3**	**Depth**	**Acute1**	**TT**	**$ROTC_{SS}$**	**DTR_{30}**							
FE	0.65	1.31	1.88	-1.63	0.94	1.08	0.64	-2.16		NA	NA	144.062	0.00000	1.00000	0.279
ME	0.65	1.31	1.88	-1.63	0.94	1.08	0.64	-2.16		-6.67	0.00126	146.597			0.279
	C_1	**C_2**	**C_3**	**Depth**	**MMM**	**DHW_{30}**	**Acute1**	**DTR_{30}**							
FE	0.80	1.47	2.03	-1.71	0.63	1.22	0.91	-2.30		NA	NA	144.084	3.09610	0.07848	0.279
ME	0.89	1.69	2.39	-1.98	0.93	1.73	0.66	-2.97		0.24	1.26498	143.524			0.297
	C_1	**C_2**	**C_3**	**Depth**	**MMM**	**CSA_{Total}**	**Acute1**	**DTR_{30}**							
FE	0.61	1.26	1.83	-1.31	0.93	1.20	1.26	-1.91		NA	NA	144.291	0.84470	0.35800	0.278
ME	0.63	1.33	1.94	-1.37	1.06	1.29	1.22	-2.07		-0.38	0.68680	145.982			0.283
	C_1	**C_2**	**C_3**	**Depth**	**MMM**	**CSA_{Before}**	**Acute1**	**TT**	**DTR_{30}**						
FE	0.53	1.20	1.80	-1.13	0.87	0.78	1.17	0.72	-1.79	NA	NA	144.578	0.00000	1.00000	0.291
ME	0.53	1.20	1.80	-1.13	0.87	0.78	1.17	0.72	-1.79	-9.44	0.00008	147.186			0.291
	C_1	**C_2**	**C_3**	**Depth**	**CSA_{Durir}**	**Acute1**	**TT**	**$ROTC_{SS}$**	**DTR_{30}**						
FE	0.73	1.40	1.98	-1.83	0.83	0.90	0.75	0.65	-2.54	NA	NA	144.632	0.07880	0.77900	0.291
ME	0.76	1.45	2.05	-1.89	0.89	0.88	0.71	0.65	-2.62	-1.05	0.34828	147.161			0.291
	C_1	**C_2**	**C_3**	**Depth**	**DHW_{90}**	**Acute1**	**TT**	**$ROTC_{SS}$**	**DTR_{30}**						
FE	0.72	1.40	1.98	-1.83	0.82	0.90	0.76	0.65	-2.53	NA	NA	144.719	0.07480	0.78450	0.290
ME	0.76	1.45	2.04	-1.89	0.87	0.88	0.72	0.65	-2.61	-1.07	0.34323	147.251			0.290
	C_1	**C_2**	**C_3**	**Depth**	**MMM**	**CSA_{During}**	**Acute1**	**DTR_{30}**							

Continued on next page

Table D.1 continued from previous page

Model Type: Fixed Effects (FE) or Mixed Effects (ME)	**Intercept Estimates**			**Covariate Parameter Estimates**							**Mean Random Effect Parameter Estimate**	**Random Effect Standard Deviation**	**AIC_C**	**Likelihood Ratio Statistic**	***p*-value**	**McFadden's pseudo R^2**
FE	0.82	1.47	2.03	-1.79	0.53	1.13	1.06	-2.37			NA	NA	144.730	1.97010	0.16040	0.275
ME	0.83	1.57	2.23	-1.84	0.77	1.32	0.90	-2.65			0.04	1.03790	145.295			0.287
	C_1	**C_2**	**C_3**	**Depth**	**MMM**	**DHW_{90}**	**Acute1**	**DTR_{30}**								
FE	0.81	1.47	2.03	-1.80	0.53	1.12	1.06	-2.36			NA	NA	144.878	1.94550	0.16310	0.275
ME	0.83	1.57	2.23	-1.85	0.76	1.30	0.91	-2.64			0.03	1.03196	145.468			0.286
	C_1	**C_2**	**C_3**	**Depth**	**MMM**	**DHW_{30}**	**Acute1**	**TT**	**DTR_{30}**							
FE	0.73	1.41	1.99	-1.69	0.58	1.03	0.81	0.48	-2.28		NA	NA	145.007	2.02520	0.15470	0.171
ME	0.81	1.59	2.28	-1.87	0.82	1.50	0.61	0.33	-2.82		0.09	1.09021	145.589			0.171
	C_1	**C_2**	**C_3**	**Depth**	**CSA_{Durir}**	**Acute1**	**$ROTC_{SS}$**	**DTR_{30}**								
FE	0.88	1.53	2.08	-2.14	1.25	1.04	0.46	-2.74			NA	NA	145.013	0.72680	0.39390	0.274
ME	0.95	1.64	2.24	-2.30	1.36	0.99	0.48	-2.96			-0.46	0.63168	146.821			0.278
	C_1	**C_2**	**C_3**	**Depth**	**MMM**	**CSA_{Before}**	**Acute1**	**TT**	**$ROTC_{SS}$**	**DTR_{30}**						
FE	0.49	1.19	1.79	-1.04	0.62	0.68	1.10	0.93	0.52	-1.94	NA	NA	145.015	0.00000	1.00000	0.303
ME	0.49	1.19	1.79	-1.04	0.62	0.68	1.10	0.93	0.52	-1.94	-9.51	0.00007	147.698			0.303
	C_1	**C_2**	**C_3**	**Depth**	**DHW_{90}**	**Acute1**	**$ROTC_{SS}$**	**DTR_{30}**								
FE	0.87	1.52	2.08	-2.14	1.24	1.04	0.46	-2.73			NA	NA	145.162	0.72470	0.39460	0.273
ME	0.95	1.63	2.23	-2.31	1.35	0.99	0.48	-2.95			-0.46	0.63063	146.972			0.277
	C_1	**C_2**	**C_3**	**Depth**	**MMM**	**DHW_{30}**	**Acute1**	**TT**	**$ROTC_{SS}$**	**DTR_{30}**						
FE	0.64	1.35	1.95	-1.52	0.36	0.98	0.77	0.78	0.54	-2.45	NA	NA	145.188	0.78570	0.37540	0.302
ME	0.70	1.45	2.10	-1.61	0.51	1.20	0.67	0.66	0.49	-2.65	-0.33	0.72029	147.085			0.307
	C_1	**C_2**	**C_3**	**Depth**	**MMM**	**CSA_{Total}**	**Acute1**	**TT**	**DTR_{30}**							
FE	0.59	1.26	1.84	-1.39	0.83	0.98	1.12	0.48	-2.01		NA	NA	145.240	0.51120	0.47460	0.287
ME	0.60	1.30	1.92	-1.40	0.92	1.06	1.07	0.45	-2.11		-0.52	0.59170	147.337			0.290
	C_1	**C_2**	**C_3**	**Depth**	**MMM**	**CSA_{Before}**	**Acute1**	**DTR_{30}**								
FE	0.67	1.30	1.86	-1.12	0.90	0.81	1.38	-1.79			NA	NA	145.294	0.00420	0.94820	0.272
ME	0.67	1.31	1.87	-1.13	0.90	0.80	1.37	-1.80			-1.69	0.18536	147.825			0.272
	C_1	**C_2**	**C_3**	**Depth**	**CSA_{Befor}**	**Acute1**	**TT**	**$ROTC_{SS}$**	**DTR_{30}**							
FE	0.64	1.31	1.89	-1.59	0.35	1.01	1.08	0.69	-2.21		NA	NA	145.320	0.00000	1.00000	0.287
ME	0.64	1.31	1.89	-1.59	0.35	1.01	1.08	0.69	-2.21		-9.30	0.00009	147.927			0.287
	C_1	**C_2**	**C_3**	**Depth**	**CSA_{Durir}**	**Acute1**	**DTR_{30}**									
FE	0.94	1.55	2.09	-2.46	1.14	1.00	-2.60				NA	NA	145.382	1.33170	0.24850	0.258
ME	0.95	1.62	2.22	-2.52	1.26	0.89	-2.83				-0.26	0.77482	146.516			0.265
	C_1	**C_2**	**C_3**	**Depth**	**DHW_{90}**	**Acute1**	**DTR_{30}**									
FE	0.93	1.55	2.09	-2.47	1.13	1.00	-2.60				NA	NA	145.511			0.257

Continued on next page

Table D.1 continued from previous page

Model Type: Fixed Effects (FE) or Mixed Effects (ME)	**Intercept Estimates**			**Covariate Parameter Estimates**						**Mean Random Effect Parameter Estimate**	**Random Effect Standard Deviation**	**AIC_C**	**Likelihood Ratio Statistic**	***p*-value**	**McFadden's pseudo R^2**
ME	0.95	1.62	2.22	-2.54	1.25	0.89	-2.83			-0.26	0.77120	146.659	1.31760	0.25100	0.264
	C_1	**C_2**	**C_3**	**Depth**	**MMM**	**Acute1**	**TT**	**$ROTC_{SS}$**	**DTR_{30}**						
FE	0.58	1.25	1.83	-1.33	0.30	0.96	1.01	0.55	-1.98	NA	NA	145.710	0.04620	0.82970	0.284
ME	0.60	1.28	1.87	-1.35	0.32	0.95	0.99	0.55	-2.01	-1.12	0.32539	148.271			0.285

Appendix E

Configuration Details for ROMS Simulations

Use the following information to reproduce the ROMS simulations described in Chapters 2 and 3.

E.1 Activated C-preprocessing (CPP) Options

For the base-case scenario (BL), the following options were activated in the C header code. Modifications to analytical expressions are noted in Section E.3; all others remained unchanged from their original repository settings.

```
ANA_BSFLUX          Analytical kinematic bottom salinity flux.
ANA_BTFLUX          Analytical kinematic bottom temperature flux.
ANA_DRAG_GRID       Analytical spatially varying bottom roughness length.
ANA_FSOBC           Analytical free-surface boundary conditions.
```

ANA_INITIAL	Analytical initial conditions.
ANA_M2OBC	Analytical 2D momentum boundary conditions.
ANA_M3OBC	Analytical 3D momentum boundary conditions.
ANA_SMFLUX	Analytical kinematic surface momentum flux.
ANA_SRFLUX	Analytical kinematic shortwave radiation flux.
ANA_SSFLUX	Analytical kinematic surface salinity flux.
ANA_STFLUX	Analytical kinematic surface temperature flux.
ASSUMED_SHAPE	Using assumed-shape arrays.
AVERAGES	Writing out time-averaged nonlinear model fields.
CANUTO_A	Canuto A-stability function formulation.
DIAGNOSTICS_TS	Computing and writing tracer diagnostic terms.
DIAGNOSTICS_UV	Computing and writing momentum diagnostic terms.
DIFF_GRID	Horizontal diffusion coefficient scaled by grid size.
DJ_GRADPS	Parabolic Splines density Jacobian (Shchepetkin, 2002).
DOUBLE_PRECISION	Double precision arithmetic.
GLS_MIXING	Generic Length-Scale turbulence closure.
LIMIT_BSTRESS	Limit bottom stress to maintain bottom velocity direction.
MIX_GEO_TS	Mixing of tracers along geopotential surfaces.
MIX_GEO_UV	Mixing of momentum along geopotential surfaces.
MPI	MPI distributed-memory configuration.
NONLINEAR	Nonlinear Model.
N2S2_HORAVG	Horizontal smoothing of buoyancy and shear.
OUT_DOUBLE	Double precision output fields in NetCDF files.
POWER_LAW	Power-law shape time-averaging barotropic filter.
PROFILE	Time profiling activated .
K_C4ADVECTION	Fourth-order centered differences advection of TKE fields.
RADIATION_2D	Use tangential phase speed in radiation conditions.

SALINITY	Using salinity.
SOLAR_SOURCE	Solar Radiation Source Term.
SOLVE3D	Solving 3D Primitive Equations.
TS_MPDATA	Recursive flux corrected MPDATA 3D advection of tracers.
TS_MPDATA_LIMIT	Further limiter in upwind corrector fluxes for stability.
TS_DIF2	Harmonic mixing of tracers.
UV_ADV	Advection of momentum.
UV_COR	Coriolis term.
UV_C4ADVECTION	Fourth-order centered differences advection of momentum.
UV_DRAG_GRID	Spatially varying bottom roughness length.
UV_LOGDRAG	Logarithmic bottom stress.
UV_VIS2	Harmonic mixing of momentum.
VAR_RHO_2D	Variable density barotropic mode.
VISC_GRID	Horizontal viscosity coefficient scaled by grid size.

In addition to the above, activate the following to implement the alongshore current forcing described in Chapters 2 and 3:

BODYFORCE	Momentum stresses as body-forces.

For the simulations of Chapter 3, in order to turn off depth-decaying shortwave radiation, do **not** activate SHORTWAVE, SOLAR_SOURCE, and ANA_SRFLUX

E.2 Input Parameters

Essential input parameter settings are as follows:

```
! Grid dimension parameters.
Lm == 100          ! Number of I-direction INTERIOR RHO-points
Mm == 500          ! Number of J-direction INTERIOR RHO-points
N == 30           ! Number of vertical levels
! Set lateral boundary conditions keyword.
LBC(isFsur) ==   Per     Clo     Per     Che            ! free-surface
LBC(isUbar) ==   Per     Clo     Per     Shc            ! 2D U-momentum
LBC(isVbar) ==   Per     Clo     Per     Shc            ! 2D V-momentum
LBC(isUvel) ==   Per     Clo     Per     Rad            ! 3D U-momentum
LBC(isVvel) ==   Per     Clo     Per     Rad            ! 3D V-momentum
LBC(isMtke) ==   Per     Clo     Per     Gra            ! mixing TKE
LBC(isTvar) ==   Per     Clo     Per     Gra    \       ! temperature
                 Per     Clo     Per     Gra            ! salinity
! Time-Stepping parameters.
NTIMES == 1209600
DT == 2.0d0
NDTFAST == 35
! Output history, average, diagnostic files parameters.
LDEFOUT == T
NHIS == 300
NDEFHIS == 1800
NTSAVG == 1
NAVG == 10800
```

```
 NDEFAVG == 43200
 NTSDIA == 1
 NDIA == 300
 NDEFDIA == 1800
 ! Harmonic/biharmonic horizontal diffusion of tracer for nonlinear model
 ! and adjoint-based algorithms: [1:NAT+NPT,Ngrids].
 TNU2 == 0.0844 0.0844                   ! m2/s
 ! Harmonic/biharmonic, horizontal viscosity coefficient for nonlinear model
 ! and adjoint-based algorithms: [Ngrids].
 VISC2 == 0.0844                          ! m2/s
 ! Logical switches (TRUE/FALSE) to increase/decrease horizontal viscosity
 ! and/or diffusivity in specific areas of the application domain (like
 ! sponge areas) for the desired application grid.
 LuvSponge == T                                ! horizontal momentum
 LtracerSponge == T T                              ! temperature, salinity, inert
! Generic length-scale turbulence closure parameters.
! (set to k-epsilon)
 GLS_P == 3.0d0
 GLS_M == 1.5d0
 GLS_N == -1.0d0
 GLS_Kmin == 1.0d-10        ! minimum TKE lowered to 1e-10 m2/s2
 GLS_Pmin == 1.0d-12
 GLS_CMU0 == 0.5477d0
 GLS_C1 == 1.44d0
 GLS_C2 == 1.92d0
 GLS_C3M == -0.4d0
 GLS_C3P == 1.0d0
```

```
GLS_SIGK == 1.0d0

GLS_SIGP == 1.30d0

! Constants used in momentum stress computation.

Zob == 0.02d0                     ! m

! Various parameters.

WTYPE == 1       ! Jerlov optical clarity

LEVSFRC == 1 ! Surface momentum body force penetrates from this layer up to surface

LEVBFRC == 1 ! Btw momentum body force penetrates up to this layer

! Set vertical, terrain-following coordinates transformation equation and

! stretching function, [1:Ngrids].

Vtransform == 2                          ! transformation equation

Vstretching == 4                          ! stretching function

! Vertical S-coordinates parameters (see below for details), [1:Ngrids].

THETA_S == 3.0d0                       ! surface stretching parameter

THETA_B == 1.0d0                       ! bottom  stretching parameter

TCLINE == 25.0d0                       ! critical depth (m)

! Mean Density and Brunt-Vaisala frequency.

RHO0 =  1025.0d0                    ! kg/m3

BVF_BAK =  1.0d-5                      ! 1/s2

! Linear equation of State parameters:

R0 == 1027.0d0                   ! kg/m3

T0 == 24.0d0                     ! Celsius

S0 == 35.0d0                     ! nondimensional

TCOEF == 1.7d-4                    ! 1/Celsius

SCOEF == 7.6d-4                    ! nondimensional

! Slipperiness parameter: 1.0 (free slip) or -1.0 (no slip)

GAMMA2 == -1.0d0
```

E.2.1 Vertical Mixing Modifications

The $k - \epsilon$ turbulence closure is used in all simulations, and the minimum turbulent kinetic energy (TKE) value (`GLS_Kmin` in the input parameter file) is lowered to 1E-10 m^2s^{-2}. Furthermore, the surface boundary condition for TKE, located in `/Nonlinear/gls_corstep.F`, is set to 0 m^2s^{-2} as follows:

```
...
!-----------------------------------------------------------------------
!  Time-step dissipation and vertical diffusion terms implicitly.
!-----------------------------------------------------------------------
!  Set Dirichlet surface and bottom boundary conditions. Compute
!  surface roughness from wind stress (Charnok) and set Craig and
!  Banner wave breaking surface flux, if appropriate.
!
 DO i=Istr,Iend
#  if defined CRAIG_BANNER
      ...
#  elif defined TKE_WAVEDISS
      ...
#  else
      tke(i,j,N(ng),nnew)=0.0_r8
#  endif
 ...
```

E.3 Analytical Forcing Expressions

E.3.1 Surface Heat Flux

To implement the surface heat flux from Chapter 2, define shortwave radiation as follows in the analytical file `ana_srflux.h`:

```
DO j=JstrT,JendT
    DO i=IstrT,IendT
        srflx(i,j)=(1.0_r8/(rho0*cp))*((1.0836_r8*750_r8) &
                   *(sin(pi*time(ng)/86400.0_r8)**10))
    END DO
END DO
```

Next, in the analytical file `ana_stflux.h`, define the total surface heat flux as the sum of shortwave radiation and a constant cooling value:

```
DO j=JstrT,JendT
    DO i=IstrT,IendT
        stflx(i,j,itrc)= srflx(i,j) - (200.0_r8/(rho0*cp))
    END DO
END DO
```

E.3.2 Kinematic Momentum Flux

In order to implement upwelling- and downwelling-favorable alongshore currents as in Chapters 2 and 3, set the kinematic momentum flux as follows in the analytical file `ana_smflux.h`:

```
DO j=JstrT,JendT
```

Simulations	**Amplitude**	**Simulations**	**Amplitude**
U1 and NU1	-1E-5	D1 and ND1	1E-5
U2 and NU2	-2E-5	D2 and ND2	2E-5
U3 and NU3	-6E-5	D3 and ND3	6E-5
U4 and NU4	-2.922E-4	D4 and ND4	2.922E-4
U5 and NU5	-4E-4	D5 and ND5	4E-4
U6 and NU6	-9E-4	D6 and ND6	9E-4

Table E.1: Amplitude of kinematic momentum flux for each ROMS simulation with alongshore forcing, as in Chapters 2 and 3.

```
    DO i=IstrP,IendT
        sustr(i,j)=(...)*abs(GRID(ng)%h(i,j))/20.0_r8
    END DO
END DO
```

In the above, the local depth is scaled by a reference depth of 20 m, and the omitted value inside the parentheses is the net kinematic momentum flux amplitude. Table E.1 gives amplitudes corresponding to each simulation from Chapters 2 and 3.

Appendix F

Thermal Exchange Results from Simulations with Different Turbulence Closures

As mentioned in Chapter 2, the results from ROMS simulations of thermally-driven exchange are sensitive to the parameterization of subgrid-scale processes, such as convection and turbulent mixing. Prior to finalizing the simulation configurations for Chapter 2, multiple runs of the base-case scenario (i.e. forced only with the diurnal buoyancy flux) of thermally-driven exchange were performed, each implementing one of the different turbulence closures offered within ROMS. Two general classes of vertical mixing schemes are used here: the algebraic K-profile parameterization (KPP) of Large et al. (1994) and the two-equation turbulence closures given by the Level 2.5 scheme of Mellor and Yamada (1974) or the general length scale (GLS) approach of Umlauf and Burchard (2003) and implemented in ROMS according to Warner et al. (2005). The following is not intended to be a comprehensive comparison of different turbulence closures, but rather, to demonstrate that the choice of mixing scheme is highly consequential in simulations of relatively quiescent flows that are heavily dependent

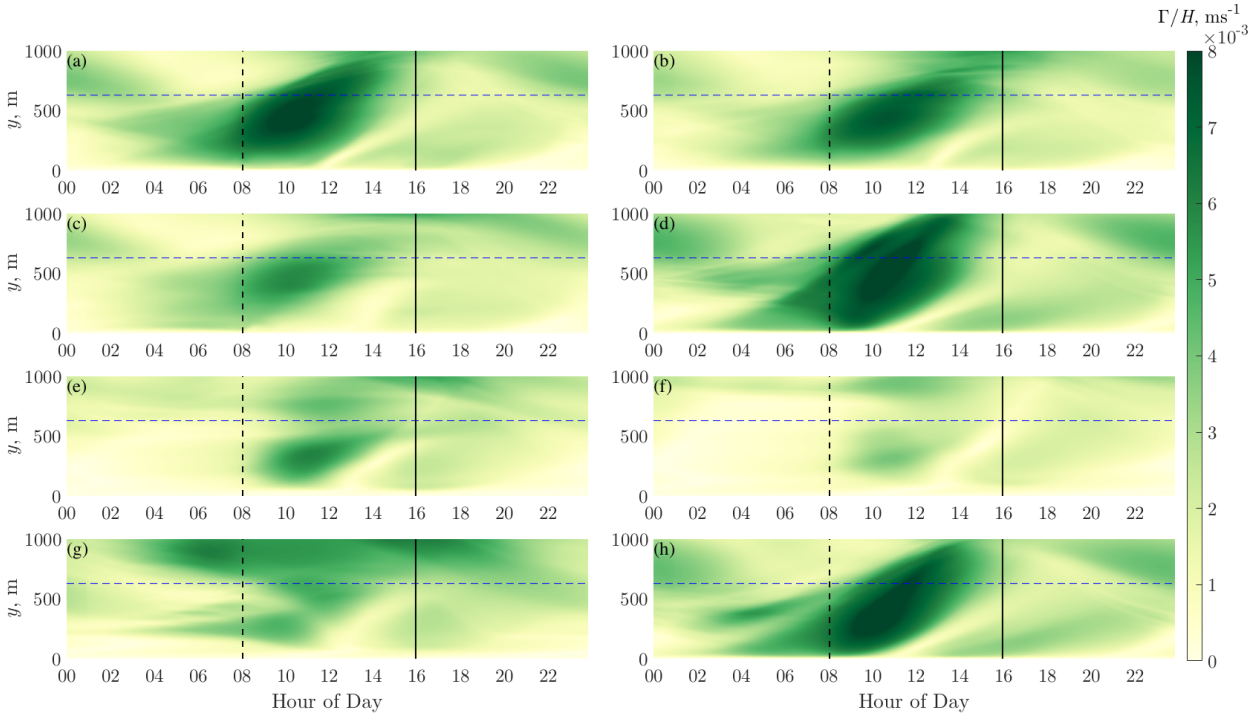

Figure F.1: Depth-normalized baroclinic cross-shore volume exchange, Γ/H (see Chapter 2), as a function of time and distance offshore, computed from base-case simulations of thermal exchange using the following turbulence closures: KPP (a), KPP with the maximum interior diffusivity due shear instability multiplied by 10 (b) and 100 (c), Mellor and Yamada's Level 2.5 closure (d), GLS, $k-kl$ (e), GLS, $k-\epsilon$ (f), GLS, $k-\omega$ (g), and the generic GLS closure (h). The offshore location of the 20 m isobath is indicated by the horizontal dashed line spanning each panel, the dashed black line indicates the transition time from net surface cooling to net surface heating, and the solid black line indicates the transition time from net surface heating to net surface cooling.

on mixing dynamics; in this case, a domain with a sloping bottom, initially unstratified and at rest, and forced only with surface heating and cooling. The depth-normalized exchange, or Γ/H from Chapter 2, is used to illustrate results according to the different turbulence closures (Fig. F.1).

Additional simulations using modifications to the standard KPP scheme were also completed. These modifications increased the maximum interior diffusivity due shear instability, originally set to 0.001 $\mathrm{m^2 s^{-1}}$, by factors of 10 (Fig. F.1b) and 100 (Fig. F.1c). The GLS schemes solve transport equations for the turbulent kinetic energy, k, and a second parameter that is used to determine the turbulent length scale, l. These include the $k-kl$ (Fig. F.1e), $k-\epsilon$ (Fig. F.1f), and $k-\omega$ (Fig. F.1g) parameterizations, where ϵ is the dissipation of turbulent kinetic energy and ω is a physically meaningless quantity, but can be approximately interpreted such that ω^2 "is the mean square vorticity of the 'energy containing eddies' " (Saffman, 1970), and $l \sim k^{1/2}\omega^{-1}$. A fourth GLS scheme given by Umlauf and Burchard (2003) is expected to be applicable to multiple scales of turbulence (Fig. F.1h).

Considering that all simulations were forced with the same diurnal buoyancy flux, the resulting differences in the spatial structure and magnitudes of Γ/H are striking and warrant investigation.